# Aerodynamic Damping of an Oscillating Fan Blade: Numerical Fluid Structure Interaction Analysis

by
Christian Dietrich Peters

*Thesis presented in partial fulfilment of the requirements for the degree of Master of Engineering (Mechanical) in the Faculty of Engineering at Stellenbosch University*


Supervisor: Dr. D.N.J. Els
Co-supervisor: Prof. S.J. van der Spuy

March 2017

# Declaration

By submitting this thesis electronically, I declare that the entirety of the work contained therein is my own, original work, that I am the sole author thereof (save to the extent explicitly otherwise stated), that reproduction and publication thereof by Stellenbosch University will not infringe any third party rights and that I have not previously in its entirety or in part submitted it for obtaining any qualification.

Date: March 2017

# Abstract

The thesis' main objective is to determine the dynamic flow phenomena that dampen a fan blade's oscillation amplitude using numerical fluid structure interaction (FSI) simulations. The observed flow effects include the formation and shedding of leading edge vortices, downwash and the added mass effect. Leading edge vortices are a major damping contributor and are dependent on the blade's effective angle of attack.

The aim of the thesis is to find a suitable method that is capable of simulating the aerodynamic damping of an axial fan used in an air cooled condenser unit. Therefore, three different numerical models are used to perform the FSI simulation and are compared according to their accuracy, robustness and computational cost.

The aerodynamic damping of an oscillating fan blade was experimentally investigated by Basson (2015) and his results are used to validate the three numerical models.

The three methods used are a mesh-based FSI simulation, a simplified one dimensional beam model coupled with a heuristic flow model and a meshless FSI simulation. The mesh based and meshless FSI simulations are both suitable for modelling the entire air cooled condenser fan unit, whereas the simplified 1D beam model is incapable of doing so.

# Opsomming

Die tesis se hoofdoelwit is om die dinamiese vloei-verskynsels te bepaal wat 'n waaierlem se ossillasie amplitude demp met gebruik van numeriese vloei struktuur interaksie simulasies (FSI). Die waargeneemde vloei effekte sluit in die vorming en vergieting van leirand draaikolke, valstroomvloei en die bykomende massa-effek. Leirand draaikolke lewer 'n groot bydrae tot die demping en is afhanklik van die lem se effektiewe aanvalshoek.

Die doel van die tesis is om 'n geskikte metode te vind wat in staat is om die aerodinamiese demping van 'n aksiale waaierlem in 'n lugverkoelde kondensoreenheid te simuleer. Daarom word drie verskillende numeriese modelle gebruik wat die vloei struktuur interaksie simulasie uitvoer en vergelyk volgens hul akkuraatheid, robuustheid en koste van berekening.

Die aerodinamiese demping van 'n ossilerende waaierlem is eksperimenteel ondersoek deur Basson (2015) en sy resultate word gebruik om die drie numeriese modelle te bevestig.

Die drie metodes is 'n rooster gebaseerde FSI simulasie, 'n vereenvoudigde een-dimensionele balk-model tesame met 'n heuristiese vloeimodel en 'n roosterlose FSI simulasie. Die rooster gebaseerde en roosterlose FSI simulasies is beide geskik vir die modellering van die hele lugverkoelde kondensor waaier eenheid, terwyl die vereenvoudigde 1D balk-model nie in staat is om dit te doen nie.

# Acknowledgements

I would like to thank:

- Dr. Els and Professor van der Spuy for their guidance and supervision. I appreciate their support and allowance for leeway when it came to choosing and developing the three different numerical methods.
- Dr. Kuhnert for his supervision and help with the Finite Pointset Method. I especially appreciate that Dr. Kuhnert offered me the opportunity to join his research group at the Fraunhofer ITWM Institute in Kaiserslautern, Germany.
- Olaf Diener, Pratik Suchde and my parents for their advice and help in improving the thesis.

# Contents

# List of Figures

# List of Tables

# Nomenclature

**Symbols**

| | |
|---|---|
| $A$ | Area |
| $A_{Pol}$ | Empirical correction factor for the Polhamus effect |
| $A_j$ | j-th undetermined coefficient |
| $a$ | Distance from blade root |
| $C$ | Theodorsen function |
| $C_{Air}$ | Speed of sound in air |
| $c$ | Chord length |
| $c$ | Viscous damping |
| $c_P, c_V$ | Specific heat at constant pressure and volume respectively |
| $D$ | Displacement |
| $E$ | Young's Modulus (Modulus of Elasticity) |
| $E$ | Error |
| $e$ | Span efficiency factor |
| $F$ | Force |
| $f$ | Frequency |
| $f_B$ | Distributed body force |
| $f_{Max}$ | Frequency of highest order mode |
| $G$ | Added mass correction term |
| $G$ | Shear modulus |
| $h$ | Heat transfer coefficient |
| $h_{SL}$ | Smoothing length |
| $I$ | Area moment of inertia |
| $K_v$ | Vortex lift term |
| $k$ | Reduced frequency |
| $k$ | Stiffness |
| $k_{AM}$ | Added mass velocity ratio |
| $L$ | Length |
| $m$ | Mass |
| $\dot{m}$ | Mass flow rate |
| $N$ | Node |
| $n$ | normal |
| $P_i$ | All points in the support domain of point i |
| $p$ | Pressure |

| | |
|---|---|
| $\dot{Q}$ | Heat transfer rate |
| $R$ | Pearson product-moment correlation coefficient |
| $R_{Air}$ | Gas constant of air |
| $Re$ | Reynold's number |
| $r$ | Frequency ratio |
| $r_v$ | Distance from vortex core to trailing edge |
| $S_\phi$ | Source term of arbitrary scalar $\phi$ |
| $T$ | Temperature |
| $T_{KE}$ | Kinetic energy |
| $t$ | Time variable |
| $t_1\,, t_2\,, t_3\,, t_4$ | Time instances in the blade's oscillation cycle as shown in figure 2.10 |
| $U$ | Velocity |
| $u$ | Flow velocity close to the wall |
| $u^+$ | Dimensionless velocity |
| $u^*$ | Frictional velocity |
| $V$ | Volume |
| $V_{Emp}$ | Factor to be approximated by the empirical factor |
| $v$ | Displacement degree of freedom |
| $\dot{W}$ | Rate of work done |
| $w$ | Weighting function |
| $x$ | Spatial variable |
| $Y$ | Base excitation |
| $\dot{Y}$ | Base excitation velocity |
| $y$ | Distance to the wall |
| $y^+$ | Dimensionless wall distance |
| $z$ | Spanwise spatial variable |
| $\alpha$ | Angle of attack |
| $\alpha$ | Constant used to determine FPM smoothing length |
| $\beta$ | Factor |
| $\Delta t$ | Time step |
| $\Delta t_{FEM}$ | Structural solver time step |
| $\Delta x$ | Cell length |
| $\delta$ | Amplitude decay factor |
| $\epsilon$ | Tolerance value |
| $\Gamma$ | Circulation strength |

| | |
|---|---|
| $\Gamma$ | Diffusion coefficient |
| $\gamma$ | Factor |
| $\lambda$ | Viscosity relating stress to volumetric deformation |
| $\mu$ | Dynamic viscosity |
| $\nu$ | Poisson's ratio |
| $\omega$ | Angular driving frequency |
| $\omega_n$ | Angular natural frequency |
| $\omega_d$ | Angular damped natural frequency |
| $\phi$ | Arbitrary scalar representing a field variable |
| $\rho$ | Density |
| $\sigma$ | Surface stress tensor |
| $\sigma_{XX}$ | Normal stress in x-direction |
| $\sigma_{XY}$ | Shear stress in the xy-plane |
| $\tau$ | Stress tensor |
| $\tau_W$ | Wall shear stress |
| $\theta$ | Angle |
| $\theta_j$ | Rotational degree of freedom of node j |
| $\varphi$ | Phase shift angle |
| $\zeta$ | Damping coefficient |

**Vectors and matrices**

| | |
|---|---|
| $\vec{A}$ | Face vector |
| $\boldsymbol{B}$ | Strain-displacement matrix |
| $\boldsymbol{C}$ | Damping matrix |
| $\boldsymbol{D}$ | Nodal degree of freedom vector |
| $\boldsymbol{D}_{Ext}$ | Extrapolated nodal degree of freedom vector |
| $\dot{\boldsymbol{D}}$ | Nodal degree of freedom velocity vector |
| $\ddot{\boldsymbol{D}}$ | Nodal degree of freedom acceleration vector |
| $\boldsymbol{E}$ | Constitutive matrix |
| $\boldsymbol{F}$ | Force vector |
| $\boldsymbol{K}$ | Stiffness matrix |
| $\boldsymbol{M}$ | Mass matrix |
| $\boldsymbol{N}$ | Shape function matrix |
| $\vec{x}_{P,i}$ | Position vector of point i |
| $\boldsymbol{\epsilon}$ | Strain vector |
| $\boldsymbol{\sigma}$ | Stress vector |

**Superscripts**

| | |
|---|---|
| $x$ | First derivative with respect to x |
| $xx$ | Second derivative with respect to x |
| $Eff$ | Effective |

**Subscripts**

| | |
|---|---|
| $Air$ | Air |
| $AM$ | Added mass |
| $B$ | Body |
| $Bl$ | Blade |
| $Con$ | Condenser |
| $Cons$ | Consistent |
| $Cr$ | Critical |
| $D$ | Drag |
| $E$ | Effective |
| $Env$ | Environment |
| $Exp$ | Experiment |
| $Ext$ | External |
| $F$ | Fluid |
| $G$ | Geometric |
| $G$ | Grid |
| $Glo$ | Global |
| $Gr$ | Growth |
| $ID$ | Induced drag |
| $In$ | Inlet |
| $L$ | Lift |
| $L, \alpha$ | Lift gradient |
| $Loc$ | Local |
| $Lum$ | Lumped |
| $N$ | Normal |
| $n$ | Time step n |
| $i$, $j$, $k$ | Counter variable |
| $ij$ | At point i considering neighbour j |
| $P$ | Peak |
| $p$ | Particular |
| $Pol$ | Polhamus |

| | |
|---|---|
| $Rel$ | Relative |
| $S$ | Surface |
| $ST$ | Separation threshold |
| $T$ | Tip |
| $T$ | Tangential |
| $Th$ | Theodorsen |
| $Tot$ | Total |
| $Tra$ | Transition |
| $Tur$ | Turbulence |
| $V$ | Vacuum |
| $Vor$ | Vortex |
| $x$ | Component in x-direction |
| 0 | Amplitude |
| $\infty$ | Free stream |
| $1D$ | 1D beam model |

**Acronyms**

| | |
|---|---|
| ACC | Air cooled condenser |
| AFS | Against free stream |
| ALE | Arbitrary Lagrangian-Eulerian |
| AOA | Angle of attack |
| AR | Aspect ratio |
| BC | Boundary condition |
| BS | Blade surface |
| CFD | Computational fluid dynamics |
| CFL | Courant-Friedrich-Lewys |
| DOF | Degree of freedom |
| EQ | Element quality |
| FPM | Finite Pointset Method |
| GE | Governing equation |
| FEM | Finite element method |
| FSI | Fluid structure interaction |
| FRF | Frequency response function |
| HAR | Hot air recirculation |
| LEV | Leading edge vortex |
| LLT | Lifting line theory |
| LSB | Laminar separation bubble |
| MDOF | Multiple degree of freedom |
| MPC | Multi-point-constraint |
| OQ | Orthogonal quality |
| PSOA | Particle swarm optimisation algorithm |
| RBE | Round blade edges |
| RD | Relative deviation |
| SDOF | Single degree of freedom system |
| SFR | Separated flow region |
| SPH | Smoothed particle hydrodynamics |
| SST | Shear stress transport |
| ST | Separation threshold |
| TI | Turbulence intensity |
| UF | Unstructured faces |
| WE | Wake edges |
| WFS | With free stream |

# Chapter 1

# Introduction

## 1.1 Project background

Electricity is generated in coal-fired power plants using the Rankine cycle depicted in figure 1.1. It is an ideal thermodynamic closed loop cycle that converts heat into mechanical work using the following four components:

**Boiler:** Heat is transferred from the burning coal to the working fluid, which is water. The water is evaporated in the process to produce superheated steam.

**Turbine:** The internal energy of the superheated steam is converted into mechanical work to drive a generator (Kapooria *et al.*, 2008). The steam exits the turbine at a considerably lower temperature than when it enters and is preferably saturated.

**Condenser:** The steam's residual energy cannot be efficiently used to further generate electricity. The excess energy is rejected to the environment and the steam condenses.

**Pump:** The condensate is pumped through the boiler where it can be efficiently reheated to superheated steam.

The cycle's maximum achievable thermal efficiency is limited by the temperature limits in the boiler and in the condenser. Its efficiency is improved if the vapour is superheated to higher temperatures in the boiler and condensed at lower temperatures in the condenser.

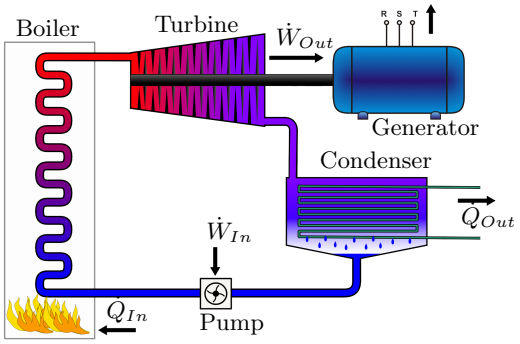


**Figure 1.1:** Diagram of the Rankine Cycle (Avinash, 2016)

Lowering the temperature in the condenser reduces the temperature difference between the environment $T_{Env}$ and the fluid (Cengel and Boles, 2008). As shown by equation (1.1), this has a negative effect on the condenser's heat transfer rate.

$$\dot{Q}_{Out} = hA\,(T_{Con} - T_{Env}) \tag{1.1}$$

The amount of heat that has to be rejected by the condenser is set by the required power output of the power plant. Kröger (2004) mentions that for fossil-fuel powered power plants, more than 40 % of the heat input has to be rejected by the cooling system. Lowering the condenser temperature $T_{Con}$ increases the amount of heat to be rejected and decreases the temperature difference in equation (1.1). This means that the heat transfer surface of the condenser $A$ and the condenser's heat transfer coefficient $h$ have to be sufficiently large enough to handle the required heat transfer rate. The heat transfer coefficient depends on the cooling fluid properties and fluid velocity (Cengel and Ghajar, 2011).

There are mainly two types of condensers used:

**Wet cooled:** The steam is condensed by transferring the excess heat to surrounding water by means of an intermediate condenser vessel. The cooling fluid evaporates during this process. A natural draft cooling tower can form part of the wet cooled condenser system and releases the evaporated cooling fluid into the atmosphere as shown in the left of figure 1.2.

**Dry cooled:** The cooling fluid is not water but air. An example of a forced draught air cooled condenser (ACC) is displayed on the right of figure 1.2. Heat is transferred from the steam to its surroundings by forced convection. Large fans are used to force air over finned tubes containing the steam.

Water shortages in South Africa restrict power plants to rely on direct dry cooling, since one major disadvantage of using wet cooling is the high water consumption, which can have negative environmental effects (Kröger, 2004). Examples of direct dry cooled power plants are the Medupi and Matimba power plants. According to its owners, Medupi will be the fourth largest coal fired power plant in the world (Eskom, 2013). Once it is fully operational and connected to the national power grid it will have a maximum capacity of 4800 MW.

The disadvantage of the dry cooling system is that it is dependent on the dry-bulb temperature, which can vary significantly during the day or season (Heyns, 2008). The heat transfer rate of a dry cooled condenser reduces during periods of high ambient temperatures. Furthermore, the thermal conductivity and density of air is lower than that of water, which inhibits heat transfer. To compensate for that, larger heat transfer surfaces and higher flow rates are required. This means that for the same cooling load, dry cooling systems are

usually larger than wet cooling systems. The capital cost of the condenser is therefore increased (Kröger, 2004).

**(a)** Natural draft cooling tower (ENEXIO, 2016)

**(b)** Air cooled condenser (Leita Steel Construction, 2016)

**Figure 1.2:** Two different types of condensers

### 1.1.1 Air cooled condenser (ACC)

Matimba's ACC consists of 288 fan units with fan diameters of 9.125 m. The fans are suspended 50 m above the ground to ensure that sufficient air can enter the ACC from below (Muiyser *et al.*, 2014).

Figure 1.3 depicts a single fan unit. Under optimal working conditions, air is forced from underneath the unit through the A-frame finned tube bundles. Heat is transferred from the turbine's exhaust steam to the ambient air in the process, which leads to steam condensation.

The inlet flow distribution may be disturbed due to the following reasons:

**Wind:** The ACC is open to the environment as seen on the right of figure 1.2. This means that environmental factors such as wind can affect the flow conditions upstream of the fan unit.

**Influence of the surrounding fan units or structures:** Figure 1.2 shows how the fan units are arranged. They are tightly packed and therefore, the flow through one unit can affect the upstream conditions of another. The turbine house and other structures are also constructed in the vicinity of the ACC. Thus, they can also influence the inlet flow conditions of the fan unit.

**Hot air recirculation (HAR):** The air is heated as it passes the fins of the condenser and usually exits the condenser on top to rise away from the ACC. Under certain wind conditions, this hot air can be recirculated and sucked in at the bottom of the ACC (Liu *et al.*, 2009). This reduces the performance of the condenser.

According to Liu *et al.* (2009) the wind speed, wind direction and air temperature are the main factors that influence the operation of an ACC. For example, wind causes a distorted flow pattern within the ACC fan unit that is responsible for a varying aerodynamic loading of the fan blades. This induces varying stresses in the fan blades and the other components of the ACC, which can lead to fatigue and may result in component failure.

Muiyser *et al.* (2014) measured the air flow rate through an ACC unit and simultaneously measured the varying stresses in a fan blade. The important findings of Muiyser *et al.* (2014) are listed below.

- The dominant vibration of the fan blade occurs at approximately 5.9 Hz, which is its own natural frequency. The vibration is caused by the varying aerodynamic load acting on the fan blades.
- A higher axial flow velocity through the fan reduces the flapwise bending loads of the fan blade.

The results show that the fan blade's vibrational motion is possibly damped due to the increased air flow rate. This phenomenon is termed aerodynamic damping and forms the focus of this research.

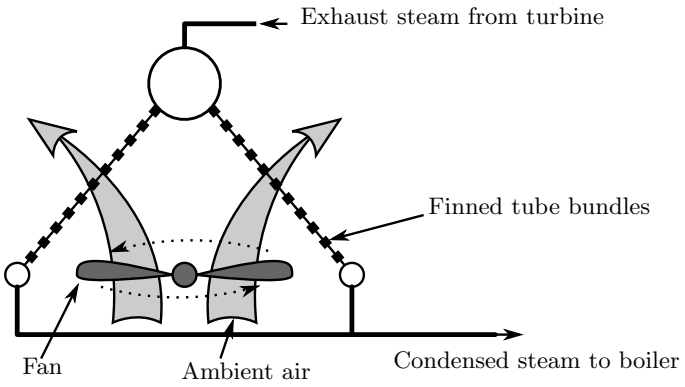


**Figure 1.3:** Diagram of the A-framed ACC

## 1.2 Flutter versus aerodynamic damping

When a flexible structure is submerged in a fluid, the motion of one affects the motion of the other. The study of this interaction is termed aeroelasticity. The interaction between the structure and fluid can be either (Hodges and Pierce, 2011):

**Stable:** If a small disturbance is introduced in the system, the system can correct for this disturbance and oscillate about its equilibrium position. The aerodynamic damping of the fan blades, as observed by Muiyser *et al.* (2014), is an example of a stable system.

**Neutrally stable:** A small disturbance leads to a constant deviation from the original equilibrium position of the system.

**Unstable:** If a small disturbance is introduced and the system deviation from the original equilibrium position increases. Flutter is an example of an unstable aeroelastic system. A small displacement of the structure induces aerodynamic forces that further amplify the deflection.

Structural failure can occur due to flutter, whereas aerodynamic damping can reduce the fatigue loading as seen in the previous section. Therefore, it is important to differentiate between the two dynamic aeroelastic interactions.

Cumpsty (1999) differentiates between induced blade vibration due to forced vibration and flutter for compressors. Both occur at or close to the natural frequency of the blades and can be summarised as follows:

**Flutter:** Flutter is a self-excited oscillation and does not have to occur at the harmonics of the rotational speed. According to Cumpsty (1999) rotating stall occurs at lower flow velocities whereas flutter occurs at higher flow velocities.

**Forced Vibration:** This usually occurs when the rotor moves through stationary disturbances. The sources for forced vibration must be harmonics of the rotational frequency of the rotor (Cumpsty, 1999). Forced vibration was observed by Muiyser *et al.* (2014), because the peak bending moments occurred at the first, second and third harmonic of the fan's rotational speed. The fan blade passes a fan bridge twice per cycle, which obtrudes the flow and thus a peak bending moment is observed at the second harmonic of the fan. The peak bending moment at the third harmonic coincides with the natural frequency of the blade.

The results of Muiyser *et al.* (2014) indicate that flutter does not occur. The aerodynamic forces dampen the blade oscillation due to forced vibration and thus stabilize the aeroelastic system.

## 1.3 Aerodynamic damping of an oscillating fan blade

The air flow distribution within the ACC is affected by several factors, which complicate the analysis of the aerodynamic damping phenomenon. These include the components of the ACC, wind speed and wind direction. Basson (2015) investigated the dynamic behaviour of a single axial fan blade to limit the number of variables influencing the blade's aerodynamic loading. This allowed for a systematic analysis of factors affecting the blade's dynamic response.

The single axial fan blade was placed in a low speed wind tunnel where the blades root was harmonically excited close to its first bending mode to investigate the effects of varying the air flow velocity and the geometric angle of attack (AOA) on the blade's tip displacement. Basson (2015) recommends that the experimental analysis is supplemented by a numerical fluid structure interaction (FSI) analysis to determine to what extent fluid phenomena, such as flow separation, influence the vibrational properties of the blade.

## 1.4 Problem statement and motivation

The aim of the thesis is to provide valuable insight into the aeroelastic behaviour of the oscillating fan blade tested by Basson (2015), by completing a numerical FSI simulation and analysing the flow around the blade. Results from the FSI simulation are validated by experimental and analytical findings. Different geometric AOAs and inlet flow velocities are investigated to obtain a broader understanding of their effects on aerodynamic damping.

Vibrations can cause structural and mechanical failure, especially if the excitation frequency is close to the system's resonance frequency. The ACC fan at Matimba vibrates at its own natural frequency, which can lead to large deflections of the fan blades (Muiyser *et al.*, 2014). Fatigue failures can occur, because the ACC's components, such as the gearbox or fan blades, are subjected to cyclic aerodynamic loading.

An in depth understanding of the occurring structural and fluid dynamic phenomena is an important step in designing more efficient ACC units and preventing component failure. This project is the first step in explaining and understanding the complex fluid and structure interactions within the ACC unit. Three numerical approaches are presented to solve the fluid structure interaction problem. The advantages and disadvantages of each are then weighed up to find a suitable model for simulating the entire ACC unit.

## 1.5 Objectives

The two major objectives set out for this project are to:

- Determine the main aerodynamic phenomena that influence the blade's motion, as measured by Basson (2015). Furthermore, relate changes of the blade's aerodynamic loading to alterations of the fluid inlet velocity, geometric AOA and base excitation frequency.
- Find a suitable method to analyse the fluid structure interaction occurring in the ACC unit. A mesh-based, analytical and meshless FSI simulation are weighed up according to their accuracy, robustness and computational cost to find the optimal method.

## 1.6 Project scope

This project is limited to the numerical investigation of the experiment carried out by Basson (2015). No further experimental analysis will be carried out nor will any design changes be made to the fan blade. Simulating the rotating fan in the ACC is beyond the scope of this project.

## 1.7 Report structure

As mentioned, the report focuses on the numerical investigation of the aerodynamic damping of an oscillating fan blade. The report is structured as follows:

**Chapter 2: Experimental background and the simulation domain**
Accurate simulation bounds have to be determined to accurately model the dynamic aeroelastic phenomena. Domain simplifications, boundary conditions and initial conditions are determined from the experimental measurements and set-up. Furthermore, experimental findings are stated that will be used to validate the numerical simulation. Lastly, additional observations of the experimental results are discussed.

**Chapter 3: Development of the mathematical and numerical model**
The mathematical model is derived from the occurring physical phenomena to numerically solve the governing equations.

**Chapter 4: Mesh-based FSI analysis**
Mesh based methods are used to simulate the aerodynamic damping of the oscillating fan blade. An in depth analysis of the flow and structural behaviour is covered. This includes the explanation of aerodynamic effects and how these affect blade motion.

**Chapter 5: 1D beam model**
An Euler-Bernoulli beam model is coupled with a heuristic flow model to simulate the blade's response. The choice of flow models depends on the observed flow phenomena in chapter 4.

**Chapter 6: Meshless FSI analysis**
Mesh based methods have certain drawbacks. A different solution procedure is investigated using meshless methods. The results are compared with the experimental and mesh based FSI simulation results.

**Chapter 7: Conclusion**
Recommendations and important findings are summarised for the two FSI analyses and the 1D beam model.

# Chapter 2

# Experimental background and the simulation domain

A single axial fan blade was fixed to a base excitation mechanism as shown in figure 2.1 and tested under different flow conditions in a low speed wind tunnel (Basson, 2015). The aim of the numerical simulation is to replicate the dynamic response of the oscillating fan blade depicted in the figure.

The blade is oscillated at driving frequencies ranging from 0 to 2 times the blade's first natural bending mode frequency. The blade root is forced to oscillate in the flapwise direction by the motor driven crank with an amplitude of 1 mm. The blade's tip displacement was measured for different inlet velocities and AOAs. The obtained transmissibility curves are given in section 2.4 and will be used to validate the FSI simulations. Also, the structural and fluid model will be validated using further experimental findings from Basson (2015).

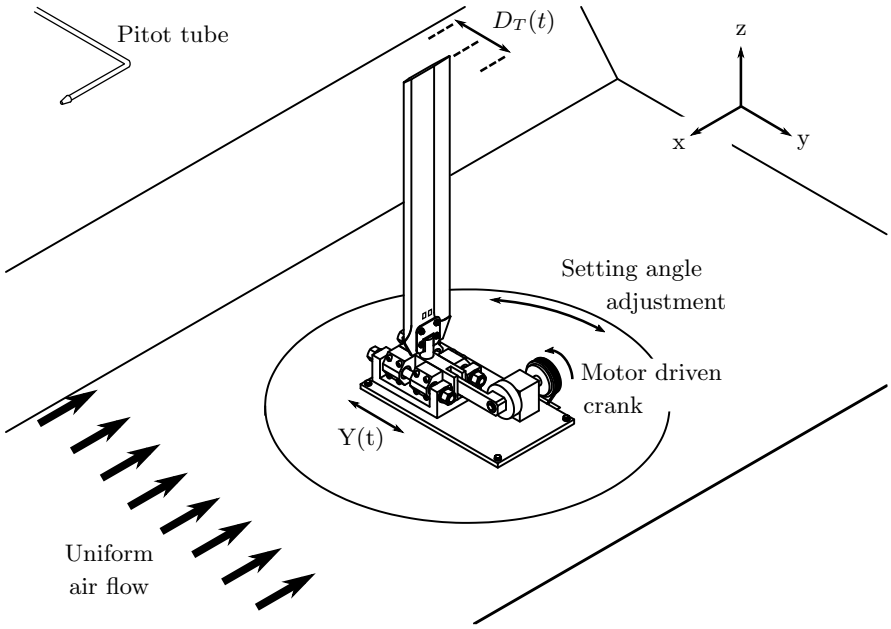


**Figure 2.1:** Experimental set-up in the Stellenbosch University low speed wind tunnel (Basson, 2015)

## 2.1 Considerations for the simulation domain

Due to the dynamic nature of the problem, the simulation is strongly time dependent. The dynamic response of the blade is greater than its static response, because the applied cyclic loading vibrates the blade close to resonance (Cook *et al.*, 2002).

The fluid is displaced during the motion of the structure and acts as a damping influence. Energy is transferred from the oscillating blade to the fluid (Schmucker *et al.*, 2010). These damping effects vary with time and position, which according to Mostafa (2009), make the loading highly non-linear.

Both the structure and fluid have to be modelled and included in the computational domain to accurately simulate their strong interaction. The structural and fluid model will be separately validated using available experimental data to ensure that they are set up correctly. This is followed by the validation of the FSI simulation.

## 2.2 Structural model and validation data

The investigated fan blade has a flat plate profile, similar to the one specified in Riegels (1961). The blade profile and geometry are depicted in appendix A.

The blade geometry was simplified to easily accommodate the fluid and structural discretization, but the solution accuracy was not affected, as shown in section 4.1. The following geometry alterations were performed:

- The bolted connections, indicated in figure 2.2, and their respective holes were removed and replaced by a mathematically rigid contact. The effect on the structural stiffness is negligible and has no effect on the fluid flow as it is excluded from the fluid domain.

- The base excitation mechanism will not be explicitly modelled. Rather, a harmonic displacement boundary condition will model the base excitation. An accelerometer was placed on the base excitation mechanism to confirm the sinusoidal excitation of the blade (Basson, 2015). As a result, accurate modelling by means of a displacement boundary condition is ensured.

The material properties of the blade were also obtained by Basson (2015). These are stated in table 2.1. The modulus of elasticity is decreased from the specified 74 GPa to 70 GPa to ensure that the first natural frequency of the blade model corresponds to that obtained experimentally. The altered modulus of elasticity lies within the specified range of 70 GPa to 80 GPa for aluminium 5083 out of which the blade is manufactured (Basson, 2015).

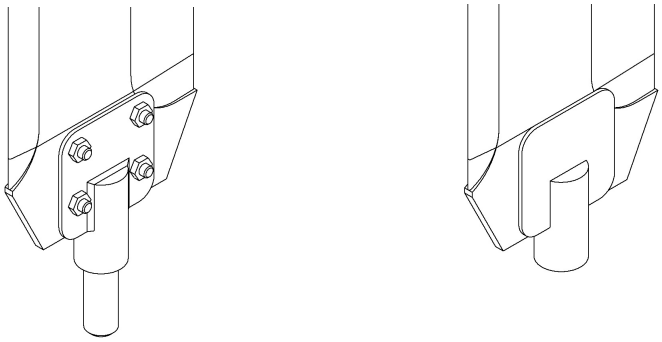

**(a)** Experimentally tested blade model

**(b)** Simplified numerical blade model

**Figure 2.2:** Structural model adjustments

The natural frequency and the structural damping of the blade will be verified using a modal analysis and a transient decay analysis respectively. Validation data is available from vacuum chamber tests that were performed by Basson (2015). The blade was placed in a vacuum chamber with the blade base fixed. Its tip was initially displaced by 2 mm and then released. The decaying motion was captured using strain gauges bonded to the blade root. The structural damping coefficient and the blade's natural frequency in vacuum are recorded in table 2.1. A 100 % vacuum was not achieved, but the blade's natural frequency and damping coefficient at vacuum could be extrapolated (Basson, 2015).

**Table 2.1:** Material and vibrational properties

| Blade: Aluminium 5083 | | |
|---|---|---|
| $\rho$ | 2700 | $kg/m^3$ |
| $E$ | 70 | GPa |
| $\nu$ | 0.34 | |
| Base: Steel 300W | | |
| $\rho$ | 7800 | $kg/m^3$ |
| $E$ | 205 | GPa |
| $\nu$ | 0.29 | |
| Vibrational properties | | |
| $f_V$ | 11.3255 | Hz |
| $\zeta_V$ | 0.001333 | |

## 2.3 Fluid model and validation data

The fan blade's profile was designed and manufactured to correlate with the obtained drag and lift coefficients for a flat plate profile given in Riegels (1961). Figure 2.3 shows the experimentally obtained lift- $C_L$ and drag coefficient $C_D$ for different AOAs and three different Reynolds numbers.

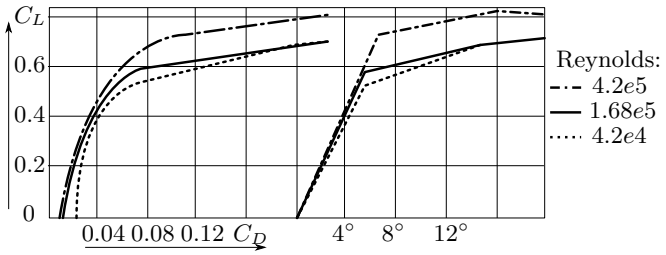


**Figure 2.3:** Lift and drag coefficients for a flat plate at different angles of attack (Riegels, 1961)

The Reynolds number is defined as:

$$Re = \frac{\rho\, U_{In}\, c}{\mu} \tag{2.1}$$

where the air density $\rho$ and dynamic viscosity $\mu$ are $1.184\,\mathrm{kg/m^3}$ and $1.849\times10^{-6}\,\mathrm{kg/ms}$ respectively. These air properties are based on atmospheric measurements performed by Basson (2015) prior to the experiment. The blade's characteristic length is given by its chord length $c$, which is 120 mm. The air inlet velocity $U_{In}$ ranges from 0 m/s to approximately 20 m/s. Riegels (1961) has given drag and lift coefficients for three different Reynolds numbers of which $1.68\times10^5$ closely corresponds to the maximum Reynolds number of the experiments performed by Basson (2015). Therefore, these drag and lift coefficients are used to validate the CFD simulation. The flow properties for the CFD validation are stated in table 2.2.

**Table 2.2:** Flow properties for the CFD validation

| | | |
|---|---|---|
| $\rho$ | 1.225 | $kg/m^3$ |
| $\mu$ | $1.7894 \times 10^{-5}$ | $kg/ms$ |
| $U_{In}$ | 20.45 | $m/s$ |

Cengel and Cimbala (2010) state that flow transition on a flat plate may occur at Reynolds numbers ranging from $1\times10^5$ to $3\times10^6$. The specific Reynolds number at which flow transition occurs depends on factors such as free stream turbulence and surface roughness. Section 4.2.1 discusses which turbulence or transition model is used for the simulation.

The CFD simulation has to meet the following criteria before a FSI simulation can be attempted:

**Replicate experimental results:** The CFD simulation has to accurately predict $C_L$ and $C_D$ at AOAs ranging from 0° to 8°. A steady state CFD simulation will be used as done by Brandsen (2013).

**Mesh independent:** The solution may not depend on the number of mesh cells. Thus, different meshes are compared in their ability to predict Riegels (1961) experimental lift and drag coefficients for the flat blade profile.

**Domain independent:** The flow has to fully develop around the oscillating blade without the domain boundaries influencing the solution. The Neumann or Dirichlet boundary conditions have to be placed at locations where they offer good approximations of the flow conditions (Versteeg and Malalasekera, 2007).

### 2.3.1 Fluid simulation domain

The fluid domain encompasses only the upper section of the oscillating fan blade. The gray shaded region in figure 2.5 is not contained within the fluid domain. The advantage is that the meshing procedure is simplified and the size of the computational domain is reduced without affecting the accuracy of the solution.

It is assumed that the blade can be modelled as a cantilever beam with a fixed base as shown in figure 2.4. Load $F$ represents the aerodynamic force at any location along the blade. The tip displacement decreases as load $F$ approaches the root of the blade, as shown by the following equation (Nisbett, 2011):

$$D_T = \frac{Fa^2}{6EI}\left(3L_{Bl} - a\right) \tag{2.2}$$

Therefore, the aerodynamic forces induced by the flow around the blade's base have a negligible effect on the tip displacement.

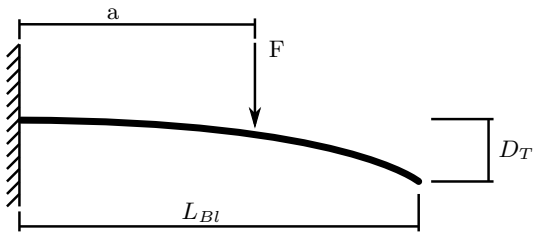


**Figure 2.4:** Cantilever beam with aerodynamic load $F$ at any point

The width, height and length of the domain have been adjusted to ensure that the simulation is domain independent. The smallest allowable domain is chosen for a fast FSI simulation. The sizes of the two different domains that were investigated, are compared in table 2.3 with the length scales indicated in figure 2.5.

**Table 2.3:** Fluid domains

| Length scale | Large domain | Small domain |
|---|---|---|
| Height [m] | 0.89 | 0.856 |
| Width [m] | 0.9 | 0.8 |
| Front [m] | 0.6 | 0.5 |
| Length [m] | 2.05 | 1.85 |

The boundary conditions (BCs) are indicated in figure 2.5. For the CFD simulation the blade surface is given as a wall BC. It is altered to a FSI interface when performing the FSI simulation.

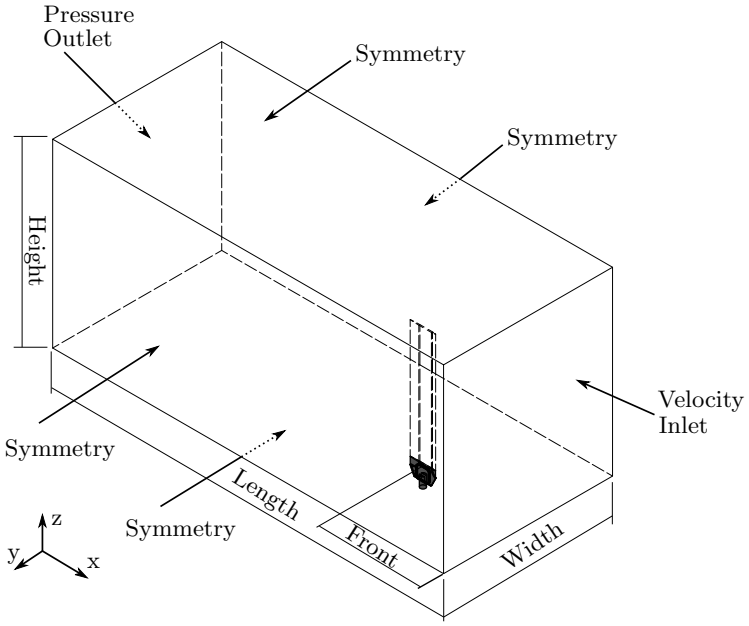


**Figure 2.5:** The fluid and structural domain combined

## 2.4 FSI validation data

Basson (2015) observed that the blade's aerodynamic loading depends on the geometric AOA, the relative angle between the blade and the flow direction and the air inlet velocity. The FSI simulation will only be performed for a geometric AOA of 0° and 9°. These two angles have been chosen for the following reasons:

**0AOA:** As stated by Basson (2015), the findings at 0 ° offer valuable insight, because the only factor that influences the blade displacement is the air velocity.

**9AOA:** For smaller geometric angles of attack, Basson (2015) found a positive correlation between it and the aerodynamic damping force. At 9AOA, this does not hold true for the maximum inlet velocity. Here, damping at 9 ° is less than that at 8 °. Basson (2015) also states that the motion transmissibility curves are less predictable. His assumption is that flow separation may be the reason for the unexpected vibrational characteristics. A FSI simulation at this AOA can give valuable information on these unpredicted vibrational characteristics of the blade.

The experimental tip displacements for 0AOA and 9AOA are depicted in figure 2.6. The FSI simulation will be performed for different frequency ratios $r$, which is the ratio between the driving frequency and the blade's natural frequency, to ensure that the peak tip displacement is determined.

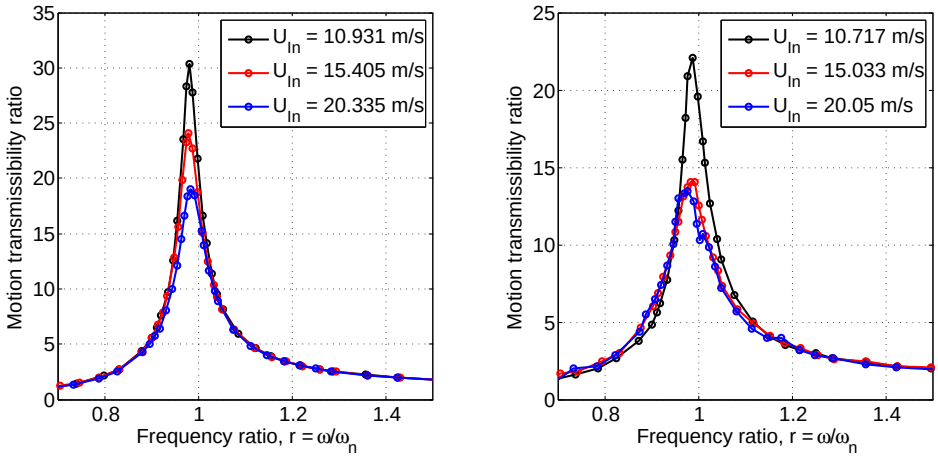


**(a)** 0AOA **(b)** 9AOA

**Figure 2.6:** Motion transmissibility ratio relative to the frequency ratio, for different geometric AOAs

### 2.4.1 Alterations performed on the structural and fluid model for FSI

The interface between the solid and fluid is either modelled implicitly or explicitly, as will be explained in section 3.1. For implicit modelling the entire domain is modelled as a continuum and the interface requires no special consideration. On the other hand, for explicit modelling the interface acts as a boundary between the fluid and structure. Information is transmitted be-

tween the two media in the form of boundary conditions (Bijl *et al.*, 2006). Other information necessary for the FSI simulation is stated in table 2.4.

**Table 2.4:** Required information for the FSI simulation

| General flow information | | |
|---|---|---|
| $\rho$ | 1.184 | $kg/m^3$ |
| $\mu$ | $1.849 \times 10^{-5}$ | $kg/ms$ |
| Blade's base excitation | | |
| $Y_x$ | $0.001\, sin\,(r\omega t)$ | m |
| $Y_y$ , $Y_z$ | 0 | m |

## 2.5 Additional observations from the experimental results

Using an FRF analysis, Basson (2015) determined the blade's first bending mode frequency to be 10.993 Hz and 11.3255 Hz in static air and in vacuum respectively. This is a noticeable deviation of 2.936 %. Assuming the blade can be modelled as a single degree of freedom system, the damped natural frequency can be written as:

$$\omega_{d,Air} = \sqrt{\frac{k_{Bl}}{m_{Bl} + m_{AM}}\,(1 - \zeta^2)} \tag{2.3}$$

where $k_{Bl}$ and $m_{Bl}$ are the blade's stiffness and mass respectively. The blade's damped natural frequency is reduced if the added mass of the air $m_{AM}$ or the damping coefficient $\zeta$ are increased.

As discussed by Basson (2015), the shift in natural frequency can be explained by the added mass effect. This phenomenon occurs if the structure is submerged in a fluid. The motion of the blade has to displace the fluid and thus the structure is subjected to a counteracting inertial force. The added mass effect is of importance if the fluid density is comparable to that of the structure (Harris and Piersol, 2002), which could be the case as the blade is manufactured out of aluminium.

The blade's natural frequency is not only influenced by the mass of the system, but also by its damping and stiffness as shown by equation (2.3). The stiffness of the system can be altered by centrifugal stiffening as observed by Brandsen (2013). Centrifugal forces or other stiffening mechanisms are not present and thus the blade's stiffness is not altered. The system's damping on the other hand is altered for different AOAs and flow velocities. Basson (2015) specifies a $\zeta$ value for each simulation that ranges from 0 to 0.04, at no inlet velocity and maximum inlet velocity, at 8AOA respectively. Substituting these values into equation (2.3) gives negligible variations of the natural frequency.

This suggests that the shift in natural frequency mainly depends on the added mass effect.

The frequency ratio at which the maximum tip displacement occurs $r_P$, varies with the inlet velocity as shown in figure 2.7. $r = 1$ corresponds to the blade excitation frequency being equal to the first natural frequency of the blade in vacuum.

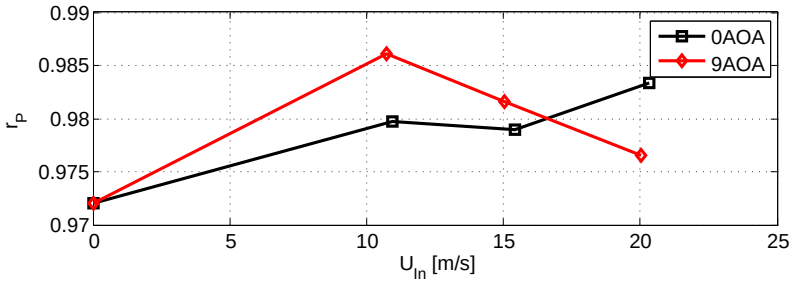


**Figure 2.7:** Blade's $r_P$ vs. inlet flow velocity

The following observations can be made from the figure:

**0AOA:** $r_P$ increases as the inlet velocity is increased, but remains below unity. The mass of the system inversely affects the natural frequency as shown in equation (2.3). This means that the added mass effect is most noticeable for blade oscillation in the static fluid, due to the relatively large deviation of $r_P$ from unity. The added mass effect is reduced as the flow velocity increases, because the blade's flapwise acceleration decreases. The relationship of the blade's acceleration and the added mass effect is discussed in greater detail in section 5.2.3.

**9AOA:** For a moving fluid, the added mass effect is dependent on the relative acceleration between the blade and the air. As shown in section 5.2.3, the blade's experienced added mass increases due to an increased relative acceleration between the blade and air as the inlet velocity is increased, when the blade is set at an angle. Therefore, the peak frequency ratio decreases as the flow velocity increases from 10 m/s to 20 m/s.

The aerodynamic lift force is given as (Cengel and Cimbala, 2010):

$$F_L = 0.5\,\rho\,C_L\,A\,U_{Rel}^2 \tag{2.4}$$

where $\rho$ is the air density, $C_L$ is the lift coefficient, $A$ is the planform area of the blade and $U_{Rel}$ is the relative velocity of air over the blade. Equation (2.4) indicates that the aerodynamic force is proportional to the square of $U_{Rel}$, but the 0 ° transmissibility curve shows a linear decrease in tip displacement as the inlet velocity is increased. This trend is shown in figure 2.8 and will be explained in section 2.5.1. This linear relationship is not observed

for the 9AOA case as shown in the figure. An increase of the flow velocity from 15 m/s to 20 m/s does not have a significant influence on the tip displacement. As Basson (2015) suggested, more complex flow phenomena influence the aerodynamic damping, which will be analysed in chapter 4.

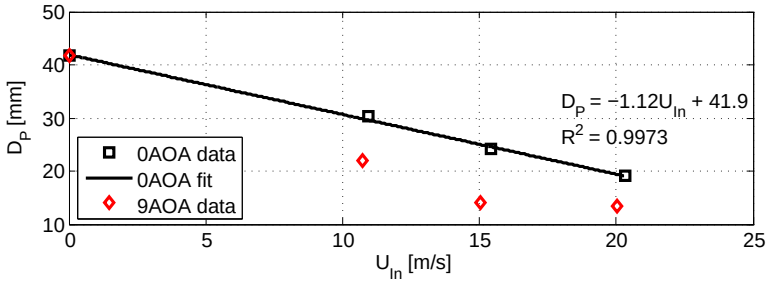


**Figure 2.8:** Blade's peak tip displacement vs. inlet flow velocity

### 2.5.1 Effective AOA and relative flow velocity

The geometric AOA is the blade setting angle prior to blade oscillation. If there is no blade vibration then the relative angle between the blade and the flow direction is given by the geometric AOA. This does not hold true as the blade starts to vibrate.

In equation (2.4) the lift force is calculated using the relative velocity between the air and the blade. Similarly, $C_L$ is a function of the relative angle, referred to as effective AOA. From figure 2.9 the relative air velocity components can be determined as:

$$U_{Rel,x'} = U_{In} \cos(\alpha_G) \tag{2.5}$$

$$U_{Rel,y'} = -U_{Bl} + U_{In} \sin(\alpha_G) \tag{2.6}$$

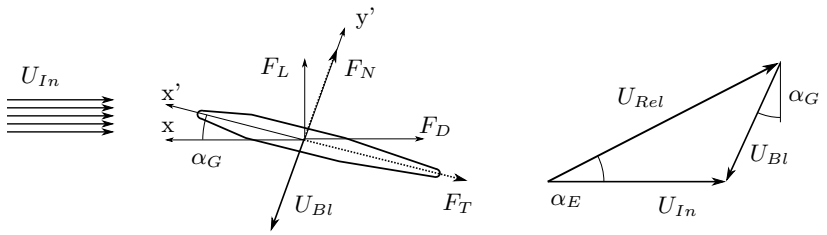


**Figure 2.9:** Effective angle of attack

The blade's flapwise deflection $D_{Bl}$ and velocity $U_{Bl}$ vary with time and spanwise location as indicated in figure 2.10. At instances $t_1$ and $t_3$, the blade reaches its maximum displacement and therefore its velocity is minimum. On the other hand, $U_{Bl}$ is maximum at $t_2$ and $t_4$.

The effective AOA grows proportionally with the blade velocity everywhere along the blade except at the blade tip. Here, it decreases due to downwash as shown in the figure. This phenomena is described in section 4.4.2.

The relative fluid velocity and the effective AOA are therefore dependent on time and position. The effective AOA is obtained by the following equation:

$$\alpha_E\left(z,t\right) = \tan^{-1}\left(\frac{U_{Rel,y'}}{U_{Rel,x'}}\right) \tag{2.7}$$

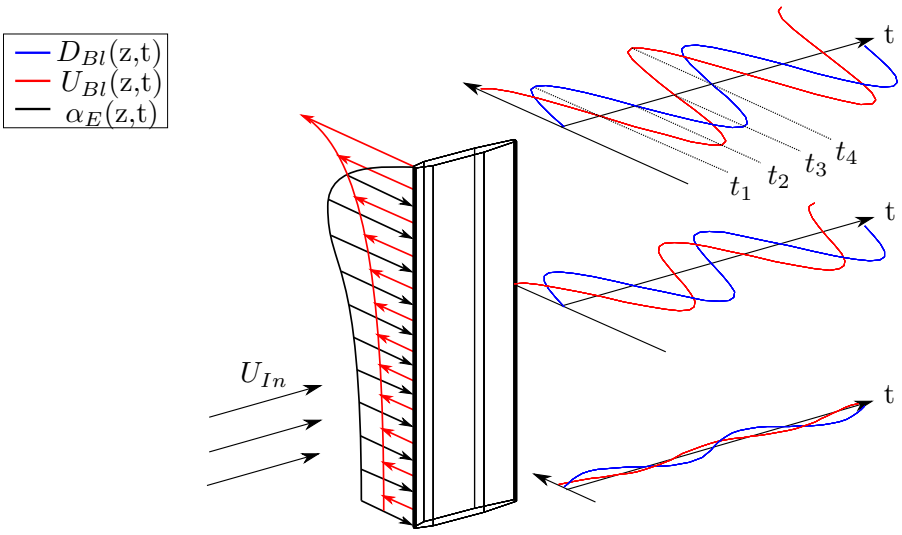


**Figure 2.10:** $D_{Bl}$ and $U_{Bl}$ are dependent on the time instance and the spanwise location. The maximum blade velocity is reached at the blade tip when the tip displacement is zero

In the previous section it was stated that the tip displacement varies linearly with respect to the inlet velocity, if the geometric AOA is zero. As the inlet velocity is increased, the relative air velocity increases, but the effective AOA decreases. Assuming potential flow, an infinite aspect ratio and a small effective AOA, equation (2.4) can be rewritten as:

$$F_L = 0.5\,\rho\,A\,2\pi\tan^{-1}\left(\frac{U_{Bl}}{U_{In}}\right)\left(U_{In}^2+U_{Bl}^2\right) \approx 0.5\,\rho\,2\pi\,\frac{U_{Bl}}{U_{In}}\,A\,\left(U_{In}^2+U_{Bl}^2\right) \tag{2.8}$$

The blade velocity is negligible compared to the inlet velocity and thus the lift force can be approximated as:

$$F_L \approx 0.5\,\rho\,A\,2\pi\,U_{In}\,U_{Bl} \tag{2.9}$$

Thus, a linear correlation exists between the aerodynamic loading and the inlet velocity. The tip displacement therefore decreases linearly with an increase in inlet velocity.

# Chapter 3

# Development of the mathematical and numerical model

This chapter forms the mathematical foundation for the following chapters. Firstly, the fundamentals of a FSI simulation are discussed, which is followed by a derivation of the fluid and structural model's governing equations. The last section covers the implicit and explicit discretization methods.

## 3.1 Fundamentals of computational fluid structure interaction (FSI)

The fluid and structural domains are governed by different physical laws, which have to be solved simultaneously or in series to achieve an accurate representation of the fan blade motion. This section describes how the different governing equations (GEs) are combined into a set of system equations. The two different approaches of solving FSI problems are:

**The monolithic approach:** This approach combines the governing equations of the fluid and structure into a single system equation. This means that the structure and fluid GEs are solved simultaneously (Hou *et al.*, 2012).

The interface conditions between the solid and fluid are implicitly incorporated in the algorithm and the problem is treated as a single continuum. This eliminates the problem of treating the interface and interaction between solid and fluid explicitly (Hron and Turek, 2006), which can be problematic and introduce errors in the simulation. However, the monolithic approach introduces additional nonlinearity into the resulting system of equations (Wick, 2011).

For mesh-based methods, the GEs of the fluid and structure are described in the Eulerian and Lagrangian reference frame respectively. This means that the monolithic approach requires a mixed description. The arbitrary Lagrangian-Eulerian (ALE) framework offers this possibility and is used in the monolithic approach to solve FSI problems (Hron and Turek, 2006). This approach is complicated (Liu and Liu, 2003) and requires special expertise and time to develop the numerical algorithm. The advantages on the other hand are that more stable simulations are obtained (Liu and Liu, 2003) and the simulation results are potentially more accurate (Hou *et al.*, 2012). The solver can also be computationally more efficient, because no tracking of the interface is required and no interface conditions have to be computed explicitly.

**The partitioned approach:** The GEs of the structure and fluid are separately integrated in time (Bijl *et al.*, 2006). This allows for different discretizations and numerical algorithms to be used for each medium. The information between the two is then explicitly communicated using the interfacial conditions (Hou *et al.*, 2012). The interface acts as a boundary for the fluid and structural domain. The interfacial conditions are explicitly applied as boundary conditions on each domain in a staggered or asynchronous manner in time (Bijl *et al.*, 2006). The fact that the partitioned approach splits the structural and fluid solvers, means that their systems of equations are not solved simultaneously, but rather in series. This allows for a staggered solution procedure (Gatzhammer, 2008). The two solvers communicate with each other using either the weak or strong coupling schemes discussed in the following subsection.

A staggered solution procedure reduces the cost of solving the overall system of equations, because the computational cost linearly correlates to the number of unknowns (Gatzhammer, 2008).

The partitioned approach makes use of already developed numerical algorithms of each discipline and combines them. This allows the use of sophisticated and validated structural and fluid dynamic codes and thus reduces the development time of the algorithm. The aim is to combine the algorithms in a manner so that they function efficiently together and give accurate results. The interface location between the structure and fluid usually varies with time and has to be determined continuously. This is a cumbersome process and often introduces errors in the simulation (Hou *et al.*, 2012).

### 3.1.1 One way vs. two way coupling

For the partitioned approach, there are one way and two way coupling schemes. These describe the exchange direction of interface information between the two partitioned solvers.

One way coupling refers to a procedure where interface information is only transferred from one solver to the other and not vice versa (Raja, 2012). Two way coupling is used when the motion of each medium influences that of the other. In the case of the aerodynamic damping of the oscillating fan blade, the blade motion is damped by the air flow and that in turn produces flow fluctuations. Due to the strong interaction of both fluid and structure, one way coupling would not capture the physical phenomena accurately.

The two way coupling process can either be categorized by the weak or strong coupling scheme. Both are discussed in the following subsection.

### 3.1.2 Weak and strong coupling schemes

The weak and strong coupling schemes only apply to the partitioned approach, because the interface position has to be tracked explicitly using either the strong or weak coupling scheme.

The weak (explicit) coupling method only requires a single fluid and structure solve per time step (Bijl *et al.*, 2006). This makes the method efficient, but it can lead to the divergence of the simulation. This is especially problematic when the dynamics of the fluid and structure significantly affect the interaction (Bijl *et al.*, 2006). The stability problems can be reduced by limiting the time step size.

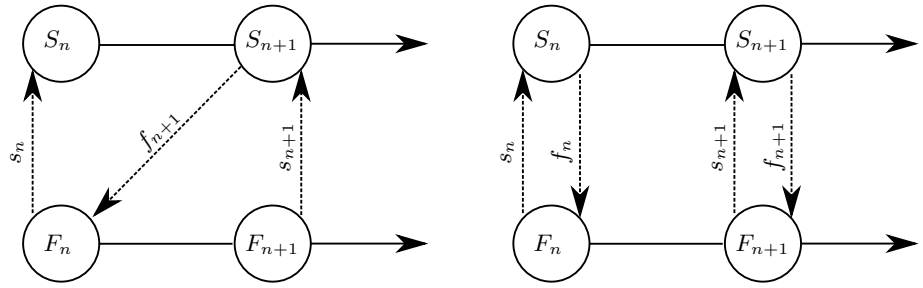


**(a)** Weak coupling scheme **(b)** Strong coupling scheme

**Figure 3.1:** Two different types of coupling schemes

The **weak (explicit) coupling scheme** is depicted in figure 3.1a. Solver F and Solver S represent the separate fluid and structural solver. Interface values are computed and communicated to the other solver so that it can progress to the next time step (Gatzhammer, 2008). The following lists the series of steps taken in the weak coupling scheme as depicted in figure 3.1a.

**Step 1:** The structural solver (or fluid solver) computes its next time step $S_{n+1}$ using given initial conditions and boundary conditions.

**Step 2:** The structural solver then transfers interface displacement information ($f_{n+1}$) to the fluid solver.

**Step 3:** Using the interface conditions and other boundary conditions the fluid solver progresses to $F_{n+1}$.

**Step 4:** This time the updated interface conditions ($s_{n+1}$) from the fluid solver are fed back to the structural solver. The structural solver receives the aerodynamic forces on the interface.

**Step 5:** The process is restarted at Step 1 until the simulation end time has been reached.

The **strong (implicit) coupling scheme** uses multiple fluid and structure iterations, called stagger iterations, per time step. The exchange of interface information is stopped once the coupled solution fully converges at the time step (Bijl *et al.*, 2006).

Figure 3.1b shows the strong coupling method and each step of the solver is listed below.

**Step 1:** The process is started with the computation of the interface values using the structural solver. A first estimate of the structural displacement is then communicated to the fluid solver. The fluid solver then computes a new prediction of the aerodynamic loading and feeds the information to the structural solver. The process is repeated using the newest interface predictions. This loop is terminated once the interface values of both solvers have converged.

**Step 2:** With Step 1 completed both solvers can progress to the new time step. Step 1 is then repeated at the new time step.

The strong coupling method can become computationally expensive, but ensures stability as mentioned by Gatzhammer (2008). This implicit method also allows for larger time steps due to its stability.

Important to note is that an explicit coupling scheme does not prohibit the use of an implicit solver for the internal solution procedure. The statement also holds for an implicit coupling scheme. Both systems may be solved implicitly in time and coupled by either an implicit or explicit coupling scheme (Gatzhammer, 2008). Explicit and implicit methods are discussed in section 3.3.

Another advantage of the partitioned method is subcycling. Usually the time step is more restricted for the fluid solver than for the structural solver due to stability reasons (Gatzhammer, 2008). Subcycling allows for different time steps to be taken by each solver. The fluid solver can perform several non-coupled time steps, called subcycles, in between two coupled time steps. This can be combined with either the weak or strong coupling schemes.

Tooley (2012) states that ANSYS 14.0, a commercial mesh-based solver that will be used in chapter 4, uses an iterative implicit scheme to compute the interface values between the two separate solvers. ANSYS couples Fluent and ANSYS Mechanical, which are both highly developed CFD and FEM solvers.

## 3.2 Governing equations

This section focuses on the development of governing equations for the partitioned FSI approach. If the monolithic approach is used then additional non-linearities are introduced in the system of equations (Wick, 2011) and the whole system is non-linear.

Firstly the Eulerian and Lagrangian reference frame will be discussed. The governing equations of the fluid and structure are then derived.

### 3.2.1 Eulerian and Lagrangian reference frame

The formulation of the governing equation depends on the position of the observer (Gatzhammer, 2008). The two possible reference frames that the observer can take are discussed below.

**Eulerian reference frame:** This frame of reference is not interested in the motion of a single object, but rather in the motion through a control volume. The observer has an external reference frame positioned away from the control volume. The interest of the observer lies with describing the changes of the field variables in the desired region by describing the motion of objects moving through it (Gatzhammer, 2008).

This reference frame is usually used for mesh-based fluid dynamics. A fixed mesh does not distort due to large deformations of the moving material, which usually occurs during fluid motion (Liu and Liu, 2003).

**Lagrangian reference frame:** The observer is interested in the motion of a single object. Therefore, the Lagrangian reference frame is fixed to the object in motion, which means that the reference frame varies in time.

This reference frame is used for the finite element method (FEM), which is generally used for numerically solving structural mechanics problems. The object is discretized into smaller elements using a mesh. The mesh cells track the structural mass they represent and therefore deform and move with the structure.

### 3.2.2 Fluid dynamics

This subsection covers the development of the fluid governing equations based on physical laws. Fluid model simplifications and assumptions are stated in appendix B. The Navier-Stokes equation is the governing equation for fluid dynamics. It is stated with additional conservation laws in the Eulerian perspective.

#### 3.2.2.1 Mass conservation

An additional equation is introduced for methods using the Eulerian reference frame to ensure the conservation of mass. It is implicitly ensured for methods where the mass of the object is continuously tracked by the mesh or particles. Thus, an additional conservation law is not required in numerical methods such as FEM or Smoothed Particle Hydrodynamics (SPH).

Mass conservation is based on the fact that mass is neither destroyed nor created. For a fluid element this means that the rate of mass increase within the element is equal to the net rate of mass flow into the element (Versteeg and Malalasekera, 2007). For this investigation, the control volume is fixed and the fluid can be assumed incompressible, as shown in appendix B. The rate of mass increase in the control volume is therefore zero:

$$\frac{\partial m}{\partial t} = \frac{\partial}{\partial t}\left(\rho dV\right) = 0 \tag{3.1}$$

This means that the mass flow rates across the boundaries have to equal zero. In tensor notation, this is given by:

$$\sum_{i=1}^{3} \rho \frac{\partial\left(U_i\right)}{\partial x_i} = 0 \tag{3.2}$$

where $i$ takes the values one to three to indicate the three-dimensional coordinates.

#### 3.2.2.2 Momentum conservation

According to Newton's second law, an object's rate of momentum is equal to the sum of forces acting on the object. Using the Reynolds transport theorem, as done by Gatzhammer (2008), Newton's second law can be written as:

$$\int_V \left( \frac{\partial\left(\rho U_i\right)}{\partial t} + \frac{\partial\left(\rho U_i U_j\right)}{\partial x_j} \right) dV = \sum F_i \tag{3.3}$$

The forces acting on the object can either be body or surface forces. Body forces, such as gravity or centrifugal forces, are acting on the entire fluid element. Gatzhammer (2008) gives the body force as:

$$F_{B,i} = \int_V \rho f_{B,i} dV \tag{3.4}$$

where $f$ is the distributed force acting on the entire fluid element. Pressure and viscous forces are surface forces acting on the surfaces of the element (Versteeg and Malalasekera, 2007):

$$F_{S,i} = \int_S \sigma_{ij} n_j dS \tag{3.5}$$

where the surface stress tensor $\sigma$ is composed of the pressure $p$ and the stress tensor $\tau$. The surface stress tensor for the fluid element is given by:

$$\sigma = \begin{pmatrix} -p + \tau_{11} & \tau_{12} & \tau_{13} \\ \tau_{12} & -p + \tau_{22} & \tau_{23} \\ \tau_{13} & \tau_{12} & -p + \tau_{33} \end{pmatrix} \tag{3.6}$$

The diagonal entries of the stress tensor $\tau$ are the normal stresses acting on the element. The off-diagonal entries are shear stresses. The matrix has to be symmetrical, because the fluid element is in torsional equilibrium (Gatzhammer, 2008).

Substituting the forces back into equation 3.3 results in:

$$\int_V \left( \frac{\partial (\rho U_i)}{\partial t} + \frac{\partial (\rho U_i U_j)}{\partial x_j} \right) dV = -\int_S p n_i dS + \int_S \tau_{ij} n_j dS + \int \rho f_{B,i} dV \tag{3.7}$$

The surface integrals can be rewritten into volume integrals and then cancelled throughout equation 3.7. Knowing that the density is constant and using the continuity equation, the final momentum equation is:

$$\rho \left( \frac{\partial U_i}{\partial t} + U_j \frac{\partial U_i}{\partial x_j} \right) = -\frac{\partial p}{\partial x_i} + \frac{\partial \tau_{ij}}{\partial x_j} + \rho f_{B,i} \tag{3.8}$$

#### 3.2.2.3 Navier-Stokes Equation

The Navier-Stokes equation is a further simplification of the momentum equation. The fluid is assumed to be Newtonian and isotropic as stated in appendix B. Furthermore, the stress tensor is symmetric and therefore six out of nine viscous stress components are independent in a three-dimensional fluid element. The diagonal entries according to Versteeg and Malalasekera (2007) are:

$$\tau_{ii} = 2\mu \frac{\partial U_i}{\partial x_i} + \lambda \sum_{j=1}^{3} \left( \frac{\partial U_j}{\partial x_j} \right) \tag{3.9}$$

here $i$ and $j$ range from one to three, representing the three-dimensional coordinates. The second part on the right hand side equals to zero, because of the incompressible continuity equation 3.2. The diagonal entries are reduced to:

$$\tau_{ii} = 2\mu \frac{\partial U_i}{\partial x_i} \tag{3.10}$$

The off diagonal entries are given by:

$$\tau_{ij} = \tau_{ji} = \mu \left( \frac{\partial U_i}{\partial x_j} + \frac{\partial U_j}{\partial x_i} \right) \tag{3.11}$$

Substituting the simplified stress tensor into 3.8 yields the incompressible Navier-Stokes equation:

$$\rho\left(\frac{\partial U_i}{\partial t}+U_j\frac{\partial U_i}{\partial x_j}\right)=-\frac{\partial p}{\partial x_i}+\mu\left(\frac{\partial^2 U_i}{\partial x_i^2}+\frac{\partial^2 U_i}{\partial x_j^2}+\frac{\partial^2 U_i}{\partial x_k^2}\right)+\rho f_{B,i} \tag{3.12}$$

The only body force $f_{B,i}$ that needs to be considered is the gravitational force acting in the downward direction.

### 3.2.3 Structural dynamics

In this subsection the structural governing equation is developed. This is done by first stating why a linear model is feasible. A simple single degree of freedom system will then be explained and expanded to a multiple degree of freedom system. Features of the mass, damping and stiffness matrix will be covered in appendix B.

#### 3.2.3.1 Linear structural solver

Non-linear analysis is computationally more expensive and requires an iterative process to determine the node displacements. The structural model can be non-linear for several reasons (Cook *et al.*, 2002):

**Material non-linearity:** The strain in the material is linearly related to the applied stress, if the material does not exceed its yield strength. Stress oscillations below the yield strength will lead to no permanent deformation of the structure. This is only true if the oscillation count is too small to be considered for fatigue. The material will be plastically deformed if a stress greater than the yield strength is applied. The fan blade showed no permanent plastic deformation after the experiments were carried out and therefore the material properties can be considered as linear.

**Contact non-linearity:** This occurs if the contact area between two parts changes as the contact force varies or if sliding occurs with frictional forces.

A motor oscillates the blade in the flapwise direction by sliding the blade support over two parallel rails as shown in figure 2.1. Coulomb friction will counteract the forced motion and will make the model non-linear. As mentioned in section 2.2, the base excitation mechanism will not be directly modelled and thus non-linearities are not introduced into the structural system.

**Geometric non-linearity:** Large deformations may lead to the dependency of the equilibrium equations on the deformed structural geometry. The largest blade deflection was measured to be 41.96 mm (Basson, 2015). This is less than 10 % of the blade's length and is deemed small enough to be modelled linearly.

**Non-linear loading:** The aerodynamic loading on the structure is non-linear due to its dependency on time and blade position. For the partitioned FSI approach, information from one solver is transferred to the next before it commences its new calculation step. This means that the transferred information is assumed constant throughout the calculation step. The aerodynamic loading is therefore constant for each calculation of the structural solver and does not require a non-linear solver.

As stated, the non-linearities are either non-existing or can be circumvented and the use of a linear structural solver is applicable.

#### 3.2.3.2 Single degree of freedom system

Modelling the blade as a single degree of freedom (SDOF) system is inaccurate, but explains the fundamental theory. The model is expanded to a multiple degree of freedom (MDOF) system in the next section.

The damped SDOF system of the blade is visualised in figure 3.2a. It consists of a point mass $m_{Bl}$ representing the blade's mass, a linear spring with stiffness $k_{Bl}$ and a viscous damper $c_{Bl}$. An assumption is made that a viscous model is sufficiently accurate to model the occurring energy dissipation for mathematical convenience (Inman, 2014). Newton's second law can be used to determine the motion $D(t)$ of the SDOF system by setting up an equilibrium equation. Here, a base excitation is transmitted through the spring and viscous damper and sets the mass in motion (Cook *et al.*, 2002). The driving force is harmonic:

$$F_{Ext}(t) = F_0 \cos \omega t \tag{3.13}$$

where $F_0$ represents the amplitude of the excitation and $\omega$ is the base excitation driving frequency. Setting up the equilibrium equation for the SDOF system results in:

$$m_{Bl}\,\ddot{D} + c_{Bl}\,\dot{D} + k_{Bl}\,D = F_0 \cos \omega t \tag{3.14}$$

Dividing by the mass leads to:

$$\ddot{D} + 2\,\zeta\,\omega_n^2\,\dot{D} + \omega_n^2\,D = f_0\,cos\,\omega t \tag{3.15}$$

where $\omega_n$ is the undamped natural frequency of the system:

$$\omega_n = \sqrt{\frac{k_{Bl}}{m_{Bl}}} \tag{3.16}$$

and $f_0 = F_0/m_{Bl}$ is the mass normalised force. $\zeta$ is the damping coefficient. Using the method of undetermined coefficients as described in Inman (2014) the particular solution is:

$$D_p(t) = D_{p,0}\,cos\,(\omega t - \varphi_2) = \frac{f_0}{\sqrt{\left(\omega_n^2 - \omega^2\right)^2 + \left(2\zeta\omega_n\omega\right)^2}}\,cos\,(\omega t - \varphi_2) \tag{3.17}$$

The total solution is:

$$D(t) = A_1 e^{-\zeta\omega_n t} sin\,(\omega_d t + \varphi_1) + D_{p,0}\, cos\,(\omega t - \varphi_2) \tag{3.18}$$

From equations 3.17 and 3.18 the following can be seen:

- As the driving frequency of the motor approaches the natural frequency of the blade, the vibration gets very large for an undamped system. This is described by Inman (2014) as resonance. This means that modelling the blade without viscous damping $c_{Bl}$, would lead to an indefinite increase in blade displacement. The blade's tip displacement is finite and therefore an undamped model is not sufficient.
- A phase shift occurs between the forced response and the motion of the mass. This is mathematically expressed using $\varphi_1$ and $\varphi_2$.
- The negative exponential term of the homogeneous solution reduces the amplitude to zero. If the system's damping is large, then it dies out very quickly. That is why the homogeneous solution is called the transient response (Inman, 2014). This is advantageous, because we are interested in the steady state motion of the oscillating fan blade.
- The particular solution is called the steady state response, as its amplitude stays constant with time. The amplitude does not approach infinity as the driving frequency approaches the natural frequency of the blade. The amplitude is finite and depends on the damping coefficient. The smaller $\zeta$ is, the greater the vibrational response, if the natural frequency and driving frequency are approximately equal.

The normalised amplitude $D_{p,0}\,\omega_n^2/f_0$ of the steady state response is plotted against the frequency ratio $r = \omega/\omega_n$ in figure 3.2b. The figure shows an amplitude increase as $r$ approaches 1 and $\zeta$ decreases. Another important fact is that the motion of the mass and the driving motion are 90 ° out of phase at $r \approx 1$. This describes resonance for a damped system (Inman, 2014).

The previous discussion was focused on an applied force. A better representation of the applied motion through the motor can be achieved by modelling it as a base excitation as shown in figure 3.2a and mathematically expressed as:

$$m_{Bl}\,\ddot{D} + c_{Bl}\,\dot{D} + k_{Bl}\,D = c_{Bl}\,\dot{Y} + k_{Bl}\,Y \quad \text{with} \quad Y(t) = Y_0\,\sin\,\omega t \tag{3.19}$$

The inertia force depends on the absolute acceleration of the mass while the elastic and damping forces depend on the relative motion between the base and the mass.

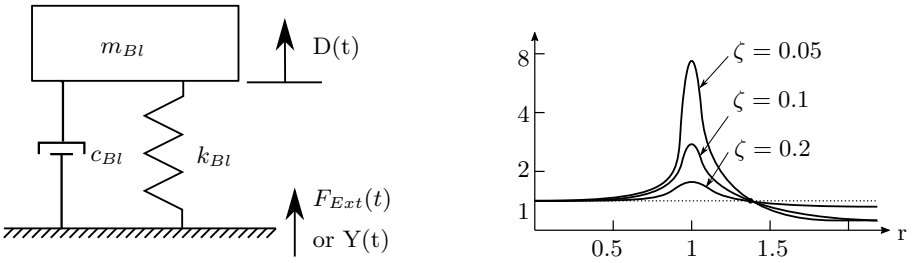


**(a)** Damped single degree of freedom system

**(b)** Normalised amplitude vs. frequency ratio

**Figure 3.2:** Harmonically excited single degree of freedom system

#### 3.2.3.3 Multiple degree of freedom system

The blade model has to be discretized into a finite set of discrete elements to numerically approximate the blade's dynamic behaviour. This introduces a discretization error that can be minimised by increasing the number of structural nodes that resemble the blade. For that reason, the SDOF system inaccurately models the blade motion and is expanded to a MDOF system.

Setting up the equilibrium equation at each node results in a global system of equations. The unknowns to be solved are the nodal degrees of freedom that govern the spatial variation of the field variables (Cook *et al.*, 2002). Equation 3.14 can simply be expanded as shown by Cook *et al.* (2002) to give:

$$\boldsymbol{M}\ddot{\boldsymbol{D}} + \boldsymbol{C}\dot{\boldsymbol{D}} + \boldsymbol{K}\boldsymbol{D} = \boldsymbol{F}_{Ext} \tag{3.20}$$

The mass matrix $\boldsymbol{M}$ is a discrete representation of the continuous mass distribution (Cook *et al.*, 2002). $\boldsymbol{C}$ is the global damping matrix and $\boldsymbol{K}$ is the global stiffness matrix. The three matrices are discussed in appendix B.

$\boldsymbol{D}$ consists of all nodal degrees of freedom (DOF) in the structure and is a $n \times 1$ vector called the displacement vector. Here, $n$ is the total number of degrees of freedom. The externally applied forces are stored in the force vector $\boldsymbol{F}_{Ext}$ which is also an $n \times 1$ vector.

## 3.3 Implicit and explicit discretization

Equation (3.20) has to be discretized in time and space. The spatial discretization is performed by splitting the structure into smaller elements and specifying the DOF at each node as was discussed in previous sections. Time discretization is performed by using the finite difference approximations (Cook *et al.*, 2002). The two different time discretization schemes are discussed in this section.

### 3.3.1 Explicit discretization

In this discretization scheme, the nodal DOF at the new time step are only determined from historical information (Cook *et al.*, 2002):

$$\boldsymbol{D_{n+1}} = f\left(\boldsymbol{D_n}, \dot{\boldsymbol{D}}_{\boldsymbol{n}}, \ddot{\boldsymbol{D}}_{\boldsymbol{n}}, \boldsymbol{D_{n-1}}...\right) \tag{3.21}$$

This time-marching method has the disadvantage of being only conditionally stable, which means it diverges as soon as the critical time step $\Delta t_{Cr}$ is exceeded. $\Delta t_{Cr}$ is a restriction on the maximum time step and is small compared to the time step taken in implicit schemes. This means that many time steps have to be performed to complete the simulation, but each time step is calculated quickly as no matrix inversions are required. Therefore, this method is suited for wave propagation problems, which occur over a short time interval (Cook *et al.*, 2002). This makes the method unsuitable for this problem, because the blade requires a large simulation interval to reach steady harmonic motion.

### 3.3.2 Implicit discretization

The nodal DOF are not only calculated using historic information, but also require information from the current time step (Cook *et al.*, 2002):

$$\boldsymbol{D_{n+1}} = f\left(\dot{\boldsymbol{D}}_{\boldsymbol{n+1}}, \ddot{\boldsymbol{D}}_{\boldsymbol{n+1}}, \boldsymbol{D_n}, \dot{\boldsymbol{D}}_{\boldsymbol{n}}...\right) \tag{3.22}$$

This time-marching method is suited for structural dynamic problems where the loads vary slowly and the lower vibration modes dominate structural motion. The method is unconditionally stable and allows large time steps, but the time steps should be limited to fully capture the blade motion. ANSYS Inc. (2013*c*) suggests that the maximum time step is chosen so that:

$$\Delta t_{Max} \leq \frac{1}{20 f_{Max}} \tag{3.23}$$

where $f_{Max}$ is the frequency of the highest order mode that contributes to the dynamic motion of the blade. This guideline was followed by Brandsen (2013) whose investigation focused on the blade's oscillation close to its first bending mode. He thoroughly investigated the effect of altering the time step and found that a smaller time step does not alter the simulation response.

Similar to the research done by Brandsen (2013), the oscillating fan blade is excited close to its first bending mode. Therefore, $f_{Max}$ is set to be the blade's first bending mode frequency. This results in a time step size of 0.0044 seconds.

#### 3.3.2.1 Newmark method

The Newmark method is an implicit scheme that is used in ANSYS (ANSYS Inc., 2013*c*). This method is also used for the 1D model as it is second order accurate if numerical damping is implemented as done in equation (3.29) (Kim *et al.*, 2013). This section explains the procedure followed to solve equation (3.20) using the Newmark method. The first step is to determine $\boldsymbol{K}^{Eff}$:

$$\boldsymbol{K}^{Eff} = \frac{1}{\beta \Delta t^2}\boldsymbol{M} + \frac{\gamma}{\beta \Delta t}\boldsymbol{C} + \boldsymbol{K} \tag{3.24}$$

The numerical factors $\gamma$ and $\beta$ are discussed in greater detail in section 3.3.2.2. $\boldsymbol{K}^{Eff}$ is constant and can be predetermined if there are no non-linearities and $\Delta t$ stays constant. The nodal positions at the new time step can then be determined by solving:

$$\begin{aligned} \boldsymbol{K}^{Eff}\boldsymbol{D_{n+1}} &= \boldsymbol{F_{n+1}} \\ &+\boldsymbol{M}\left(\frac{1}{\beta \Delta t^2}\boldsymbol{D_n} + \frac{1}{\beta \Delta t}\dot{\boldsymbol{D}}_{\boldsymbol{n}} + \left(\frac{1}{2\beta} - 1\right)\ddot{\boldsymbol{D}}_{\boldsymbol{n}}\right) \\ &+\boldsymbol{C}\left(\frac{\gamma}{\beta \Delta t}\boldsymbol{D_n} + \left(\frac{\gamma}{\beta} - 1\right)\dot{\boldsymbol{D}}_{\boldsymbol{n}} + \Delta t\left(\frac{\gamma}{2\beta} - 1\right)\ddot{\boldsymbol{D}}_{\boldsymbol{n}}\right) \end{aligned} \tag{3.25}$$

The FEM solver receives force data from the CFD solver at the FSI interface, which are stored in $\boldsymbol{F_{n+1}}$ (Hou *et al.*, 2012). Other external loads, such as the base excitation, are also stored in $\boldsymbol{F_{n+1}}$. The new nodal velocities and accelerations are determined by:

$$\dot{\boldsymbol{D}}_{\boldsymbol{n+1}} = \frac{\gamma}{\beta \Delta t}\left(\boldsymbol{D_{n+1}} - \boldsymbol{D_n}\right) - \left(\frac{\gamma}{\beta} - 1\right)\dot{\boldsymbol{D}}_{\boldsymbol{n}} - \Delta t\left(\frac{\gamma}{2\beta} - 1\right)\ddot{\boldsymbol{D}}_{\boldsymbol{n}} \tag{3.26}$$

and

$$\ddot{\boldsymbol{D}}_{\boldsymbol{n+1}} = \frac{1}{\beta \Delta t^2}\left(\boldsymbol{D_{n+1}} - \boldsymbol{D_n} - \Delta t\dot{\boldsymbol{D}}_{\boldsymbol{n}}\right) - \left(\frac{1}{2\beta} - 1\right)\ddot{\boldsymbol{D}}_{\boldsymbol{n}} \tag{3.27}$$

respectively (Cook *et al.*, 2002).

#### 3.3.2.2 Numerical damping

The factors $\gamma$ and $\beta$ that are used in the Newmark equations influence the accuracy, stability and numerical damping of the simulation. The simulation is unconditionally stable if (Cook *et al.*, 2002):

$$2\beta \geq \gamma \geq \frac{1}{2} \tag{3.28}$$

For no numerical damping, $\beta$ and $\gamma$ are set to 0.25 and 0.5 respectively. A second order accurate implementation of numerical damping is done using the amplitude decay factor $\delta$ (ANSYS Inc., 2009) as follows:

$$\beta = \frac{1}{4}(1+\delta)^2 \quad \gamma = \frac{1}{2} + \delta \tag{3.29}$$

Numerical damping is required for the following reasons:

**High frequency numerical noise:** According to Howard and Cazzolato (2015) numerical damping is added to improve the stability of the simulation. The higher modes of the structure are not accurately modelled due to the restricted time step size. Therefore, higher frequencies of the structure can produce numerical noise that have to be damped using numerical damping (ANSYS Inc., 2009).

**Spurious vibrations:** Brandsen (2013) observed spurious vibrations, because his initial conditions were not set up correctly. He initially increased the damping of the system to remove the spurious vibrations. Bungartz and Mehl (2010) state that spurious vibrations can occur due to non-physical initial conditions. During the first time step the air is at rest and the structure moves. The air is then accelerated to the velocity of the structure within the first time step. The smaller the time step, the larger the fluid acceleration. This leads to a large fluid pressure pulse acting on the structure. In the next time step, the fluid is moving and the pressure pulse is absent. This introduces non-physical structural vibrations that can lead to spurious vibrations throughout the whole simulation if not properly damped (Bungartz and Mehl, 2010).

**Numerical diffusion:** The fluid mesh has to be adapted to the structural position at each time step. This requires mesh operations such as smoothing and remeshing. This means that the field variables have to be interpolated from the old mesh to suit the new mesh (Tiwari *et al.*, 2006*a*). This process introduces numerical diffusion, which artificially adds or subtracts energy from the system and thus degrades the simulation accuracy (Fries and Matthies, 2004).

**Displacement BCs:** ANSYS Inc. (2013*c*) state that a displacement boundary condition causes numerical noise, because the acceleration at the boundary is discontinuous. The discontinuity can already be observed from the velocity at the boundary nodes as shown in figure 3.3a. The figure shows that with no numerical damping the discontinuity persists. If numerical damping is used, the discrete approximation approaches the continuous function over time.

Bathe and Noh (2012) compare different implicit time integration schemes and show that with no numerical damping, the acceleration at the boundary node diverges. This is shown in figure 3.3b. This further supports the requirement for numerical damping if displacement BCs are used.

Howard and Cazzolato (2015) state that the exact value of $\delta$ depends on the system. For an accurate result, the energy being added to the system due to the above mentioned numerical errors has to equal the energy being

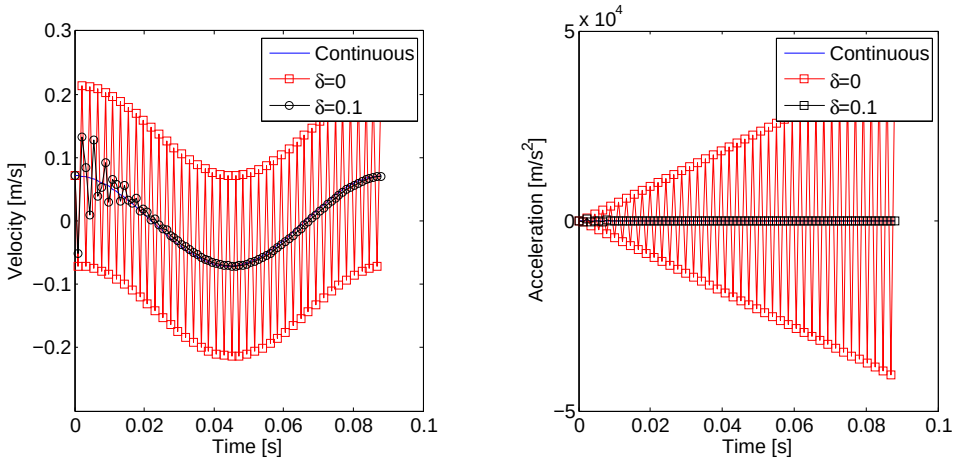


**(a)** Velocity of the boundary node for various methods

**(b)** Acceleration of the boundary node for various methods

**Figure 3.3:** Newmark velocity and acceleration approximation of the boundary node (Bathe and Noh, 2012)

dissipated by numerical damping. Furthermore, the artificial energy being added to the system might be small, but relatively large to the energy of the system. The blade is oscillated close to its natural frequency, which means that large deflections result from a small base excitation. This means that small deviations in the system's energy can lead to large errors.

The choice of the numerical damping model and the magnitude of $\delta$ can affect the accuracy of the solution (Howard and Cazzolato, 2015). Furthermore, the Newmark numerical damping scheme is time step size dependent and elongates the oscillation period (Craig and Kurdila, 2006).

ANSYS suggests setting $\delta = 0.1$ when using a time step that applies to equation (3.23) (ANSYS Inc., 2013*c*). An explicit time integration scheme can be used to circumvent the uncertainties arising from numerical damping, but it increases the computational cost significantly.

# Chapter 4

# Mesh-based FSI analysis

This chapter commences by presenting the structural and fluid model validation. This was done prior to the FSI simulation to ensure that each model is set up correctly. The FSI results are then presented with a discussion on whether mesh-based methods are a viable option for simulating the aerodynamic damping of the ACC fan.

## 4.1 Structural model verification

The structural model was validated using the data given in section 2.2. Three different structural meshes are compared to ensure mesh independence. The meshing procedure and set-up of the transient and modal analysis are discussed in appendix C. Table 4.1 compares the numerical results of the three different meshes with the experimental measurements.

**Table 4.1:** Structural model verification

| | Experimental | Coarse | Medium | Fine |
|---|---|---|---|---|
| No. of cells | | 4158 | 4689 | 6151 |
| $f_V$ $[Hz]$ | 11.3255 | 11.345 | 11.352 | 11.35 |
| $\zeta_V$ $[10^{-3}]$ | 1.3333 | 1.352 | 1.353 | 1.328 |

The medium and fine meshes have 12.77 % and 47.93 % more cells than the coarse mesh respectively, but predict values for $f_V$ and $\zeta_V$ that are almost identical as shown in table 4.1. The solution is therefore mesh independent. As done by Brandsen (2013), the Young's modulus of the blade model was adapted so that its natural frequency corresponds to that of the physical blade. This lead to deviations from the experimental values of less than 0.25 % and 1.5 % for $f_V$ and $\zeta_V$ respectively.

The computational cost of the FEM model is negligible compared to that of the CFD simulation (Brandsen, 2013). The choice of the structural grid is therefore only dependent on the model's accuracy. As seen from table 4.1, the predictions of each model are identical and so the coarse mesh will be used in the FSI simulation.

Figure 4.1 displays the first three modelled structural modes. In figure 4.1a, the blade only deflects along its longitudinal axis with no torsional deformation. A single vibrational node is observed at the blade's base. This defines the first bending mode. The second bending mode is depicted in figure 4.1b. Again, no torsional deformation is observed, but two vibrational

nodes occur. The third mode differs from the first two as shown in figure 4.1c. The blade twists around its longitudinal axis , indicating the first torsional mode. This corresponds to the findings of Basson (2015).

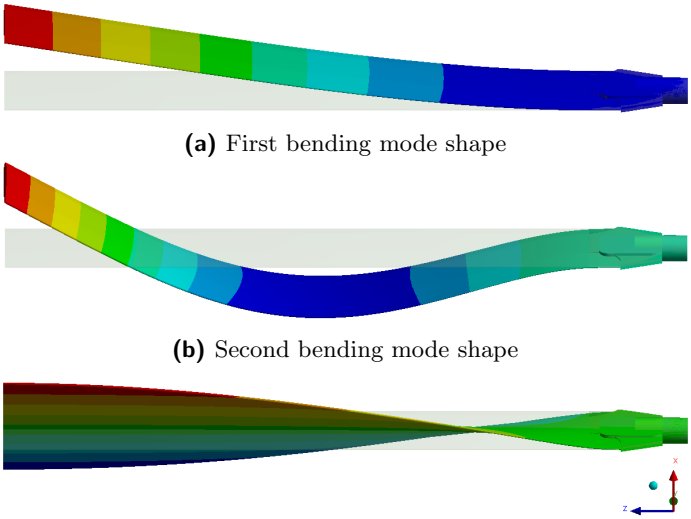

**(a)** First bending mode shape

**(b)** Second bending mode shape

**(c)** First torsional mode shape

**Figure 4.1:** First three mode shapes

In table 4.2 the experimentally and numerically determined modal frequencies are compared. Important to note is that Basson (2015) determined these modes in air, whereas the FEM blade model is simulated in vacuum. As mentioned in section 2.5, the added mass effect of air is not negligible and leads to deviations in the blade's natural frequencies when measured in air. The modal frequencies are still within 5 % of each other as shown in table 4.2.

**Table 4.2:** Experimental and numerical modal frequencies

| | Experimental | Coarse |
|---|---|---|
| 1st Bending mode $[Hz]$ | 10.993 | 11.345 |
| 2nd Bending mode $[Hz]$ | 68.161 | 70.428 |
| 1st Torsional mode $[Hz]$ | 116.869 | 118.43 |

## 4.2 Fluid model verification

The fluid model will be validated using a steady state simulation. The first subsection covers the viscous model selection for the FSI simulation. The obtained results are then compared to the experimental data from Riegels (1961) for a flat plate.

### 4.2.1 Turbulence or transition model

The maximum Reynolds number falls within the transition region, as specified in section 2.3, which suggests the use of a transition model. However, free stream turbulence and the rapid motion of the blade further induce flow disturbances that can lead to flow transition or fully turbulent flow. The use of turbulence models can limit the prediction of dynamic and static flow effects (Shengyi *et al.*, 2010). These can only be accurately captured using a transition model and can affect the prediction of $C_L$ significantly (Shyy *et al.*, 2013).

**Computational considerations:** The use of a transition model implies a higher computational cost compared to using a turbulence model for the following two reasons:

- No wall functions are employed when using transition models. The model requires that the boundary layer is fully resolved and thus limits $y^+$ to be below 1 (ANSYS Inc., 2013*b*). The mesh density is therefore higher in the blade's proximity. This increases the computational cost compared to turbulence models using enhanced wall treatment. The use of enhanced wall treatment is discussed in appendix D.3.

- The fluid mesh is updated at every time instance to accompany the displaced blade. This can cause computational problems such as the formation of negative cell volumes. Re-meshing and smoothing operations, discussed in appendix D.5.1, are used to prevent mesh deterioration. These operations are more costly for finer meshes and fail once the blade's motion per time step is too large compared to the cell volume.

Two different geometric AOAs are investigated with each one being tested at three different flow velocities. Furthermore, the frequency ratio $r$ has to be varied to ensure that the peak tip displacement is recorded. This means that for a minimum of three different frequency ratios, a total of 18 FSI simulations are required. Thus, the computationally less expensive turbulence model will be used to determine the peak frequency ratios. The transition model will then be used to analyse and visualise the flow for these. This reduces the total computational time significantly.

**Accuracy considerations:** Figure 2.9 shows the normal force $F_N$ that dampens the flapwise blade motion. $F_N$ is given by:

$$F_N = cos(\alpha_G)F_L + sin(\alpha_G)F_D \tag{4.1}$$

The equation shows that the transverse motion of the blade is mainly influenced by the lift force for small AOAs ranging from 0 ° to 9 °. Additionally, figure 2.3 shows that $C_L$ is significantly larger than $C_D$. The lift force is given by Cengel and Cimbala (2010) in equation (4.2):

$$F_L = -\int_A (p\,sin\,\theta + \tau_W\,cos\,\theta)\,dA \tag{4.2}$$

where $\theta$ is the angle between the normal of the differential surface area $dA$ and the positive flow direction. According to Cengel and Cimbala (2010), the lift contribution of the viscous forces, modelled using the wall shear stress $\tau_W$, is negligible compared to that of the fluid pressure $p$ for streamlined objects. This significantly simplifies the lift prediction as the pressure distribution can be approximated by potential flow theory. In this case, the turbulence and transition model will accurately predict the lift force.

Inaccuracies and deviations between the turbulence and transition model are introduced due to flow separation and the occurrence of transitional effects. Pierce (2008) found that transitional effects, such as the laminar separation bubble, are not captured by turbulence models. Furthermore, a variation in the predicted separation and reattachment point can lead to major discrepancies between the calculated lift force of different viscous models.

To conclude, the use of a turbulence model is appropriate if no transitional effects are present and if it can accurately predict the onset of flow separation. The choice of the correct viscous model can therefore greatly influence the simulation's accuracy. In addition, the accuracy of the chosen turbulence model is verified using a transition model at the peak frequency ratios.

#### 4.2.1.1 Transition and turbulence models

According to the findings of Pierce (2008), the SST $k-\omega$ model underpredicts the lift coefficient of the investigated wind turbine blade. This turbulent model will however be used for the following reasons:

- It is a superior alternative to the $k-\epsilon$ model, which has difficulties with predicting boundary layer separations and is not recommended for external flows (ANSYS Inc., 2013*b*).
- The SST $k-\omega$ model is better than other turbulence models at predicting flow separation from smooth surfaces and predicting boundary layer separation under adverse pressure gradients (Shengyi *et al.*, 2010).

The transition SST model is used for the transition FSI simulations, as it is capable of predicting flow transition in the boundary layer and is recommended by ANSYS Inc. (2013*b*).

### 4.2.2 Validation and mesh independence

Figure 4.2 compares the lift and drag coefficients of the flat plate from Riegels (1961) with those determined by the two viscous models. The fluid model set-up and the mesh independence study are discussed in Appendix D.

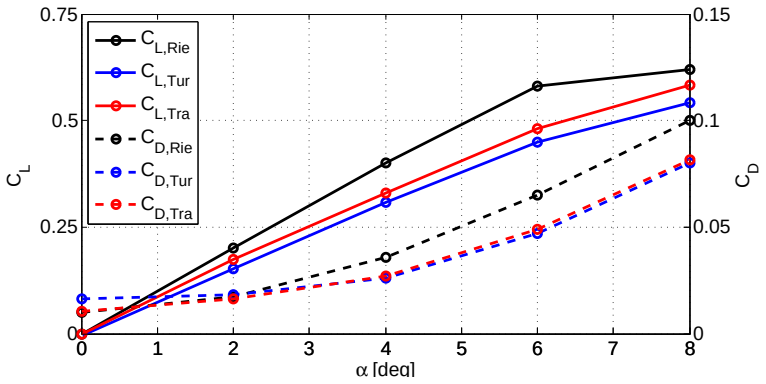


**Figure 4.2:** $C_L$ and $C_D$ findings from Riegels (Rie) compared to those predicted by the SST $k-\omega$ turbulence (Tur) model and the SST transition (Tra) model

The viscous models underpredict the experimentally determined lift coefficient. The flat plate used in Riegels (1961) spans over the entire width of the wind tunnel. This means that both ends of the blade are enclosed so that the flow over the blade can be assumed to be two-dimensional. The flow over the fan blade cannot be assumed to be two-dimensional, as three-dimensional flow effects occur at the blade tip. The lift force is reduced due to downwash at the blade tip (Shyy *et al.*, 2013).

At the blade's tip the air is free to move from the high pressure side to the low pressure region on the blade's suction side. This reduces the pressure difference across the blade's tip and thus the lift force is reduced. Downwash is depicted in figure 4.3 by indicating the pressure reduction and increase on the blade's pressure and suction sides respectively.

The transition model predicts a higher lift coefficient than the turbulence model. As explained in subsection 4.2.1 this can be due to both models predicting different flow separation points on the blade. The findings from Pierce (2008) indicated that the SST $k-\omega$ model underpredicts the lift force.

The SST $k-\omega$ model assumes turbulent flow over the entire blade, which results in a larger $C_D$ than experimentally determined for low AOAs. The SST transition model on the other hand predicts the drag coefficient accurately at low AOAs.

Downwash modifies the pressure distribution near the tip of the blade and thus produces an additional drag force named induced drag (Shyy *et al.*, 2013):

$$C_{ID} = \frac{C_L^2}{\pi e AR} \tag{4.3}$$

where the induced drag coefficient $C_{ID}$ depends on the lift coefficient, span efficiency factor $e$ and the aspect ratio (AR) of the wing. This means that the numerically determined drag force should be higher than the experimental drag due to the additional three-dimensional effects. This is not the case, as shown in figure 4.2, due to numerical inaccuracies.

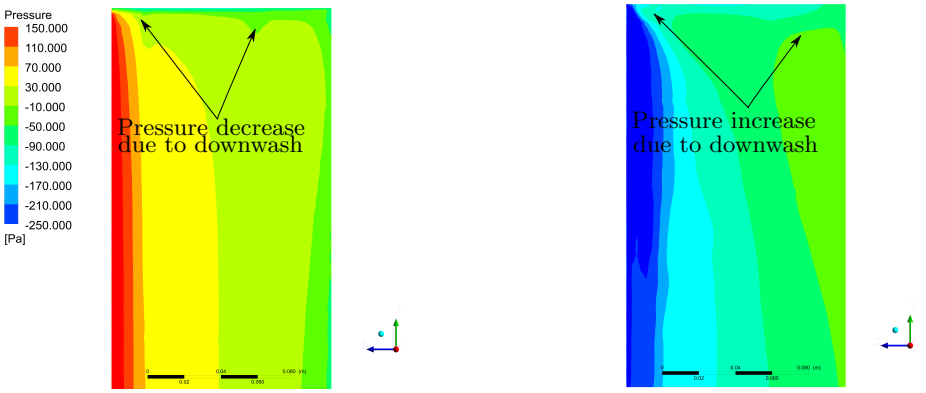


**(a)** Pressure distribution on blade's pressure side

**(b)** Pressure distribution on blade's suction side

**Figure 4.3:** Pressure changes at blade tip due to downwash

## 4.3 FSI results

The structural and fluid model adjustments for the FSI simulation are stated in appendix C.3 and appendix D.5 respectively. Additional information regarding the FSI set-up procedure and sensitivity analysis can be found in appendix E.

The SST $k-\omega$ turbulence model was used in combination with the linear FEM solver to determine the blade's peak tip displacement for the different flow velocities and geometrical AOAs as shown in figure 4.4. The turbulence model was then replaced by the SST transition model to ensure that flow transition is captured accurately at the peak frequency ratio. The experimental results from Basson (2015) are displayed in the figure for reference purposes.

Table 4.3 states the relative deviation (RD) of the FSI simulations in predicting the maximum tip displacements relative to the experimental findings. The transition model estimates a lower peak tip displacement at 0AOA than the turbulence model. The opposite occurs at 9AOA where the transition model predicts a higher peak tip displacement. The deviation between the two models can be related to the fact that transitional effects are not captured by the turbulence model. The difference between the two viscous models relative to the experimental peak tip displacement is less than 12 % for all but one simulation. A good correlation between the numerical results is to be expected as Pierce (2008) had similar findings.

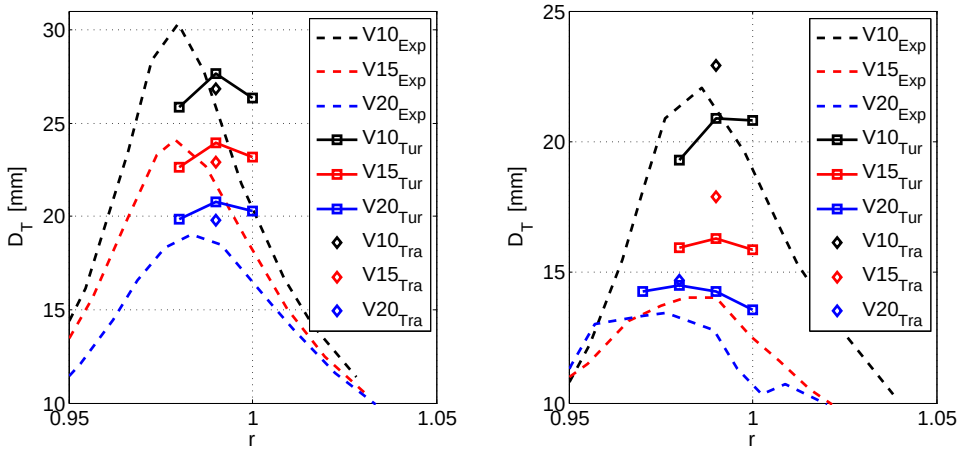


**(a)** 0AOA **(b)** 9AOA

**Figure 4.4:** Mesh-based FSI model validation for the two different geometric AOAs

Both models deviate significantly from the experimental findings at 9AOAV15, which is the simulation performed at 9AOA with an inlet velocity of approximately 15 m/s. Large deviations are also observed when using the meshless FSI simulation for this scenario. No evidence was found in the flow analysis to support the low tip displacement at 9AOAV15. Experimental inaccuracies could be the reason for the large discrepancies between the numerical and experimental results. Possible causes for experimental error are discussed in section 4.3.1.

**Table 4.3:** Relative deviation (RD) of the FSI simulations in predicting the maximum tip displacement. The deviation is relative to the experimental results

| $AOA$ | $V$ | $RD_{Tur}$ [%] | $RD_{Tra}$ [%] |
|---|---|---|---|
| 0 | 10 | -8.91 | -11.52 |
| | 15 | -0.68 | - 4.95 |
| | 20 | 9.15 | 4.13 |
| 9 | 10 | -5.36 | 3.96 |
| | 15 | 15.94 | 27.31 |
| | 20 | 7.68 | 9.31 |

Except for the 9AOAV15 simulation, the mesh based FSI simulation, using either viscous model, predicts the peak tip displacement within 12 %, when compared to the experimental results.

The peak frequency ratio $r_P$ is affected by variations of the inlet velocity and the geometric AOA as stated in section 2.5. The $r_P$ values of the FSI simulation and the experiment are compared in table 4.4. The relative deviation

for all simulations is below 2 %, which means that the FSI simulation captures the frequency shift due to the surrounding fluid very accurately. As shown by Weber and Seidel (2015), mesh-based FSI simulations also accurately predict the structure's natural frequency if it is submerged in high density liquids such as water.

**Table 4.4:** FSI peak frequency ratio verification

| $AOA$ | $V$ | $r_{P,Exp}$ | $r_{P,Tur}$ | RD [%] |
|---|---|---|---|---|
| 0 | 10 | 0.980 | 0.99 | 1.05 |
| | 15 | 0.979 | 0.99 | 1.12 |
| | 20 | 0.983 | 0.99 | 0.71 |
| 9 | 10 | 0.986 | 0.99 | 0.41 |
| | 15 | 0.981 | 0.99 | 0.92 |
| | 20 | 0.977 | 0.98 | 0.31 |

### 4.3.1 Possible causes of experimental error at 9AOAV15

Discrepancy between the numerical and experimental results for the 9AOAV15 simulation led to speculations that experimental errors could be the cause. The following statement is an assumption that should be verified before simulating the ACC fan unit.

Basson (2015) observed a problem with the blade's fastening method to the base excitation mechanism. During his first experiments, the thread loosened, which led to the weakening of the connection. This led to excessive structural damping. The problem was solved by improving the fastening method, but extensive testing could have initiated a similar issue. Other issues could have arisen from incorrect settings of the inlet velocity, geometric AOA or the base excitation frequency, but are unlikely as Basson (2015) mentions that 50 measurements were taken when determining the transmissibility curves.

### 4.3.2 Suitability of mesh-based methods for simulating the aerodynamic damping of the ACC fan

The experimental peak frequency ratios and tip displacements are accurately predicted with a relative error of less than 12 % for 5 out of 6 simulations. Experimental inaccuracies are a plausible cause for the considerable deviation of the results for the 9AOAV15 simulation.

The SST transition model in combination with a fine mesh around the blade ensures that the boundary layer and vortices are accurately resolved. Furthermore, mesh based methods use well developed algorithms to solve the governing equations of fluid and structure dynamics (Liu and Liu, 2003). For these reasons, the mesh-based method should be capable of accurately modelling the rotating and oscillating fan in the ACC unit.

Numerical instabilities were observed, because the mesh around the blade was too fine for the chosen time step. This problem can be solved by reducing the time step size or by employing re-meshing and cell smoothing processes more frequently. These prevent cell deterioration, but add to the computational cost and cause numerical diffusion. Additionally, mesh motion is more severe when explicitly modelling the fan in the ACC unit. The fan blades do not only vibrate at their first bending frequency, but are also translationally displaced as they rotate. Cell deterioration would therefore be a serious concern. However, cell deterioration can be minimized by encompassing the fan in a moving subdomain. For example, a full scale offshore wind turbine was modelled by encompassing the rotor blades with a moving subdomain in which the fluid mesh was adjusted to the deforming blade (Hsu and Bazilevs, 2012). The subdomain rotates at the same rotational speed as the wind turbine to ensure minimum mesh deformation. The mesh within the subdomain is coupled to the rest of the stationary fluid domain using sliding interface conditions. This offers a viable solution for modelling the fan within the ACC unit using mesh-based methods.

The runtime for one simulation, using the SST transition model, is 28 hours when running 8 parallel processes on an Intel core i7-4790 processor (3.6 GHz). Considering that roughly 1.2 million cells are used to model a single oscillating fan blade, the computational cost will significantly increase when modelling the ACC fan unit.

To conclude, mesh-based methods can be used to simulate the fluid structure interaction occurring within the ACC unit. One major limitation is mesh motion that can cause inaccuracies and instabilities.

## 4.4 Flow analysis

The FSI simulations, using the SST transition model, are used to analyse the occurring flow phenomena. A heuristic fluid model is created, in the following chapter, based on the observations made.

This section focuses specifically on leading edge vortices, tip vortices and downwash as they are the major flow phenomena that affect the blade's aerodynamic loading. Two other flow phenomena, namely wake capture and laminar separation bubbles, were investigated but they do not occur. Arguments to why they are absent are given in appendix E.2.

The aerodynamic forces and moments are time dependent due to blade motion. As shown in figure 4.5, the lift force requires time to fully develop to its steady state value and does not change instantaneously to the new quasi steady value. The circulation around the blade has to fully develop to adjust to the new effective AOA and therefore causes the observed delay in lift variation (Wright and Cooper, 2015). This affects the pressure distribution around the blade and has to be considered in the flow analysis.

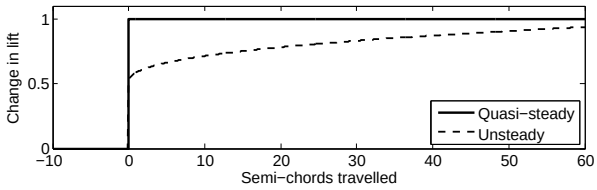


**Figure 4.5:** Change in the lift force due to sudden change in angle of attack (Wright and Cooper, 2015)

### 4.4.1 Leading edge vortices (LEVs)

The terminology used to explain the occurrence of leading edge vortices is depicted in figure 4.6. The leading edge vortex is indicated in the figure. WFS and AFS describe the direction of blade motion with and against the free stream respectively.

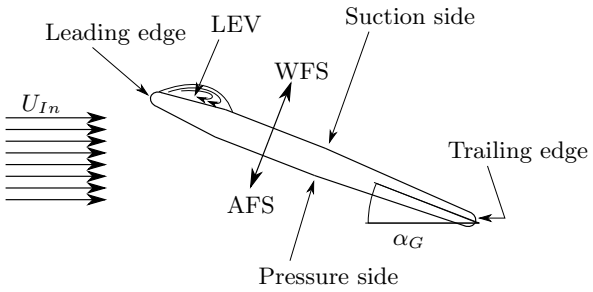


**Figure 4.6:** Leading edge vortex and terminology used to explain vortex dynamics

A theoretical background on leading edge vortices is presented to explain the phenomena by summarising previous findings from literature. This is followed by a thorough investigation of the FSI simulations at 0AOA and 9AOA.

**Theoretical background:** As mentioned, the flow around the blade does not change instantaneously as the blade is accelerated, but requires time to develop fully. The developed lift is only a fraction of its steady state value if the blade is accelerated at an AOA lower than its stall angle (Shyy *et al.*, 2013).

This is not the case if the flow separates from the blade's leading edge to form a vortex that amplifies the lift force (de Croon *et al.*, 2015). According to Chang (2014), flow separates from the leading edge if:

- The blade is set in motion at an angle of attack greater than its stall angle.

- The flow abruptly separates from the leading edge. The onset of flow separation depends on a variety of factors, such as the Reynolds number and blade geometry (Cengel and Cimbala, 2010). According to Mashud *et al.* (2009), sharp leading edges can cause premature flow separation at angles of attack lower than the stall angle. The sharp edge causes a large adverse pressure gradient that forces the flow to separate.

After the flow has separated from the leading edge, an increasing angle of attack ensures the growth of the separated flow region and its development into a vortex (Widmann, 2015). The vortex is bound to the blade creating a low pressure region on its suction side and thus amplifies the lift force. This is depicted in figure 4.6. Shyy *et al.* (2013) mentions experimental results where the LEV stays attached to the blade for several chords of travel and increases the lift by up to 80 % compared to its steady state value.

Tip effects induce spanwise flow across the blade that ensures vorticity transport towards the blade tip. This can lead to the interaction of the LEV and the tip vortex (Shyy *et al.*, 2013). It is further mentioned that a spanwise flow stabilises the LEV and delays stall during the translational motion of a wing.

A LEV is an unsteady phenomenon that is initialised on the blade's suction side and grows until it is convected downstream and shed into the wake. The lift force is drastically reduced as the LEV is shed from the blade. This is termed dynamic stall (Shengyi *et al.*, 2010). The entire stall process depends on several factors such as oscillation amplitude, reduced frequency and the Reynolds number (Shengyi *et al.*, 2010). According to Green (1995), the vortex is stable if the tangential flow velocity is high and the vortex core radius is small. Vortex breakdown occurs if the vortical motion experiences a rapid transition to highly turbulent flow with a low tangential velocity and a large vortex core radius.

**Dependency of the LEV on the effective AOA:** A leading edge vortex can only occur if the flow separates from the blade's leading edge to form an enclosed circulation region (Shyy *et al.*, 2013). Abrupt flow separation is observed at the blade's leading edge, when the effective AOA exceeds the blade's separation threshold (ST):

$$\alpha_E(z,t) > \alpha_{ST} \quad \text{where} \quad \alpha_E(z,t) = \alpha_G + \tan^{-1}\left(\frac{U_{Bl}(z,t)}{U_{In}\cos\alpha_G}\right) \tag{4.4}$$

Figure 4.7 shows the spanwise variation of the effective AOA along the blade. Four time instances are depicted for each geometric AOA to show when flow separation will occur. The separation threshold is depicted in the figure and was found to be less than 9 degrees for the given blade geometry and flow conditions. Inlet velocities V10 and V20 are depicted using the red and blue lines respectively.

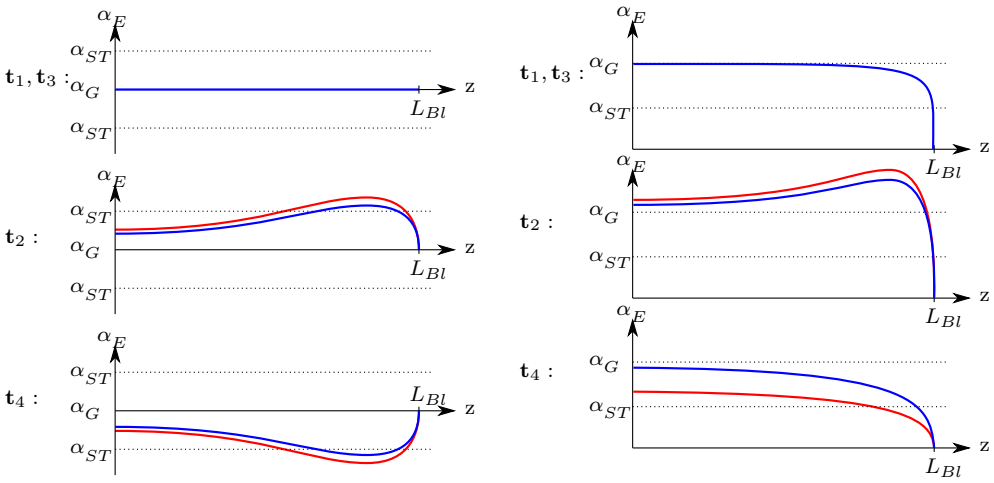


**(a)** 0AOA **(b)** 9AOA

**Figure 4.7:** Effective AOA as a function of the spanwise location and time instance. V10 and V20 are indicated by the red and blue lines respectively

Time instances $t_1$ to $t_4$ occur when either the blade's tip displacement is maximum or minimum as depicted in figure 2.10. At instances $t_1$ and $t_3$, the effective AOA is approximately equal to the geometric AOA, because the blade's velocity is at a minimum. Therefore, no flow separation occurs at 0AOA. However at 9AOA, the effective angle of attack is larger than the separation threshold and flow separates over the blade's entire leading edge, except close to its tip, where downwash reduces the effective AOA below the separation threshold.

At 0AOA, the blade reaches its maximum velocity at $t_2$. The effective angle of attack is raised above the separation threshold near the blade tip. This also applies to instance $t_4$, but the blade moves in the opposite direction. Equation (4.4) shows that the effective AOA is inversely related to the inlet velocity. Therefore, the effective AOA exceeds the ST over a larger spanwise portion of the blade at lower inlet velocity. This causes a larger separation region at V10 than at V20.

At 9AOA, the blade reaches its maximum effective AOA when the blade moves at maximum velocity against the free stream. This occurs at instance $t_2$. The separation threshold is exceeded significantly, which causes very strong vortex formations as stated by Widmann (2015). At $t_4$, the blade moves at maximum velocity with the free stream, which causes the effective AOA to reduce across the entire blade. The blade's flapwise velocity is greater at lower inlet velocities, because of the reduced aerodynamic loading. This causes a greater reduction in the effective AOA when the blade is moving WFS at lower inlet velocities.

**0AOA:** As depicted in figure 4.7a, the effective AOA only exceeds the separation threshold close to the blade tip at instances $t_2$ and $t_4$. If this occurs, the flow separates from the blade's leading edge as shown in figure 4.8 for the minimum (V10) and maximum (V20) inlet velocities. The separated flow region (SFR), indicated using a white ISO surface, reduces in size as the inlet velocity is increased.

The presence of a leading edge vortex within the separated flow region is verified in figure 4.9. Pressure reduction occurs near the blade's leading edge due to the circulating flow. This is the largest occurring LEV observed at 0AOA. It occurs at an inlet velocity of 10 m/s and at the spanwise location where the size of the SFR is maximum. Altering the spanwise location, inlet velocity or the time instance in the oscillation cycle reduces the size of the LEV.

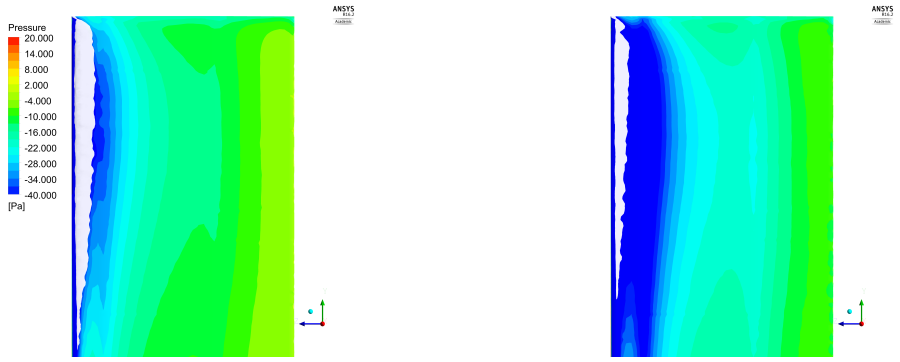


**(a)** Minimum inlet velocity **(b)** Maximum inlet velocity

**Figure 4.8:** Comparison of the separated fluid region for different inlet velocities

The vortex spans over a relatively small portion of the blade. For that reason, the induced pressure reduction due to the leading edge vortex has a negligible effect on the blade's aerodynamic loading. This is proven in section 5.3.1.

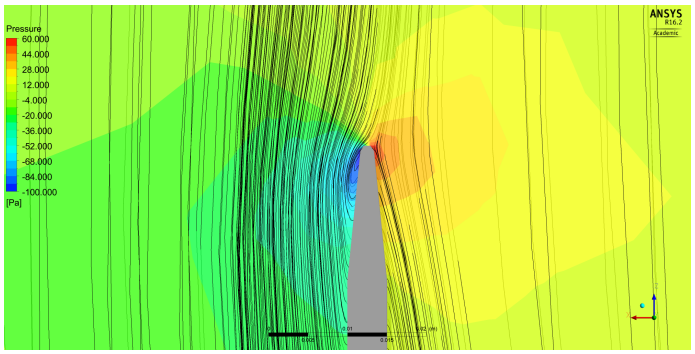


**Figure 4.9:** Streamlines and pressure contour showing the presence of a LEV in the separated fluid region

**9AOA:** Figure 4.10 and figure 4.11 visualise the development of the SFR over an entire oscillation cycle for the minimum (V10) and maximum (V20) inlet velocity respectively.

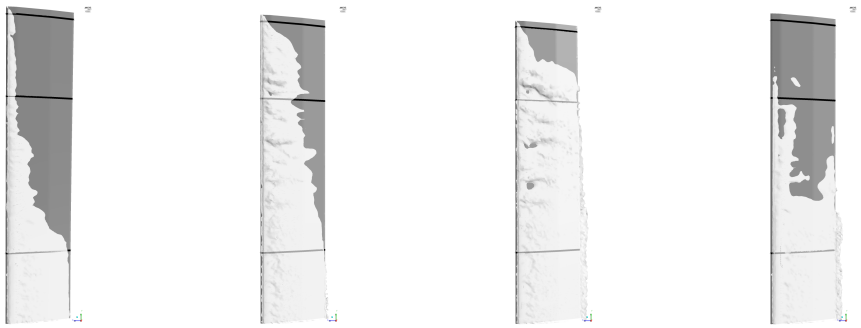

**(a)** Maximum $D_T$ at $t_1$ **(b)** Minimum $D_T$ at $t_2$, AFS **(c)** Maximum $D_T$ at $t_3$ **(d)** Minimum $D_T$ at $t_4$, WFS

**Figure 4.10:** The development of the separated flow region for V10

The effective AOA is equivalent for both inlet velocities at $t_1$ and $t_3$. It is sufficiently large so that the flow can separate across the entire blade's leading edge. Only at the blade tip it reduces below the separation threshold.

The circulating flow is convected downstream due to the free stream velocity. At higher inlet velocities the convection rate is higher and therefore the width of the SFR increases more significantly. The width of the SFR increases up to the point where the effective AOA falls below the separation threshold.

Figure 4.7b shows that at $t_4$, the effective AOA falls below the ST for the blade's upper quarter at V10. This results in no flow separation at the leading edge as depicted in figure 4.10d. The previously formed vortices have been shed into the wake and therefore a new separated flow region has to form again near the blade tip at $t_1$. This is not observed for V20, because the effective AOA still exceeds the separation threshold along the blade's entire leading edge.

According to figure 4.7b, the effective AOA does not vary significantly near the blade root and is always above the ST. Consequently, the width of the SFR is almost constant throughout the entire oscillation cycle. This means that the vorticity introduced at the leading edge is roughly equivalent to the amount being shed into the wake during blade oscillation. This does not hold true closer to the blade tip. The effective AOA fluctuates more and thus the size of the SFR varies noticeably. This especially holds true at lower inlet velocities, because of the greater oscillation amplitude. This also suggests a greater vortex strength variation towards the blade tip.

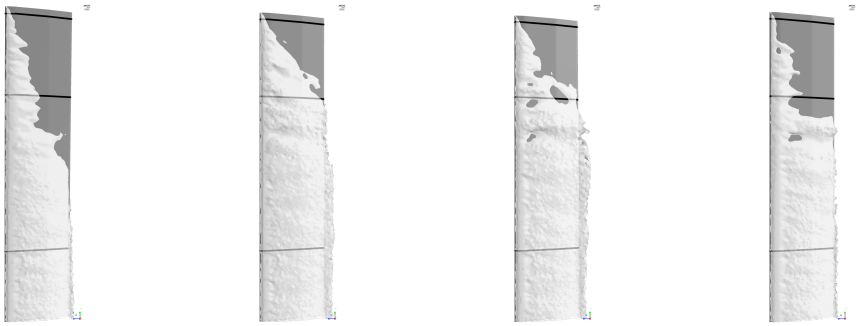

**(a)** Maximum $D_T$ at $t_1$ **(b)** Minimum $D_T$ at $t_2$, AFS **(c)** Maximum $D_T$ at $t_3$ **(d)** Minimum $D_T$ at $t_4$, WFS

**Figure 4.11:** The development of the separated flow region for V20

The black lines indicated in figure 4.10 and figure 4.11 show the location at which the flow within the SFR will be analysed. In the following chapter, the blade is split into 20 equally sized strips to locally extract the blade forces. Each strip is called an ISO clip with ISO 1 located at the blade root and ISO 20 covering the blade tip. The black lines correspond to the mid locations of ISO 5, 15 and 20. In figure 4.12 to figure 4.14 streamlines are used to easily identify vortex structures. Their influence on the local pressure distribution is visualised using pressure contours.

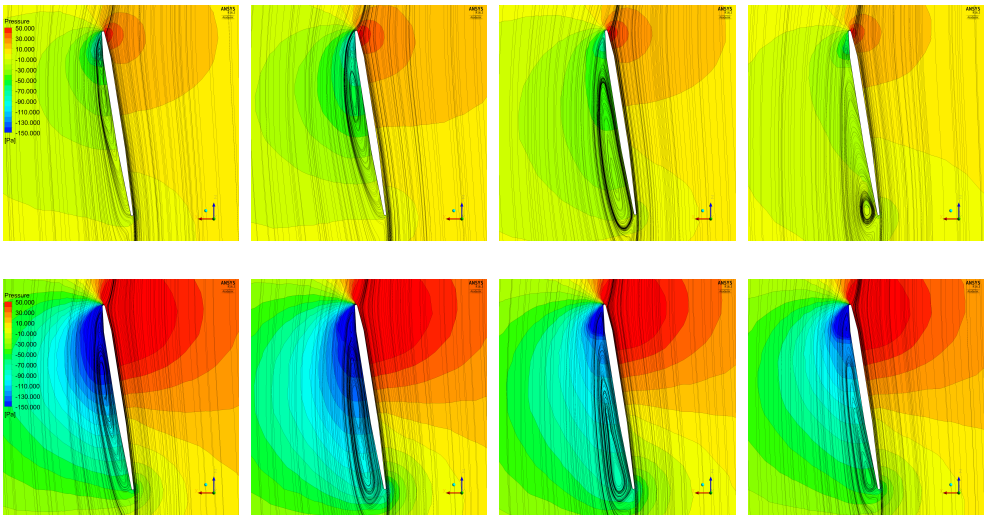

**(a)** Maximum $D_T$ at $t_1$ **(b)** Minimum $D_T$ at $t_2$, AFS **(c)** Maximum $D_T$ at $t_3$ **(d)** Minimum $D_T$ at $t_4$, WFS

**Figure 4.12:** Flow development at ISO 5 for V10 (top) and V20 (bottom)

**ISO 5:** At this spanwise location, the effective AOA always exceeds the separation threshold. Figure 4.12 proves that a leading edge vortex is formed at every time instance. At $t_2$ and $t_4$, the leading edge vortex is at its strongest and weakest respectively. This is indicated by the low pressure region near the leading edge, which is considerably larger at $t_2$ than at $t_4$. Therefore, a positive correlation between the effective AOA and vortex strength exists.

The free stream transports circulating flow downstream, which leads to the formation of a secondary vortex on the blade's suction side. At higher inlet velocities, the secondary vortex is larger and convected downstream more rapidly. It reduces the pressure in its vicinity and so increases the blade's aerodynamic loading. This holds true until the secondary vortex core is located near the blade's trailing edge. The pressure difference across the blade reduces as the vortex lowers the pressure on both sides. Most of the secondary vortex is shed into the wake at $t_4$ and reforms near the leading edge at $t_1$.

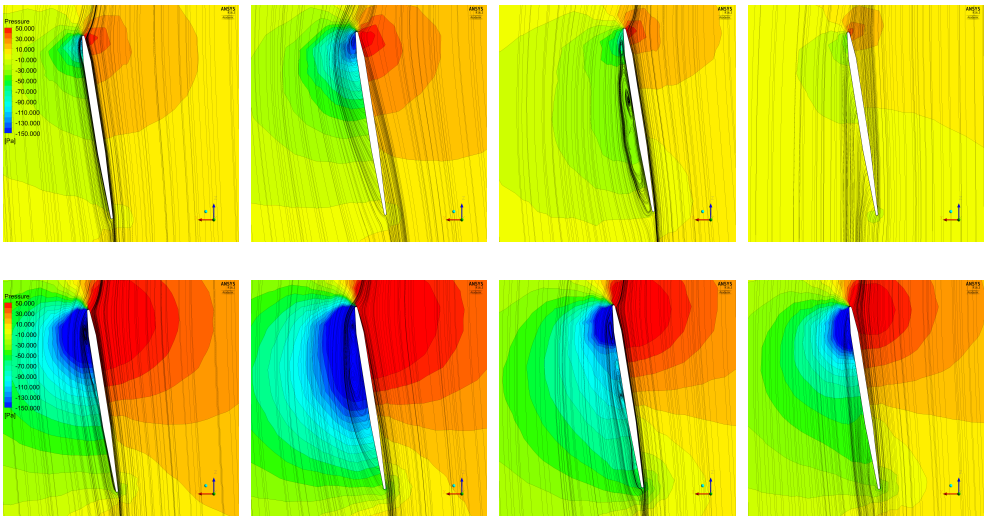

**(a)** Maximum $D_T$ at $t_1$ **(b)** Minimum $D_T$ at $t_2$, AFS **(c)** Maximum $D_T$ at $t_3$ **(d)** Minimum $D_T$ at $t_4$, WFS

**Figure 4.13:** Flow development at ISO 15 for V10 (top) and V20 (bottom)

**ISO 15:** The range of the effective AOA is considerably larger at ISO 15 than at ISO 5. This leads to a more significant vortex initialisation, growth, decay and shedding.

For both inlet velocities, a strong vortex is initialised at $t_1$. No secondary vortex is visible and thus the flow reattaches to the blade directly after the LEV. The LEV grows and spreads downstream at $t_2$, lowering the pressure over a wider region of the blade. At $t_3$, a LEV is still formed near the leading edge, but the majority of the recirculating flow is convected downstream forming a secondary vortex. Both vortices are shed as the minimum effective

AOA is significantly lower than the separation threshold at $t_4$. The pressure increases on the blade's suction side once the vortices are completely shed. This is termed dynamic stall.

**ISO 20:** This ISO clip is located relatively close to the blade tip. The observed flow is therefore influenced by downwash. A small LEV forms at $t_1$ for both inlet velocities that then grows at $t_2$, decays at $t_3$ and is completely shed at $t_4$. The SFR is limited to a small region near the leading edge. The flow immediately reattaches after the leading edge and stays attached along both sides of the blade. Vortices are convected rapidly away from the blade surface due to downwash and the large blade velocity. The formation of a secondary vortex is therefore not observed.

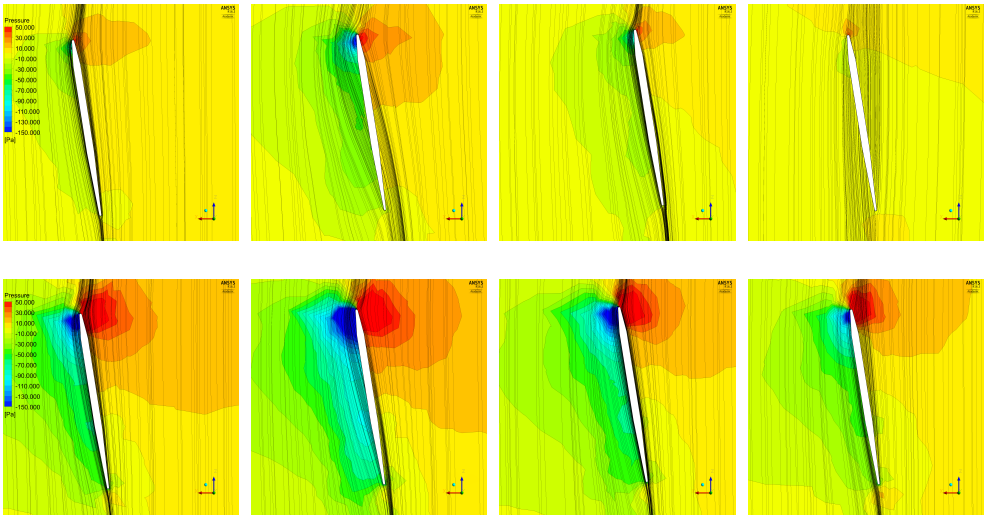

**(a)** Maximum $D_T$ at $t_1$ **(b)** Minimum $D_T$ at $t_2$, AFS **(c)** Maximum $D_T$ at $t_3$ **(d)** Minimum $D_T$ at $t_4$, WFS

**Figure 4.14:** Flow development at ISO 20 for V10 (top) and V20 (bottom)

### 4.4.2 Tip vortices and downwash:

A theoretical background on tip vortices and downwash is presented to explain the phenomena by summarising previous findings from literature. This is followed by a thorough investigation of the FSI simulations at 0AOA and 9AOA.

**Theoretical background:** For a finite wing, the fluid can freely flow from the high to the low pressure regions at the blade tip. This introduces a spanwise velocity component that decreases the pressure difference across the blade

and the effective AOA. The phenomenon is known as downwash and reduces the lift force of the blade (Shyy *et al.*, 2013).

Vortices are introduced due to the circulatory flow around the blade tip. According to Shyy *et al.* (2013), the vortex is associated with a low pressure region due to its increased circulatory velocity. For that reason, the tip vortex introduces a low pressure region on the blade's suction side that increases the lift force. The vortex dissipates further downstream, because the low pressure attracts fluid towards the vortex core and increases the pressure until ambient pressure is reached. Downwash and tip vortices were also observed in the CFD validation as discussed in section 4.2.2.

**0AOA:** Figure 4.15 compares the downwash effect using the spanwise velocity distribution for four different occasions. Downwash depends on the inlet velocity, the blade's translational velocity and the distance from the blade tip. In each scenario one variable is altered while the others remain constant.

Figure 4.15a is used as reference where the observed plane is situated 20 mm from the blade tip. The inlet velocity is 10.931 m/s and the blade is moving upwards at maximum velocity. Due to the blade's motion, the air is forced over the blade tip onto the blade's lower side. The circulating flow is convected downstream due to the free stream. This creates a helical flow structure termed tip vortex.

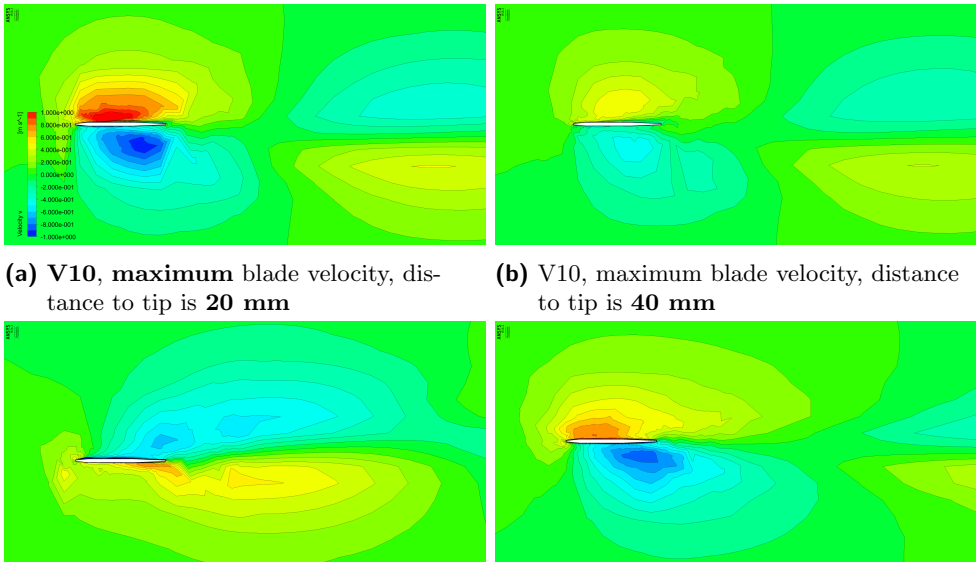

**(a)** **V10**, **maximum** blade velocity, distance to tip is **20 mm**

**(b)** V10, maximum blade velocity, distance to tip is **40 mm**

**(c)** V10, **minimum** blade velocity, distance to tip is 20 mm

**(d)** **V20**, maximum blade velocity, distance to tip is 20 mm

**Figure 4.15:** Comparison of the spanwise velocity distribution for varying conditions at 0AOA

The second figure depicts the vertical flow field 40 mm away from the tip. The magnitude of the vertical velocity reduces considerably. The loss of lift due to downwash therefore reduces as the distance to the tip increases. Figure 4.15c shows that a reduction in the blade's flapwise velocity reduces the vertical velocity around the blade. Tip vortices are therefore less dominant and downwash is reduced.

In the last figure the inlet velocity is increased to 20.335 m/s. Two counteracting effects alter the swirling strength of the tip vortex. It is reduced due to the blade's lower flapwise velocity, but increases due to the higher pressure difference across the blade. The blade's flapwise velocity reduces due to the higher aerodynamic loading, but an increased inlet velocity results in a greater pressure difference across the blade, which increases the downwash effect. The vertical velocity magnitude is lower than for a lower inlet velocity, which means that the reduction in the blade's flapwise velocity dominates the downwash effect. Furthermore, an increase of the inlet velocity results in a faster convection of the tip vortices downstream.

The vertical velocity is relatively small compared to the inlet velocity. For that reason, the effects of tip vortices on the blade's aerodynamic loading can be neglected in the heuristic fluid model.

**9AOA:** The same analysis procedure is used as for 0AOA and the spanwise velocity distribution is displayed in figure 4.16 for the four different scenarios.

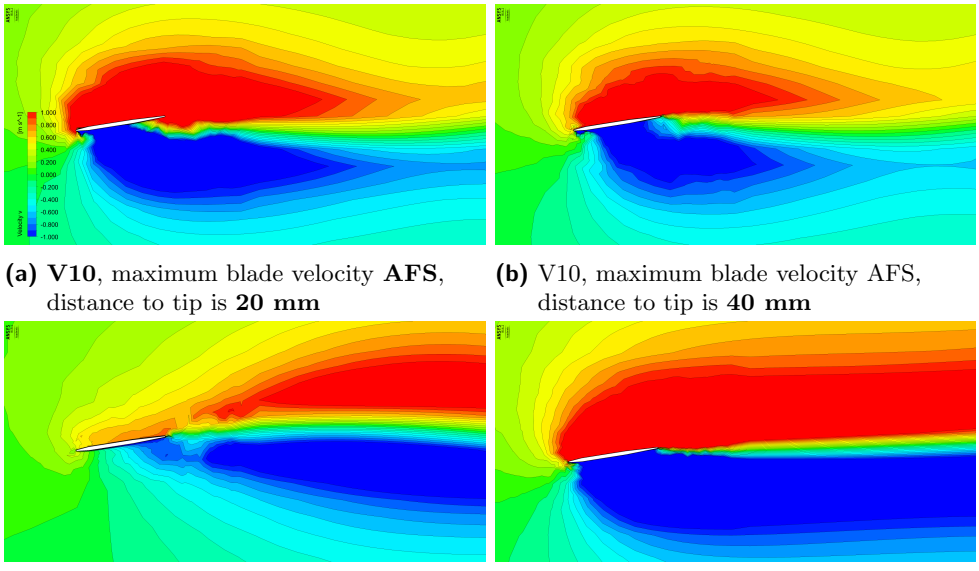

**(a)** **V10**, maximum blade velocity **AFS**, distance to tip is **20 mm**

**(b)** V10, maximum blade velocity AFS, distance to tip is **40 mm**

**(c)** V10, maximum blade velocity **WFS**, distance to tip is 20 mm

**(d)** **V20**, maximum blade velocity AFS, distance to tip is 20 mm

**Figure 4.16:** Comparison of the spanwise velocity distribution for varying conditions at 9AOA

An increase in the geometric AOA leads to larger tip vortices as shown by the increased spanwise velocity fields around the blade. The pressure difference across the blade is larger at increased geometric AOAs, which leads to an amplified downwash effect as shown in figure 4.16a. The vertical velocity is also significantly higher 40 mm away from the blade tip as seen by comparing figure 4.16b and figure 4.15b. This suggests that downwash affects a higher fraction of the blade if the geometric AOA is increased.

Figure 4.16c shows that tip vortices and downwash are significantly reduced if the effective AOA is minimal. As illustrated by figure 4.16d an increase in inlet velocity amplifies tip vortices and downwash. The maximum blade velocity is reduced, due to a higher aerodynamic force, which reduces the effective AOA. This reduces the downwash effect, but the greater pressure difference across the blade dominates the downwash effect.

### 4.4.3 Summary of observations

The main observations and relationships for leading edge vortices, tip vortices and downwash can be summarised as follows:

- LEVs have a negligible effect on the blade's lift force at 0AOA.
- The leading edge vortex phenomena is strongly dependent on the effective AOA. The flow does not separate from the blade, unless the effective AOA exceeds the separation threshold.
- At 9AOA, circulating flow from the leading edge vortex is transported downstream due to the free stream. This leads to the formation of a secondary vortex on the blade's suction side. Its strength increases if it is supplied with vorticity from the LEV and weakens constantly by shedding circulating flow into the wake.
- Secondary vortices lower the pressure in their vicinity, which increases the blade's lift force until the vortex core is located near the trailing edge. The pressure is then reduced on both blade sides, which reduces its lift force.
- Dynamic stall occurs as soon as the vortices are completely shed into the wake.
- Downwash and tip vortices increase as the pressure difference across the blade increases. This occurs at larger geometric AOAs, higher inlet velocities and higher blade velocities. Additionally, the effect of downwash reduces as the distance from the blade tip increases.

# Chapter 5

# Simplified 1D model of the blade

The chapter commences by describing the FSI algorithm containing the FEM solver and the heuristic flow model, which consists of diverse theoretical flow models. Additional information, such as the validation of the slender beam model and the mesh independence study, is given in appendix F. The heuristic flow model is described in section 5.2. It is then validated using a force analysis in which the determined lift force is compared to the forces extracted from the mesh-based FSI simulation. Lastly, the results of the simplified 1D model are stated.

## 5.1 Algorithm

The aim of this investigation is to find a fast, accurate and robust method to simulate the ACC fan unit. Therefore, this chapter focuses on whether the complex flow phenomena can be accurately modelled using a heuristic flow model. This flow model will be coupled to a simplified 1D model to simulate the fan blade's dynamic motion. Reducing the problem complexity, by using theoretical flow models coupled with a 1D beam model, will offer the most robust and computationally inexpensive method to simulate the aerodynamic damping of the oscillating fan blade.

The blade motion was solved numerically using the algorithm depicted in figure 5.1 and can be subdivided into the following steps:

**Step 1: Initialisation** This step is performed once at the beginning of the simulation and sets the general parameters. The blade's material properties, listed in table 2.1, were used to determine the global mass, damping and stiffness matrices as explained in section 3.2.3. None of these matrices are altered during the simulation process as the structural model is assumed to be linear. The time step is also not altered and therefore the effective stiffness matrix is constant throughout the entire simulation. The stiffness matrix is determined using the Euler-Bernoulli beam theory as discussed in section B.2.3.1. The blade geometry is simplified to accommodate the one-dimensional model and is depicted in appendix F.1. Prior to running the FSI simulation, the structural model was validated as shown in appendix F.

**Step 2: Time stepping loop** If the previous time step has fully converged, the simulation progresses by a time step size of 0.0044 s. The time step size was determined using equation (3.23) as was done for the mesh-based FSI simulation. This loop is repeated until the final simulation time of 10 s is reached.

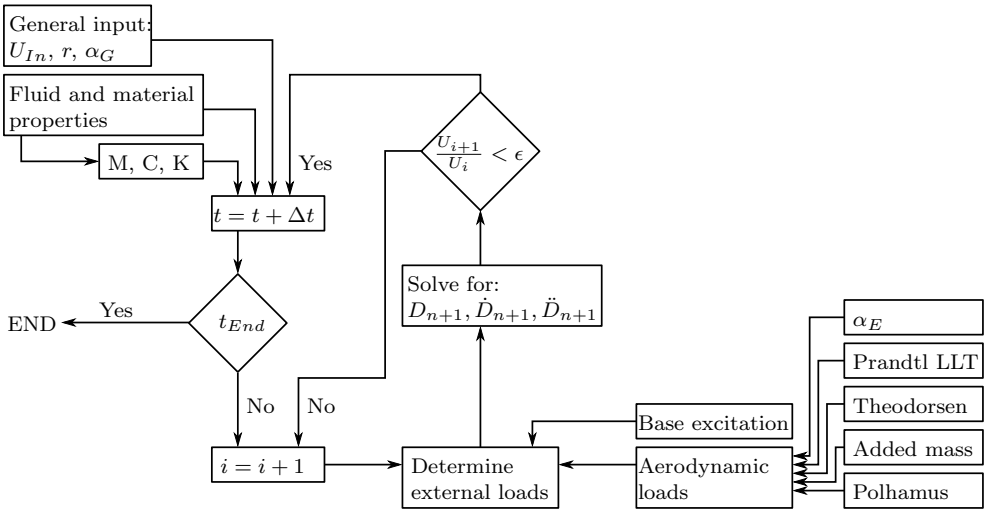


**Figure 5.1:** 1D beam model algorithm

**Step 3: Convergence loop** The inner loop is repeated at every time step and is necessary because, as equation (3.26) shows, the external loading at the new time step is required. The aerodynamic load depends on the blade velocity, which can only be obtained from the previous time step if no iterative loop is used. The inner loop ensures the solver's stability and increases the solution accuracy by iteratively determining the new velocity until it converges. The external load acting on the blade consists of the base excitation as well as the aerodynamic damping loads.

**Step 4: External loading** The heuristic flow model mentioned in section 5.2, is used to model the aerodynamic load. The blade surface is split into a finite number of segments, each with a structural node at its centre as shown in figure 5.2. The aerodynamic forces are calculated per segment and applied to each node. This method is known as strip theory or blade-element approach and is necessary, because the displacement and velocity are not uniform along the blade's length (Shyy *et al.*, 2013). Each node of the structural beam element has two DOF, which are also indicated in figure 5.2. The aerodynamic force has to be applied to the lateral translational DOF, which means that the blade's normal force has to be determined.

Firstly, the effective AOA is determined and adjusted using Prandtl's lifting line theory (LLT) to approximate downwash. The two-dimensional lift, drag and induced drag are determined from the experimental data given by Riegels (1961). As explained in section 4.4, the flow requires time to fully develop and only a fraction of the lift is generated. This is modelled using Theodorsen's function. The added mass effect and the Polhamus effect, used to approximate the additional lift created due to LEVs, are also implemented.

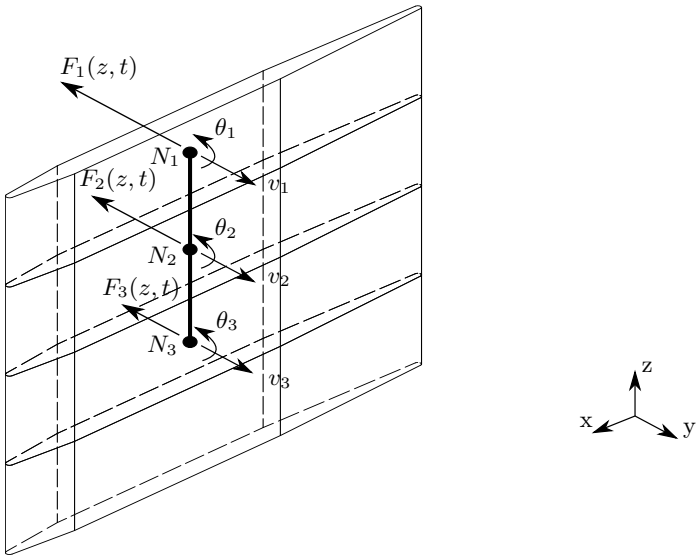


**Figure 5.2:** Blade is split into finite strips to determine the aerodynamic loading per structural node

**Step 5: Solving Newmark's equations** Equations 3.26 and 3.27 are solved sequentially. The tip displacement is recorded and the maximum tip displacement per frequency ratio is then plotted to give the transmissibility curves shown in section 5.4.

The iterative loop is repeated until the velocity at the new time step converges below the set tolerance value $\epsilon$.

## 5.2 Heuristic flow model

In this section the theoretical flow models will be discussed that are combined in the heuristic flow model. The steady state lift and drag coefficient are approximated using the experimental measurements from Riegels (1961) that are displayed in figure 2.3. An additional drag term has to be considered that exists due to tip vortices. Induced drag was covered in section 4.2.2 and can be minimised by increasing the AR of the blade (Wright and Cooper, 2015).

### 5.2.1 Prandtl's lifting line theory (LLT)

The lift force across a finite wing is not uniform due to flow effects occurring near the blade's tip. Prandtl's LLT is used to describe the lift distribution over a finite wing. The model is applicable for incompressible flow and for wings with an AR greater than 7 (Chattot and Hafez, 2015). The fluid domain is bound by a symmetry plane at its bottom. This means that during the FSI simulation, the blade length is seen as double its true length. The virtual blade's AR is:

$$AR = \frac{2\,L_{Bl}}{c} = \frac{1.12\,m}{0.12\,m} \tag{5.1}$$

The virtual AR will be used in the heuristic model as it should replicate the FSI simulation.

Figure 5.3a shows the representation of a blade by a single bound vortex. According to the Helmoltz theorem, the bound vortex cannot end in the fluid and thus expands as two free-trailing vortices downstream. The lift force is given by the Kutta-Joukowski theorem as $F_L = \rho U_{In}\Gamma$ (Anderson, 1991). $\Gamma$ is the circulation strength. According to this theorem the lift force would increase to infinity near the blade tips as $\Gamma$ goes to infinity, due to the infinite length of the free vortices. This is implausible and Prandtl suggested replacing the single horseshoe vortex by a finite number of horseshoes with a small circulation strength as shown in figure 5.3b. The circulation strength of each horseshoe is superimposed. If infinitely many horseshoes are used, a continuous vortex sheet is formed where the circulation is maximum at the blade's centre and minimum at the tips.

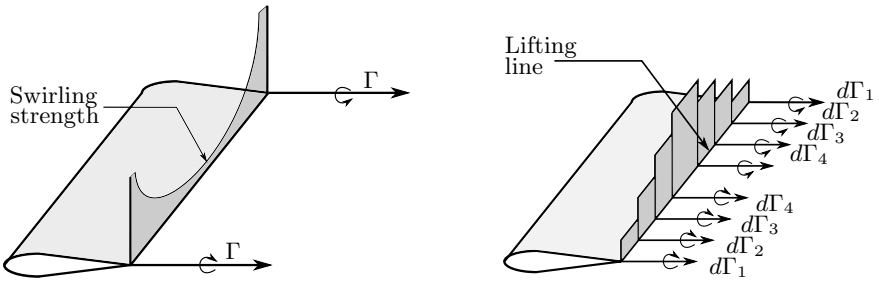


**(a)** Single bound horseshoe vortex **(b)** Superimposed horseshoe vortices

**Figure 5.3:** Prandtl superimposes several bound vortices instead of approximating the blade by a single one

The lift force can then be written as:

$$F_L = \rho U_{In} \int_{-L_{Bl}}^{L_{Bl}} \Gamma(z)dz \tag{5.2}$$

Instead of integrating the continuous circulation strength function, which is difficult to find for non-elliptical wings, the lift force can be approximated by (Anderson, 1991):

$$F_L = \rho U_{In} \sum_{j=1,odd}^{\infty} A_j sin\,(j\theta) \tag{5.3}$$

where $\theta$ is found through the following transformation:

$$z = -\frac{L_{Bl}}{2} cos\theta \tag{5.4}$$

The problem with equation (5.3) is that both the lift force and the coefficients $A_j$ are not known. After some mathematical manipulation the angle of attack can be found (Anderson, 1991):

$$\alpha = \frac{2L_{Bl}}{\pi c} \sum_{j=1,odd}^{\infty} A_j sin(j\theta_i) + \sum_{j=1,odd}^{\infty} jA_j \frac{sin(j\theta_i)}{sin(\theta_i)} \tag{5.5}$$

here the only unknowns are the coefficients $A_j$. The angle $\alpha$ is given in radians with a non-zero magnitude. The magnitude is of no importance as the lift distribution is normalised with respect to its maximum value at the blade's mid span. Equation (5.5) gives a system of $j$ equations and can be solved for the coefficients. Figure 5.4 compares the normalised lift distribution over an elliptical wing with that of the blade under investigation. The x-axis is the normalised spanwise location. At the root of the blade (z=0) the lift is maximum and at the wing tip (z=1) the lift is zero.

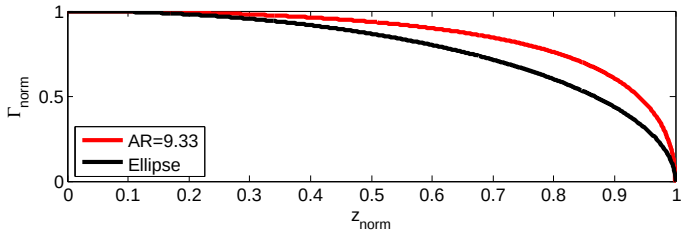


**Figure 5.4:** Comparison of the lift distribution for an elliptical wing and the rectangular blade

### 5.2.2 Theodorsen function

Theodorsen derived an expression for the lift coefficient of a flat plate plunging and pitching in two-dimensional space in an inviscid and incompressible fluid (Brunton, 2012). The unsteady lift coefficient for a sinusoidally plunging aerofoil is given by Gulcat (2016):

$$C_L = 2\pi C(k)\left(\frac{U_{Bl}}{U_{In}} + \alpha_G\right) + \frac{\pi c}{2U_{In}^2}\dot{U}_{Bl} = C(k)C_L + \frac{\pi c}{2U_{In}^2}\dot{U}_{Bl} \tag{5.6}$$

The first term gives the circulatory component, which is the three-dimensional lift multiplied by the complex Theodorsen function $C(k)$, which depends on the reduced frequency $k$. The dimensionless parameter $k$ is used to define the unsteadiness of the problem (Shyy *et al.*, 2013). It is given by:

$$k = \frac{\omega c}{2U_{In}} \tag{5.7}$$

As discussed in the beginning of section 4.4, the magnitude of $C(k) \leq 1$ to simulate the fractional lift developed. $C(k)$ is an expression of Hankel functions. The magnitude and phase of $C(k)$ as a function of $k$ are given in figure 5.5.

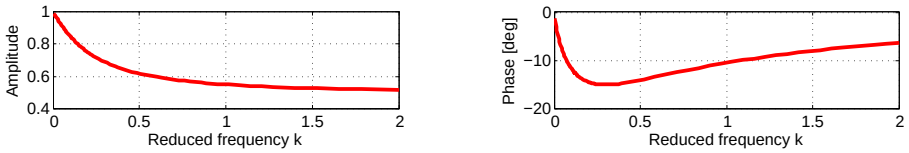


**(a)** Magnitude **(b)** Phase shift

**Figure 5.5:** Theodorsen function

The second term in equation (5.6) is the non-circulatory term due to the blade's transverse acceleration $\dot{U}_{Bl}$. In other words, the second term is the added mass force coefficient (Shyy *et al.*, 2013).

### 5.2.3 Added mass effect

The non-circulatory coefficient given in equation (5.6) can be derived from the kinetic energy equation for a static fluid (Brennen, 1982):

$$T_{KE} = \frac{\rho}{2} \int_V U_i U_i dV \tag{5.8}$$

where $U_i$ are the Cartesian velocity components and $V$ is the entire fluid volume. The kinetic energy of the fluid is increased if work is done on it by the structure. The structure thus experiences a counter force given as:

$$F_{AM} = -\rho I \frac{dV}{dt} \quad \text{where} \quad I = \int_V \frac{U_i}{U_\infty} \frac{U_i}{U_\infty} dV \tag{5.9}$$

$\rho\, I$ resembles the fluid mass that is accelerated by the blade. Using potential flow theory the added mass of an oscillating plate in a static fluid is given by (Harris and Piersol, 2002):

$$m_{AM} = \rho\pi(c/2)^2 L_{Bl} \tag{5.10}$$

According to (Konstantinidis, 2013), the above equation is only applicable if the surrounding fluid is static. A correction term was determined by Konstantinidis (2013) for a cylinder oscillating transverse to a free stream. This

term is expanded in appendix F to apply to the flapwise oscillating fan blade. The added mass force is then given by:

$$F_{AM} = m_{AM}\dot{U}_{Bl} = G\frac{\rho\pi c^2}{4}L_{Bl}\dot{U}_{Bl} \tag{5.11}$$

where $G$ is a dimensionless function of time, geometric angle of attack, blade velocity and inlet velocity. $G$ is given as:

$$G = \frac{U_{Bl}(z,t) - U_{in}\sin(\alpha_G)}{\sqrt{U_{In}^2 - 2U_{In}U_{Bl}(z,t)\sin(\alpha_G) + U_{Bl}^2(z,t)}} \tag{5.12}$$

The added mass $m_{AM}$ was calculated for the two geometric AOAs and the different inlet velocities for one entire oscillation cycle. The results are stated in table 5.1.

**Table 5.1:** Average added mass for one oscillation cycle

| $U_{In}$ | 0AOA | 9AOA |
|---|---|---|
| $10\,m/s$ | $7.5\,g$ | $9.5\,g$ |
| $15\,m/s$ | $4.3\,g$ | $9.7\,g$ |
| $20\,m/s$ | $2.6\,g$ | $9.8\,g$ |

The results show that the added mass reduces as the inlet velocity is increased, if the geometric AOA is zero. Therefore, the blade's $r_P$ value approaches unity as the inlet velocity is increased as stated in section 2.5. For 9AOA, the added mass increases as the inlet velocity is increased. This explains the observation made in section 2.5, that the natural frequency of the blade decreases as the inlet velocity is increased.

### 5.2.4 Polhamus leading edge suction analogy

The leading edge suction analogy was developed by Polhamus to model the additional lift force generated by the leading edge vortex for low AR delta wing aircraft (Gulcat, 2016). The suction force is determined using potential flow theory and then rotated by 90 ° to give the normal LEV force on the blade (Bos, 1994). The additional lift force is determined by:

$$C_L = K_v \sin(\alpha_G)^2 \cos(\alpha_G) \tag{5.13}$$

where $K_v$ is the vortex lift term. Assuming linearised flow and a rectangular blade with no sweep, it is given by Bos (1994) as:

$$K_v = C_{L,\alpha} - \frac{C_{L,\alpha}^2}{\pi e AR} \tag{5.14}$$

The lift gradient $C_{L,\alpha}$ for a finite wing is given by Anderson (1991) as:

$$C_{L,\alpha} = \frac{2\pi}{1 + 2/(eAR)} \tag{5.15}$$

The blade's normal force has to be determined to accurately predict the loading on the beam model. Thus, substituting equation (5.14) and equation (5.15) into equation (5.13) gives the normal force coefficient as:

$$C_N = \frac{C_L}{\cos(\alpha_G)} = \frac{2\pi eAR}{eAR+2}\left(1 - \frac{2}{eAR+2}\right)\sin(\alpha_G)^2 \tag{5.16}$$

## 5.3 Force analysis

The heuristic fluid model was validated by comparing its force predictions with the mesh-based FSI extracted forces. To ensure that the aerodynamic loading is modelled accurately in time and space, the blade was subdivided into 20 equally sized ISO clips over which the forces were averaged and recorded for an entire oscillation cycle. The comparison was done for the following simulations.

### 5.3.1 0AOAV10r0.99

0AOAV10r0.99 specifies the simulation performed at 0AOA with an inlet velocity of approximately 10 m/s and a frequency ratio of 0.99. Figure 5.6 illustrates the forces predicted per ISO clip. The total force comprises of the single theoretical flow models explained in the previous section. Their individual contribution is also displayed in the figures. The two instances display the forces when the blade displacement is minimum and maximum.

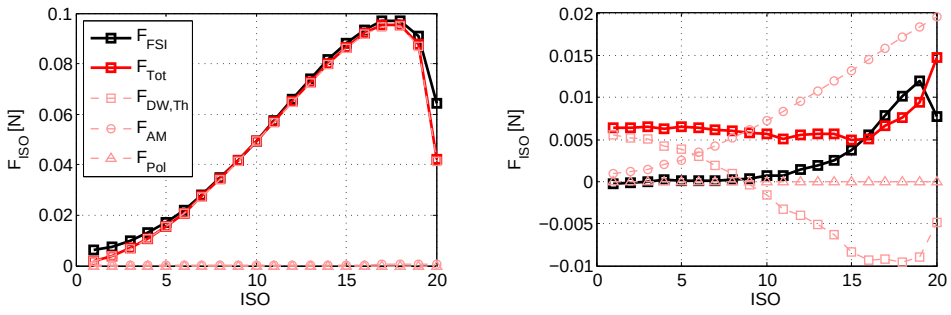


**(a)** Minimum $D_T$ **(b)** Maximum $D_T$

**Figure 5.6:** Mesh-based and theoretically predicted normal forces for each ISO clip of the 0AOAV10r0.99 simulation

At minimum blade displacement, the effective AOA is maximum and the blade's acceleration is minimum. Thus, viscous forces dominate and the added mass force is negligible. A good correlation between the heuristic model and the mesh-based FSI simulation exists as seen in figure 5.6a.

At maximum tip displacement, the blade velocity and acceleration are minimum and maximum respectively. This means that inertial effects dominate

the viscous effects. Therefore, the added mass effect is the main contributor to the total force and the viscous forces are negligible. Figure 5.6b shows discrepancies between the total theoretical force and the mesh-based predicted force. These are negligible, because the difference is relatively small compared to the total force over the entire oscillation cycle.

The Polhamus force, given by equation (5.16), is zero at all time instances if the geometric AOA is zero. This is accurate, as observations from the FSI simulation have shown that only small LEVs occur with a negligible effect on the blade's force distribution. For this reason, the Polhamus effect cannot be validated using the 0AOA simulations.

Figure 5.8a gives the total force across the whole blade for an entire oscillation cycle. The maximum deviation from the mesh-based force is observed when the blade accelerates until it reaches its maximum velocity. From figure 5.6a it can be concluded that the viscous force is overdetermined at these instances. Similar results were achieved for the $V15$ and $V20$ simulations. These deviations are negligible as shown in figure 5.8a. For that reason, the heuristic model accurately predicts the aerodynamic loading at $0AOA$.

### 5.3.2 9AOAV10r0.99

In section 4.4.1, four instances are depicted to show the evolution of LEVs over a whole oscillation cycle at 9AOA. The forces were extracted at the same instances and compared to the force predicted by the heuristic model in figure 5.7.

Large deviations between the heuristic model and the mesh-based simulation can be observed from the figure. The heuristic model underpredicts the aerodynamic force at instances $t_1$, $t_2$ and $t_3$. At $t_4$, it mainly overpredicts the loading across the blade.

As shown by figure 2.3, the slope of the steady state lift decreases as the effective AOA exceeds approximately 6 °. This leads to the observed constant lift prediction across the blade. For example, the approximated lift force is roughly constant from ISO 1 to ISO 19 at instance $t_2$. This is an inaccurate approximation of the lift force.

In the previous section, the heuristic model compared very well with the mesh-based results. The difference is that LEVs are formed and that the Polhamus model fails to accurately predict these. The leading edge suction analogy was derived for delta wing aircraft and is not directly applicable here.

The additional gain or loss in lift force can be explained by referring back to section 4.4:

**Maximum tip displacement at $t_1$:** A leading edge vortex and a secondary vortex were observed at ISO 5 in figure 4.12a. These lead to a pressure reduction on the blade's suction side and thus amplify the pressure difference across the blade. The lift further increases while progressing

towards the blade tip until it reaches its maximum value at ISO 14. This is due to stronger LEVs as shown for ISO 15 in figure 4.13a. A drastic drop in lift is observed close to the blade tip. The effective AOA reduces due to downwash. This further prevents the formation of strong LEVs and the pressure difference across the blade reduces significantly.

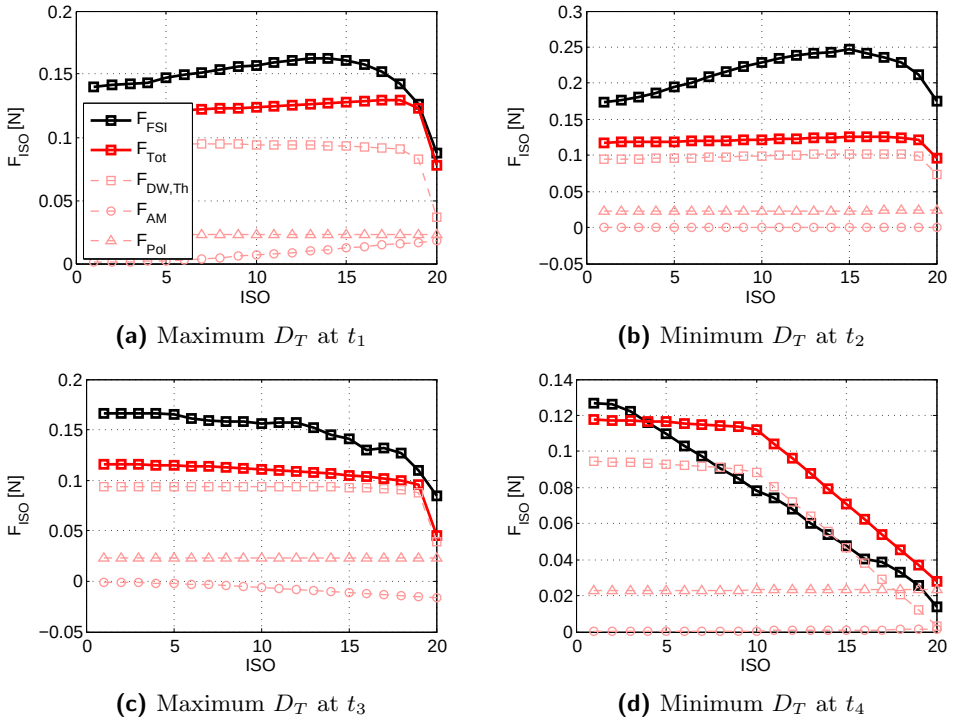


**(a)** Maximum $D_T$ at $t_1$

**(b)** Minimum $D_T$ at $t_2$

**(c)** Maximum $D_T$ at $t_3$

**(d)** Minimum $D_T$ at $t_4$

**Figure 5.7:** Mesh-based and theoretically predicted normal forces for each ISO clip of the 9AOAV10r0.99 simulation

**Minimum tip displacement at $t_2$, AFS:** At this instance the maximum effective AOA is reached because the blade moves AFS with maximum velocity. This leads to a larger deviation between the heuristic model and the mesh-based FSI simulation. The vortices formed on the blade's suction side further strengthen and lower the pressure. A less significant lift drop is observed near the tip. As shown in figure 4.14b, a small LEV forms at ISO 20 that amplifies the lift near the blade tip. Figure 4.16a shows significant downwash at this instance, but tip vortices and the LEV are the dominating effects.

**Maximum tip displacement at $t_3$:** The observations at ISO 15 have shown that only small vortices are formed near the leading edge and that most of the vortex structure is being convected downstream. This not only reduces the lift force, but also leads to the observed force fluctuations across the blade as shown in figure 5.7c. The fluctuations are more

dominant towards the blade tip. At ISO 5, a strong secondary vortex is observed that is being convected downstream. It reduces the pressure on the blade's pressure side as its core is located near the trailing edge. This leads to a further force reduction from $t_2$ to $t_3$.

**Minimum tip displacement at $t_4$, WFS:** The heuristic model overpredicts the lift force almost across the entire blade as shown in figure 5.7d. The blade moves with maximum velocity with the free stream. The effective AOA is thus at its minimum value, which leads to observed vortex shedding at ISO 15 and 20. This phenomenon is known as dynamic stall. A secondary vortex is still attached to the trailing edge at ISO 5, but it reduces the pressure difference across the blade and also leads to a loss of lift.

The heuristic model is not capable of accurately simulating the aerodynamic forces as shown in figure 5.8b. To model the complex initialisation, growth, decay and shedding of the leading edge vortices, an empirical factor is derived in the following section to adjust the Polhamus factor.

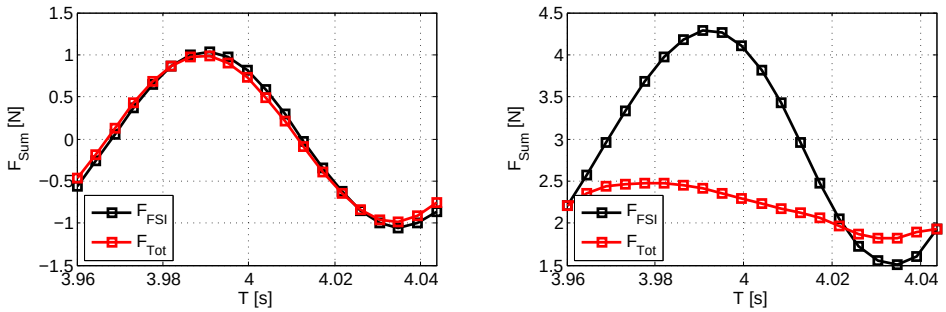


**(a)** 0AOAV10r0.99 **(b)** 9AOAV10r0.99

**Figure 5.8:** Comparison of the mesh-based and theoretically predicted blade's total normal force over an entire oscillation cycle

### 5.3.3 Empirical model to simulate vortex dynamics

The previous section indicates that a more advanced form of modelling the vortex development and breakdown is required to accurately simulate the lift force. Polhamus researched the phenomenon of LEVs for delta wing aircraft as discussed in Katz (1999). His findings are limited to low AR delta wing aircrafts and no information is given for large rectangular AR blades. Thus, an empirical factor $A_{Pol}$ is introduced that is multiplied by the Polhamus function to adjust it to the given geometry. $A_{Pol}$ is found by minimising:

$$E = \sum (V_{Emp} - A_{Pol}(z, \alpha_E))^2 \tag{5.17}$$

where $V_{Emp}$ is given by:

$$V_{Emp} = \frac{F_{FSI} - (F_{2D,LLT,Th} + F_{AM})}{F_{Pol}} \tag{5.18}$$

The predicted force of the basic heuristic model is subtracted from the extracted mesh-based FSI force $F_{FSI}$. The basic model includes the two-dimensional lift and drag force adjusted by the Theodorsen function and Prandtl's LLT function $F_{2D,LLT,Th}$. It also includes the added mass force $F_{AM}$. The difference is then divided by the predicted Polhamus force $F_{Pol}$ for each blade strip. $V_{Emp}$ is displayed for all ISO clips over an entire oscillation cycle in figure 5.9 for V10 and V20.

The magnitude fluctuates more substantially for V10 than for V20. This proves the statement made in section 4.4.1 that vortex formation and breakdown are more pronounced at lower inlet velocities, because the range of the effective AOA is larger. The peaks of $V_{Emp}$ occur at different time instances. This is due to the difference in the frequency ratio at which the maximum tip displacement is observed for the two inlet velocities.

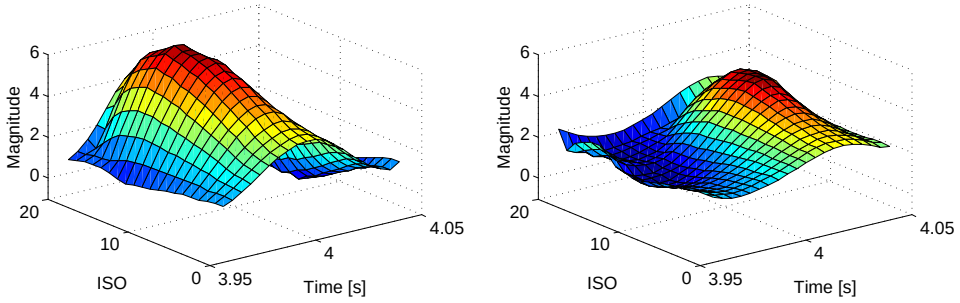


**(a)** 9AOAV10r0.99 **(b)** 9AOAV20r0.98

**Figure 5.9:** Function to be approximated by $A_{Pol}$ to adjust the Polhamus factor for the given vortex dynamics

$A_{Pol}$ approximates $V_{Emp}$ using a function that depends on the spanwise location and the effective AOA. The vortex dynamics strongly depend on these two factors as observed in section 4.4.1. $A_{Pol}$ is given by:

$$A_{Pol} = (A_1 z + A_2)\left(A_3 \alpha_E^2 + A_4 |\alpha_E| + A_5\right) \tag{5.19}$$

where $A_1$ to $A_5$ are unknown coefficients that are found by a particle swarm optimisation algorithm. The algorithm is explained in section F.5. The function is expanded and the coefficients for each term are given in table F.1. Figure 5.10 compares $V_{Emp}$ and $A_{Pol}$ for 9AOAV15r0.99. The magnitude of $A_{Pol}$ does not vary as significantly as that of $V_{Emp}$ near the blade base and tip. Furthermore, the approximation function $A_{Pol}$ is smoother than $V_{Emp}$. Besides these minor discrepancies, the approximation is sufficiently accurate.

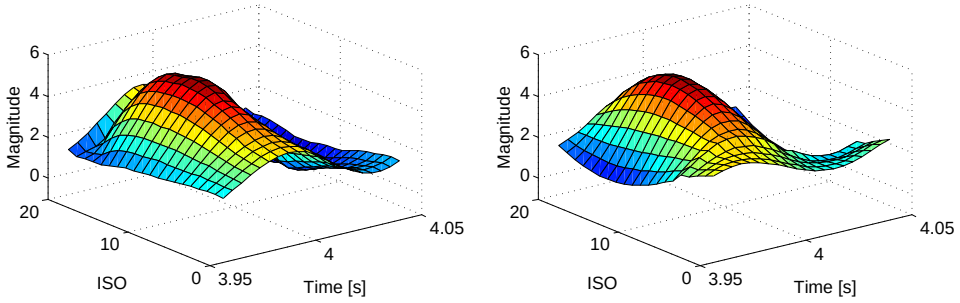


**(a)** $V_{Emp}$ **(b)** $A_{Pol}$

**Figure 5.10:** Comparison of $V_{Emp}$ and $A_{Pol}$ for 9AOAV15r0.99

The adjusted Polhamus model is used in the heuristic flow model. Figure 5.11 depicts the force distribution across the blade at $t_2$ and the total blade loading per oscillation cycle. The use of $A_{Pol}$ allows for an accurate prediction of the aerodynamic loading.

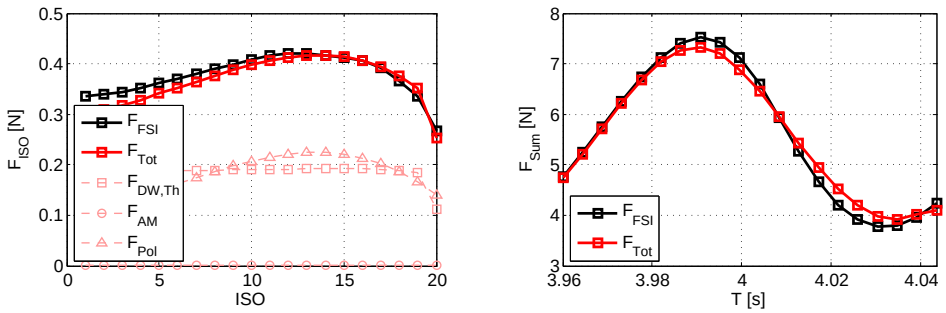


**(a)** Forces at $t_2$ **(b)** Forces for whole cycle

**Figure 5.11:** Force prediction with the empirical Polhamus factor used for 9AOAV15r0.99

## 5.4 FSI results

In figure 5.12 the experimental and theoretical transmissibility curves are compared. The 1D beam model under- and overpredicts the tip displacement for 0AOA and 9AOA respectively.

Table 5.2 compares the maximum experimental and numerical tip displacements and states the relative deviation of the 1D beam simulation. The table also includes the results for the 9AOA simulation when the empirical factor is not employed. The use of $A_{Pol}$ significantly reduces the relative deviation at 9AOA.

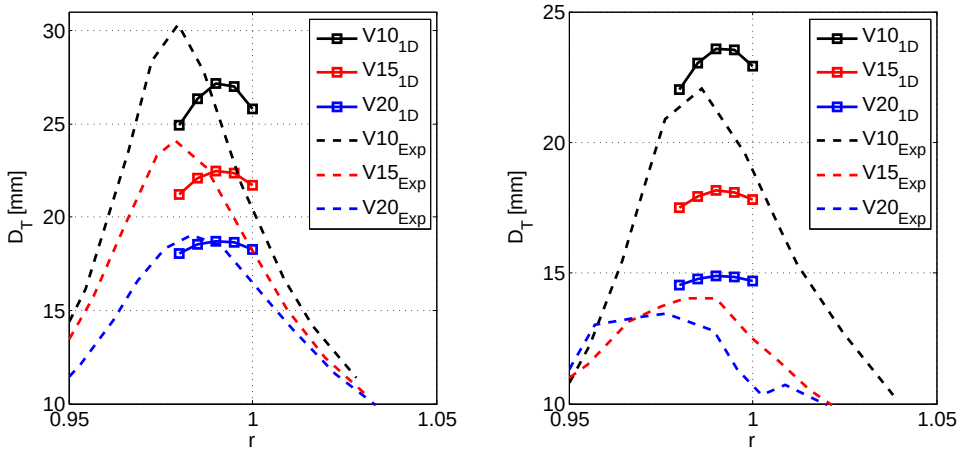


**(a)** 0AOA **(b)** 9AOA

**Figure 5.12:** 1D beam model validation for the two different geometric AOAs

The empirical factor adjusts the heuristic flow model to obtain similar forces as obtained with the SST transition model in the mesh-based FSI simulation. For that reason, the results obtained at 9AOA are very similar. The table shows that the maximum relative deviation is approximately 29 % if the empirical factor is used. This again occurs at 9AOAV15. As previously mentioned, inaccuracies for these experimental measurements are a possible reason for the large deviation. Otherwise, the maximum relative deviation is below 11 %, which is acceptable.

**Table 5.2:** 1D beam peak tip displacement verification

| $AOA$ | $V$ | $D_{Exp}$ $[mm]$ | $D_{1D}$ $[mm]$ | RD [%] |
|---|---|---|---|---|
| 0 | 10 | 30.324 | 27.16 | -10.43 |
| | 15 | 24.114 | 22.46 | - 6.86 |
| | 20 | 19.025 | 18.72 | - 1.60 |
| 9 (Emp) | 10 | 22.056 | 23.58 | 6.91 |
| | 15 | 14.045 | 18.15 | 29.23 |
| | 20 | 13.457 | 14.88 | 10.57 |
| 9 | 10 | 22.056 | 32.82 | 48.80 |
| | 15 | 14.045 | 31.22 | 122.29 |
| | 20 | 13.457 | 28.72 | 113.42 |

## 5.5 Suitability of the 1D beam model for simulating the aerodynamic damping of the ACC fan

The simplified 1D beam model is based on the Euler-Bernoulli beam theory and is coupled with a heuristic flow model to simulate the aerodynamic loading. The model combines existing potential flow models to simulate the observed flow phenomena from section 4.4.1. This leads to accurate predictions of the tip displacement at 0AOA, but fails to accurately model the aerodynamic damping force at 9AOA. The Polhamus leading edge suction analogy underpredicts the force created by the leading edge vortices. Therefore, an empirical factor, based on the effective AOA and the spanwise location, is used to improve the model's accuracy. This makes the model unsuitable for simulating the aerodynamic damping of the ACC fan, because no force data is available to calibrate the empirical factor.

# Chapter 6

# Meshless FSI analysis

This chapter commences by explaining the mathematical and numerical background of the Finite Pointset Method (FPM). This is followed by a short description of the coupling process between FPM and the Euler-Bernoulli beam model. Flow comparisons are then made with the mesh-based FSI simulation to address certain issues of FPM. Lastly, the FSI results obtained using FPM are compared to the experimental results. Solutions are also mentioned to the existing problems of modelling the aerodynamic damping of the oscillating fan blade using FPM. Additional information such as point cloud independence can be found in appendix G.

## 6.1 FPM background

One project objective is to find a suitable method to model the ACC fan unit. The simplified 1D beam model is not applicable, as discussed in section 5.5. The mesh-based method on the other hand is a suitable option, but has the disadvantage that mesh motion can lead to cell deterioration. This can lead to numerical instabilities and can negatively affect the solution accuracy (Liu and Liu, 2003).

To circumvent these disadvantages, a different approach is considered. FPM is a meshless method that solves the governing equations using a set of numerical points. It is coupled with the Euler-Bernoulli beam model, as it is computationally inexpensive and accurately models the structural dynamic response as shown in appendix F.

### 6.1.1 Mathematical model

FPM is a fully Lagrangian method where the simulation domain is discretised using a finite number of numerical points. These move at fluid velocity and carry flow information such as fluid density, pressure, temperature and so forth (Kuhnert, 1999). The partial differential equations to be solved are:

**Navier Stokes equation:** The fluid is considered to be incompressible and is described in the Lagrangian framework.

$$\rho\frac{\partial v_i}{\partial t} = -\frac{\partial p}{\partial x_i} + \mu\left(\frac{\partial^2 v_i}{\partial x_i^2} + \frac{\partial^2 v_i}{\partial x_j^2} + \frac{\partial^2 v_i}{\partial x_k^2}\right) + \rho f_i \tag{6.1}$$

The Lagrangian Navier Stokes equation does not contain a convection term. Equation (6.1) is therefore a linear equation and does not require advanced upwind differencing schemes to model convection (Versteeg and Malalasekera, 2007).

**Mass conservation:** In FPM, no mass is assigned to the numerical points. This has the advantage that points can easily be added or removed to ensure a well distributed point cloud. Mass is conserved using the mass conservation equation given by equation (3.2).

Smoothed Particle Hydrodynamics (SPH), was the first meshless method that is widely used nowadays (Liu and Liu, 2003). It's difference to FPM is that each particle carries mass and therefore particles cannot be simply added or removed, otherwise the mass conservation law is violated.

**New point location:** After each time step the new point location has to be determined. A second order explicit time stepping method is used to solve:

$$\frac{D\vec{x}_{P,i}}{Dt} = \vec{U} \tag{6.2}$$

#### 6.1.1.1 CFL condition

One major drawback of FPM is that the points can only be moved explicitly. This limits the time step size by the Courant-Friedrich-Lewys (CFL) condition. The CFL-condition ensures numerical stability for the explicit time stepping scheme. For grid based methods the CFL condition is given by (Seifarth, 2014):

$$U\frac{\Delta t}{\Delta x} < 1 \tag{6.3}$$

The time step $\Delta t$ is restricted so that fluid information, travelling with the local velocity $U$, cannot surpass one cell, with length $\Delta x$, in one step. This condition is adapted for FPM and is given as:

$$U\frac{\Delta t}{h_{SL}} = \alpha \tag{6.4}$$

where $\alpha$ is a constant usually set to less than 0.2 depending on the problem. The smoothing length $h_{SL}$ is discussed in the following section.

The time step of implicit methods is not limited by the CFL condition, but no implicit method for point movement has been developed so far.

### 6.1.2 Pointcloud management

For an accurate approximation of the fluid continuum, the point cloud has to be sufficiently dense (Jefferies *et al.*, 2014). Each point considers its neighbours within its support domain when approximating the function values for the next time step (Tiwari *et al.*, 2006*b*). The support domain is visualised in figure 6.1 in two-dimensional space. The smoothing length $h_{SL}$ is the radius of the support domain. Points lying outside of the support domain of point $p_i$ are not considered when approximating the function value at $p_i$ (Tramecon *et al.*, 2006).
Due to point motion, large holes or point clusters can form that decrease the solution's order of accuracy. To prevent this, points can easily be added or removed in FPM. This is done if the distance between the points does not meet the following two conditions:

$$h_{Max} = \alpha_{Max} h_{SL} \tag{6.5}$$
$$h_{Min} = \alpha_{Min} h_{SL} \tag{6.6}$$

where $\alpha_{Max} > \alpha_{Min}$ and both are constants less than one.

### 6.1.3 Approximation of derivatives

Spatial derivatives are approximated in FPM using a generalized finite difference method (Jefferies *et al.*, 2014). Stencils are used in finite difference methods to approximate derivatives at the grid points (Seifarth, 2014). In FPM for example, the first and second derivatives with respect to x are given by:

$$\frac{\partial f(x_i)}{\partial x} = \sum_{j=1}^{P_i} c_{ij}^{x} f(x_j), \quad \frac{\partial^2 f(x_i)}{\partial x^2} = \sum_{j=1}^{P_i} c_{ij}^{xx} f(x_j) \tag{6.7}$$

where the derivative at point $i$ is approximated using the function values of all points $P_i$ in the support domain. The first and second order stencil coefficients with respect to x are $c_{ij}^{x}$ and $c_{ij}^{xx}$ respectively.

A second order Taylor series is required to approximate the derivatives of partial differential equations of equivalent order:

$$\begin{aligned}\sum_{j=1}^{P_i} c_{ij}^{*} f(\vec{x}_j) \approx f(\vec{x}_i) \sum_{j=1}^{P_i} c_{ij}^{*} &+ \frac{\partial f(\vec{x}_i)}{\partial x} \sum_{j=1}^{P_i} c_{ij}^{*} dx_j + \frac{\partial f(\vec{x}_i)}{\partial y} \sum_{j=1}^{P_i} c_{ij}^{*} dy_j \\ &+ \frac{\partial^2 f(\vec{x}_i)}{\partial x \partial y} \sum_{j=1}^{P_i} c_{ij}^{*} dx_j dy_j + 0.5 \frac{\partial^2 f(\vec{x}_i)}{\partial x^2} \sum_{j=1}^{P_i} c_{ij}^{*} dx_j^2 \\ &+ 0.5 \frac{\partial^2 f(\vec{x}_i)}{\partial y^2} \sum_{j=1}^{P_i} c_{ij}^{*} dy_j^2 + E_{ij}\end{aligned} \tag{6.8}$$

Superscript * is used to represent one of six FPM stencils ($c^0$ , $c^x$ , $c^y$ , $c^{xy}$ , $c^{xx}$ , $c^{yy}$) that have to be determined for each point in two dimensions. Rearranging for the error $E_{ij}$ and writing equation (6.8) as a system of linear equations gives:

$$\begin{pmatrix} E_{i,1} \\ \vdots \\ E_{i,p_i} \end{pmatrix} = \boldsymbol{r}_i^* - \begin{pmatrix} 1 & \cdots & 1 & 1 & 1 & \cdots & 1 \\ dx_1 & \cdots & dx_{i-1} & 0 & dx_{i+1} & \cdots & dx_{p_i} \\ dy_1 & \cdots & dy_{i-1} & 0 & dy_{i+1} & \cdots & dy_{p_i} \\ (dxdy)_1 & \cdots & (dxdy)_{i-1} & 0 & (dxdy)_{i+1} & \cdots & (dxdy)_{p_i} \\ dx_1^2 & \cdots & dx_{i-1}^2 & 0 & dx_{i+1}^2 & \cdots & dx_{p_i}^2 \\ dy_1^2 & \cdots & dy_{i-1}^2 & 0 & dy_{i+1}^2 & \cdots & dy_{p_i}^2 \end{pmatrix} \begin{pmatrix} c_{i,1}^* \\ \vdots \\ c_{i,p_i}^* \end{pmatrix} \tag{6.9}$$

To obtain the derivatives stated in equation (6.7), the error $E_{ij}$ has to be minimised and $\boldsymbol{r}_i^*$ has to be set as:

$$\boldsymbol{r}_i^x = \begin{pmatrix} 0 & 1 & 0 & 0 & 0 & 0 \end{pmatrix}^T \quad \text{and} \quad \boldsymbol{r}_i^{xx} = \begin{pmatrix} 0 & 0 & 0 & 0 & 2 & 0 \end{pmatrix}^T \tag{6.10}$$

respectively. FPM has the advantage that boundary conditions can easily be incorporated using the FPM stencils by adjusting $\boldsymbol{r}_i^*$ for boundary particles. On the other hand, enforcing boundary conditions for SPH is more complex (Kuhnert, 1999).

A weighting function is introduced to reduce the influence of points farther away from the central point. The use of a Gaussian weighting function (Kuhnert and Tiwari, 2001):

$$w(\vec{x}_i - \vec{x}, h_{SL}) = \begin{cases} \exp\left(-\alpha \frac{||\vec{x}_i - \vec{x}||^2}{h_{SL}^2}\right) & \text{if } \frac{||\vec{x}_i - \vec{x}||}{h_{SL}} \leq 1 \\ 0 & \text{otherwise} \end{cases} \tag{6.11}$$

is displayed in figure 6.1 where $\alpha$ is a positive constant. Every point's FPM stencil is determined by minimising (Tramecon *et al.*, 2006):

$$\sum_{j=1}^{P_i} w_{ij} E_{ij}^2 = min \tag{6.12}$$

## 6.2 FPM set-up and coupling with the 1D beam model

The meshless and mesh-based FSI simulations are set up in the exact same way. The fluid domain, boundary conditions, initial conditions and the material properties are equivalent for both simulations. The only differences are:

**Viscous model:** The current in-house[1] version of FPM (August, 2016) does not incorporate a large variety of viscous models. The k-$\epsilon$ model was

[1]The FPM software is currently being developed by the grid-free methods department of the Fraunhofer Institute for Industrial Mathematics (ITWM), which is situated in Kaiserslautern, Germany.

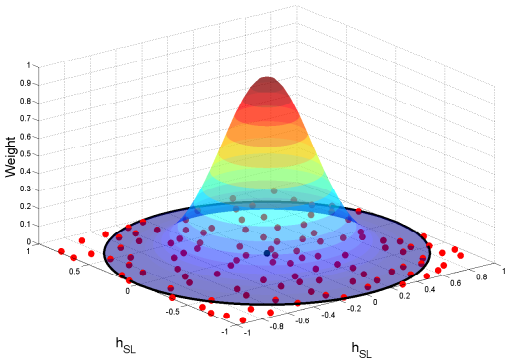


**Figure 6.1:** Support domain with radius $h_{SL}$. Neighbouring particles are indicated in red with centre point in blue. The influence of neighbouring particles is weighed using a weighting function

therefore chosen to model turbulence. As mentioned in section 4.2.1.1, the k-$\epsilon$ model is not advised for external flow and has difficulties in predicting boundary layer separations. This could cause inaccuracies that have to be considered in the results analysis.

**Spatial discretization:** The domain is discretized using numerical points instead of a mesh. An advantage of FPM over other meshless methods is that the smoothing length can easily be altered in space and in time. The discretization around the blade is refined to approximate the complex fluid flow more accurately and is coarsened further away from the blade. Figure 6.2 depicts the variation of the smoothing length in the fluid domain. Four different point clouds, each with a different number of points, were compared to ensure the simulation's independence of it. This is done in appendix G.

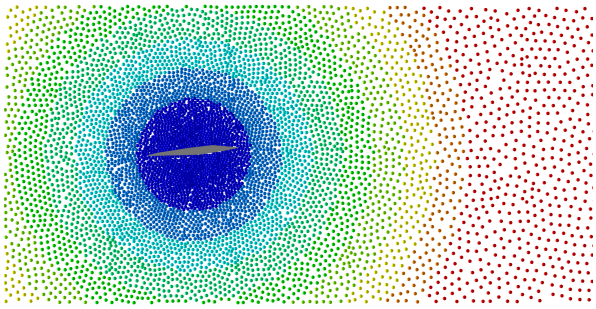

**Figure 6.2:** Spatial variation of the smoothing length on the bottom symmetry plane. Inlet is on the left with a radial refinement towards the blade's leading edge

**Exchange of interface information:** FPM requires a three-dimensional rep-

resentation of the blade, but only a one-dimensional beam model is used. The deflection of the beam is thus used to move a three-dimensional silhouette for the fluid solver. Similar to the strip theory used in chapter 5, the force is interpolated over a number of blade segments and given to the corresponding structural node.

**Coupling:** Due to the fine smoothing length near the blade and the high fluid velocities in this area, the FPM time step is restricted by the CFL condition and is notably smaller than the time step of the structural solver. Subcycling, discussed in section 3.1.2, and a weak coupling are used to reduce the computational cost of each simulation. The simulation is robust where several FPM time steps are performed in a single time step of the structural solver. The force is communicated to the structural solver at the required times and the displacement given to the FPM solver is linearly extrapolated. A good prediction of the blade motion is given by:

$$\boldsymbol{D}_{Ext,n} = \boldsymbol{D}_n + \dot{\boldsymbol{D}}_n \Delta t_{FEM} + 0.5 \ddot{\boldsymbol{D}}_n \Delta t_{FEM}^2 \tag{6.13}$$

where the blade displacement in the FPM solver is linearly varied from the blades current displacement $D_n$ to its extrapolated value $D_{Ext,n}$. During the structural solver step, the blade displacement is corrected from the extrapolated value to the calculated value from equation (3.26). The step corrections are negligible in size once the blade's oscillation is well established over time. Figure 6.3 shows the time history of one performed FSI simulation showing the increase in accuracy of the extrapolation with time.

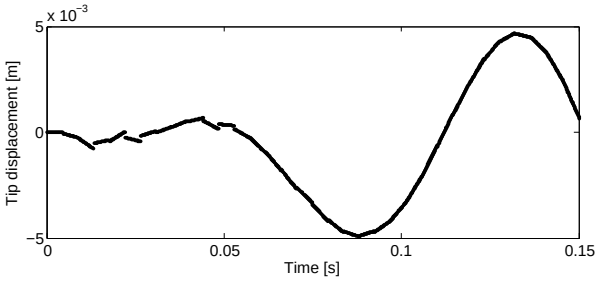


**Figure 6.3:** Extrapolation errors reduce over time as the blade motion becomes sinusoidal

## 6.3 Flow comparison with the mesh-based FSI simulation

In this section the mesh-based and meshless fluid models are compared to ensure that both predict similar flow physics. To begin with, the extracted aerodynamic loading is compared for an entire oscillation cycle as was done in section 5.3. Lastly, the separated flow regions are compared, as leading edge vortices are a major contributor to the aerodynamic loading at 9AOA.

### 6.3.1 Aerodynamic force comparison

Figure 6.4 compares the blade's aerodynamic loading extracted from the mesh-based and meshless FSI simulations for an entire oscillation cycle. The deviation between the two models is more significant at higher AOAs and inlet velocities. FPM predicts a lower force than the mesh-based simulation for the 0AOAV10, 9AOAV10 and 9AOAV15 simulations. This results in a higher estimation of the peak tip displacement as shown in table 6.1. On the other hand, FPM predicts a higher aerodynamic loading for the 9AOAV20 simulation and so estimates a lower peak tip displacement.

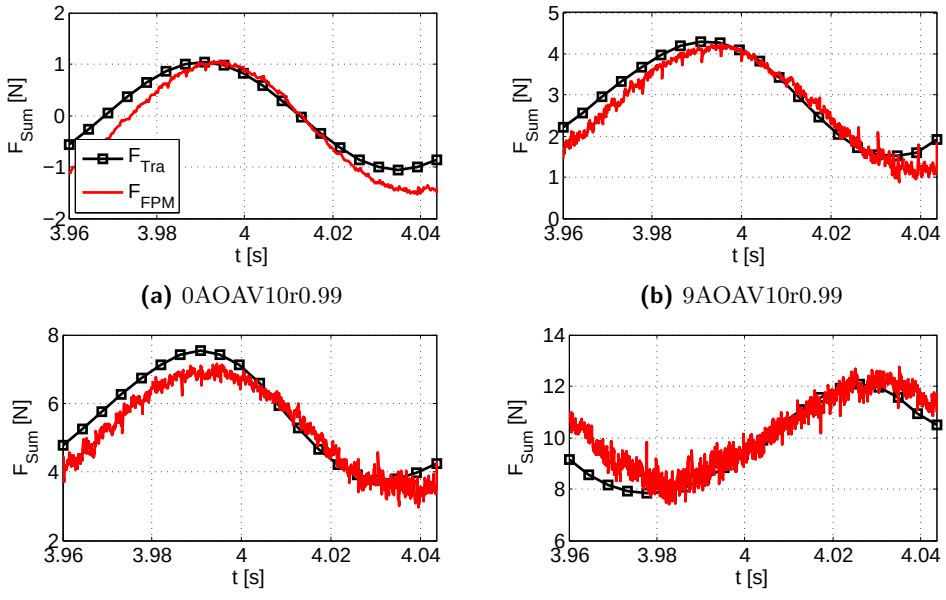


**(a)** 0AOAV10r0.99 **(b)** 9AOAV10r0.99

**(c)** 9AOAV15r0.99 **(d)** 9AOAV20r0.98

**Figure 6.4:** Comparison of the mesh-based and meshless predicted blade's total normal force over an entire oscillation cycle

As mentioned in section 6.2, the $k-\epsilon$ turbulence model has difficulties in predicting boundary layer separation and assumes fully turbulent flow. This causes inaccuracies that are especially evident at lower inlet velocities, as the flow is less turbulent. The deviation between the two models could also be attributed to the spatial resolution close to the blade. This is discussed in the following subsection.

The figures indicate a noticeable fluctuation of the predicted force using FPM. Fluctuations increase as the AOA and inlet velocity increase. Each numerical point, located on the blade surface, is assigned an area using local surface tessellation. The fine point cloud in FPM is still relatively coarse compared to the mesh used in the mesh-based FSI simulation. For that reason, the area assigned to each numerical point is relatively large and varies as points are added and removed. Fluctuations reduce as an even finer point cloud is used.

### 6.3.2 SFR comparison

Figure 6.5 shows the separated flow region, as predicted by FPM, over an entire oscillation cycle. Red and blue particles indicate a high and low circulation velocity respectively. A comparison with the mesh-based predicted SFR is discussed below:

- Both methods predict flow separation from the entire leading edge at instances $t_1$ to $t_3$. A discrepancy between the two methods occurs at $t_4$, because FPM predicts flow separation near the blade's tip. In section 4.4.1, it was argued that no flow separates near the blade tip at this instance, because the effective AOA is below the separation threshold.

- The vortex intensity is indicated in FPM using the circulation velocity. Strong LEVs are formed at instances $t_2$ and $t_3$ with weaker ones formed at $t_4$. An almost constant vortex strength is observed near the blade root. This corresponds to the mesh-based findings in section 4.4.1.

- The mesh-based method predicts a continuous separated flow region that covers most of the lower blade surface for all time instances. FPM on the other hand, predicts distinct vortex regions across the blade surface.

The inflation layer used in mesh-based methods is capable of fully resolving the separated flow region close to the blade surface. Very thin recirculation regions are therefore fully captured. The spatial refinement in FPM is limited to a relatively coarse resolution close to the blade. For this reason, only larger vortices are captured. This leads to the distinct representation of the SFR in figure 6.5.

The spatial refinement in FPM is limited by the computational cost. It increases significantly when using FPM instead of traditional mesh-based methods, because the time step size is limited by the CFL condition when using FPM. A further point cloud refinement close to the blade reduces the time step substantially. The relatively coarse discretization is a possible cause of the force deviations observed in figure 6.4.

Modelling LEVs accurately requires that they are fully resolved and that the flow separation point is accurately predicted. Therefore, a finer FPM resolution is required at a lower computational cost. Possible solutions to this issue are discussed in section 6.5.

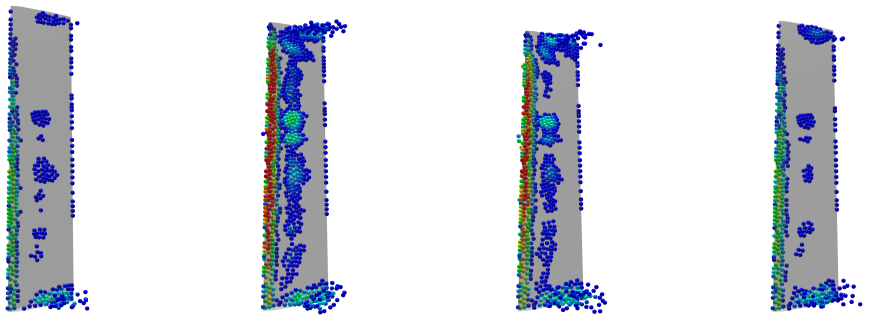

**(a)** Maximum $D_T$ at $t_1$ **(b)** Minimum $D_T$ at $t_2$, AFS **(c)** Maximum $D_T$ at $t_3$ **(d)** Minimum $D_T$ at $t_4$, WFS

**Figure 6.5:** The separated flow region development for 9AOAV10 using the meshless FSI simulation

## 6.4 FSI results

In this section the FSI simulation, using FPM and the Euler-Bernoulli beam model, is validated using the experimental data given in section 2.4. The transmissibility curves are compared in figure 6.6 for 0AOA and 9AOA.

Table 6.1 lists the relative deviations of the mesh-based FSI simulation using the SST transition model, the 1D beam model and the FSI simulation using FPM. All three models deviate significantly from the experimental results at 9AOAV15. The meshless and mesh-based methods have both been validated extensively and are capable of accurately predicting the tip displacement for the other five simulations. For that reason, experimental error at 9AOAV15 is plausible. Possible causes for experimental inaccuracies have been stated in section 4.3.1.

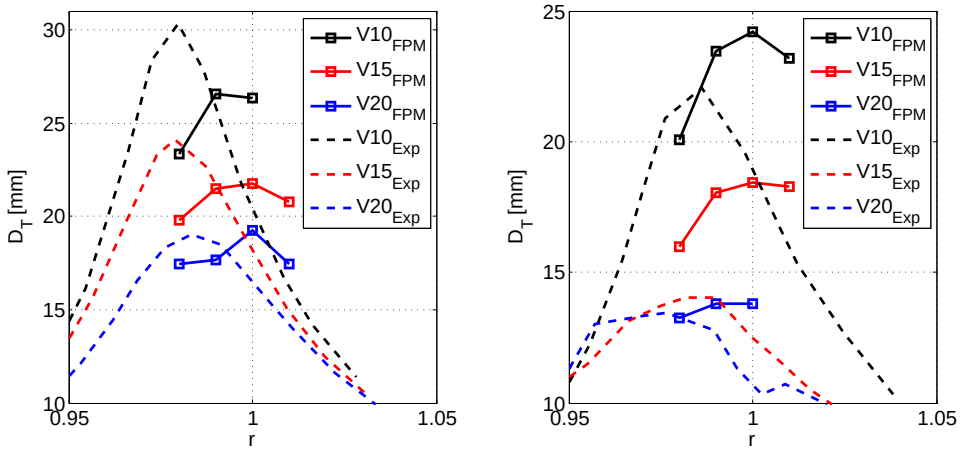


**(a)** 0AOA **(b)** 9AOA

**Figure 6.6:** Meshless FSI model validation for the two different geometric AOAs

All three methods predict similar results that vary by less than 8 % for each of the six simulations listed in table 6.1. The accuracy of the meshless FSI simulation can be improved by refining the point cloud near the blade surface to explicitly model the leading edge vortices and the flow in the boundary layer. Additionally, implementing the SST transition model in FPM can further improve the solution's accuracy.

**Table 6.1:** Relative deviatio (RD) comparison of the mesh-based $RD_{Tra}$, analytical $RD_{1D}$ and meshless $RD_{FPM}$ FSI simulations in computing the tip displacement. The deviation is relative to the experimental results

| $AOA$ | $V$ | $RD_{Tra}$ [%] | $RD_{1D}$ [%] | $RD_{FPM}$ [%] |
|---|---|---|---|---|
| 0 | 10 | -11.52 | **-10.43** | -12.41 |
| | 15 | **- 4.95** | - 6.86 | - 9.88 |
| | 20 | 4.13 | - 1.60 | **1.24** |
| 9 | 10 | **3.96** | 6.91 | 9.72 |
| | 15 | **27.31** | 29.23 | 31.14 |
| | 20 | 9.31 | 10.57 | **2.62** |

## 6.5 Suitability of meshless methods for simulating the aerodynamic damping of the ACC fan

FPM offers results that are comparable to those obtained by mesh-based methods. The relative deviation of predicting the peak tip displacements is less than 13 %, except for the experimentally flawed 9AOAV15 simulation.

In section 6.3, certain issues of FPM are mentioned. One of them is the computational expense. Each FPM simulation, using the fine point cloud, ran on average for 60 hours using 80 MPI processes on a cluster with dual Intel Xeon E5-2670 (2.6 GHz) processors. FPM has the advantage that the smoothing length can be altered in time and space as discussed in section 6.2. This reduces the simulation time, but it is still computationally more expensive than mesh-based methods. Additionally, the point cloud is not fine enough near the blade to fully resolve the leading edge vortices.

To alleviate these restrictions, an Eulerian method is currently being implemented into the in-house version of FPM (August, 2016). The method is based on (Kuhnert, 2001) and improved using the work of Seifarth (2014). FPM in the Eulerian description uses stationary numerical points to approximate the governing equations. Motion of numerical points is only required in the blade's vicinity. The CFL condition therefore allows a bigger time step as the points are not relocated with the fluid velocity, but at the lower blade velocity. This allows for a finer point cloud to resolve the vortices close to the blade while reducing the simulation's runtime significantly. Furthermore, the force fluctuations observed in figure 6.4 would reduce due to the finer point cloud. Employing the SST transition model, instead of the $k-\epsilon$ model, would in addition model transitional effects more accurately.

Remeshing and smoothing deteriorated mesh cells is a more complex task than adding or removing numerical points. Consequently, the FPM simulation is more robust than the mesh-based simulation. No numerical instabilities are observed for the meshless FSI simulation, although only a weak coupling scheme is used. Another reason for the method's robustness, is the small time stepping of the fluid solver.

To conclude, FPM is a viable alternative to mesh-based methods that offers similar results while circumventing its drawbacks. Therefore, it is suitable to model the fluid structure interaction occurring within the ACC fan unit. The computational cost is a limiting factor that can be alleviated by solving the governing equations in the Eulerian reference frame using FPM.

# Chapter 7

# Conclusion

## 7.1 Thesis objectives

The thesis objective was firstly to identify the major dynamic flow phenomena that affect the aerodynamic damping of the oscillating fan blade. These are listed below with their dependency on the fluid and structural variables stated:

**Leading edge vortex:** This is a dynamic flow phenomenon that occurs once the flow separates from the blade's leading edge to form a vortex. In its vicinity the pressure is lowered and thus the blade's lift force is amplified. Dynamic stall occurs once the vortex is shed from the blade. The formation of LEVs is dependent on the blade's effective AOA. If the effective AOA exceeds the separation threshold, a vortex is likely to form. Stronger vortices are formed at higher effective AOAs. Secondary vortices form due to vorticity being convected downstream from the LEV. They are constantly weakened by shedding circulating flow into the wake. For that reason, their size is roughly constant once the effective AOA does not vary above the separation threshold. The variation of the effective AOA depends on the blade's spanwise location.

**Tip vortices and downwash:** These are three-dimensional flow effects that occur at the blade tip. The fluid can freely flow from the blade's pressure side to its suction side. The pressure difference across the blade is reduced due to the circulating flow. The pressure loss is named downwash, whereas tip vortices are the circulating flow being convected into the wake. The pressure loss due to downwash is considerable and therefore modelled in the heuristic flow model. Downwash and tip vortices have a positive correlation with the geometric AOA, blade velocity and inlet velocity. Their influence on the blade's pressure distribution decreases as the distance to the blade tip increases.

**Added mass effect:** The blade is submerged in air and has to displace the fluid medium when vibrating. An inertial force is therefore exerted on the blade based on the added mass effect. This added mass leads to the observed shift in the blade's first bending frequency as discussed in section 2.5. As shown in section 5.2.3, the added mass increases with the inlet velocity at 9AOA, but decreases at 0AOA. Additionally, the added mass force positively correlates with the fluid density, blade surface area and the blade's acceleration.

The second objective of the thesis was to determine a suitable model for simulating the aerodynamic damping of the rotating fan in the ACC unit. Three different methods were analysed and their suitability determined based on their accuracy, robustness and computational cost. The methods are rated for each performance criteria as follows:

**Accuracy:** The predicted tip displacements, using the three models, vary by less than 8 % for all six simulations performed. The heuristic model requires an empirical factor to accurately model the lift induced by the leading edge vortices. It is therefore unsuitable for modelling the ACC fan unit as no experimental force measurements are available. The mesh-based method can resolve finer flow effects close to the blade, because the smoothing length of the particle cloud in FPM is limited due to the enormous computational cost. Additionally, the SST transition model is used in the mesh-based method whereas only the $k-\epsilon$ turbulence model is implemented in FPM. This allows for a more accurate representation of transitional effects occurring in the boundary layer.

No evidence was found to support the sudden drop in tip displacement at 9AOAV15. The three numerical FSI models predict a noticeably higher tip displacement for this simulation. For that reason, experimental errors are expected. A plausible assumption is given in section 4.3.1.

**Robustness:** Numerical stability is achieved in the mesh-based simulation by remeshing and smoothing operations. Mesh motion can cause severe numerical instabilities or inaccuracies. FPM ensures a well distributed point cloud by adding or removing points that violate equation (6.6). This is a less complex procedure as no rigid node interconnectivity has to be constructed. Additionally, the smaller time step taken in FPM ensures a more rigid simulation. The simplified 1D beam model is also very robust, because an inner iterative loop is used as discussed in section 5.1.

**Computational cost:** The least and most expensive models are the simplified 1D beam model and the meshless FSI simulation respectively. FPM is significantly more expensive than the mesh-based method due to the CFL condition restricting the time step size. As mentioned in section 6.5, this restriction can be alleviated by using the Eulerian description of FPM. Point motion is then only necessary in the blade's vicinity. Furthermore, the points move at blade velocity, which is lower than the inlet velocity. This reduces the numerical cost significantly.

To conclude, the simplified 1D beam model is unable to model the force exerted by the formed vortices accurately without an empirical factor. Therefore it is not advised to simulate the ACC fan unit.

The mesh-based and meshless methods are both suitable solutions for modelling the rotating and oscillating fan in the ACC unit. The major drawback of mesh-based methods is mesh deformation in the fluid domain. To minimise the possibility of mesh deterioration, smaller time steps, more intensive remeshing procedures or a moving mesh inside a sliding domain are plausible solutions. The latter option is used in Hsu and Bazilevs (2012). One drawback of FPM is the high computational cost relative to the coarse spatial discretization. As previously mentioned, this problem is eliminated when using the Eulerian description. Numerical stability is vital whereas simulation runtime can simply be reduced by using more MPI processes. Therefore, using FPM for simulating the fluid is advised when modelling the ACC fan unit.

## 7.2 Future work

This thesis covers the numerical foundation for modelling the aerodynamic damping of the rotating fan in the ACC unit. Either the mesh-based or meshless FSI simulation can be adapted to model this phenomenon, but the meshless method is advised.

The folowing steps are set out towards simulating the aerodynamic damping of the rotating fan in the ACC fan unit:

- Ideally, the Eulerian formulation of FPM should be used. Additionally, the SST transition model should be incorporated into FPM.
- Centrifugal forces lead to blade stiffening that alters the blade's natural frequency. Torsional modes may also play a role in blade motion as Muiyser *et al.* (2014) mentioned vibrational peaks at different frequencies- The dominant one being at the blade's first bending frequency. A two-dimensional shell model of the fan might be sufficient to capture these effects.
- As mentioned by Muiyser (2016), the fan is mounted to a fan bridge whose vertical motion at its centre causes additional fan vibrations and should therefore be incorporated in the full scale structural model. Additionally, the structural load and vibration caused by the motor and gearbox should be modelled.
- A fluid model should be created that encompasses the axial fan, its housing and the fan bridge to which it is mounted. Furthermore, the finned tube bundles should be modelled directly or as a porous medium.

# Appendix A

# Blade profile and geometry

The axial fan blade profile is manufactured according to the dimensions given in Riegels (1961) for a flat plate profile. The lift and drag coefficients of the axial fan blade are comparable to those given by Riegels in figure 2.3.

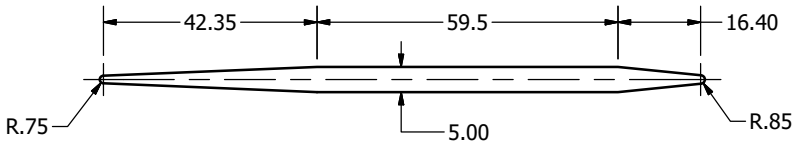


**Figure A.1:** Flat plate profile

The dimensions of the structural blade model are given in figure A.2. The top part of the aluminium blade with spanwise length 560 mm is situated within the fluid simulation domain and the bottom part of the axial fan blade is excluded.

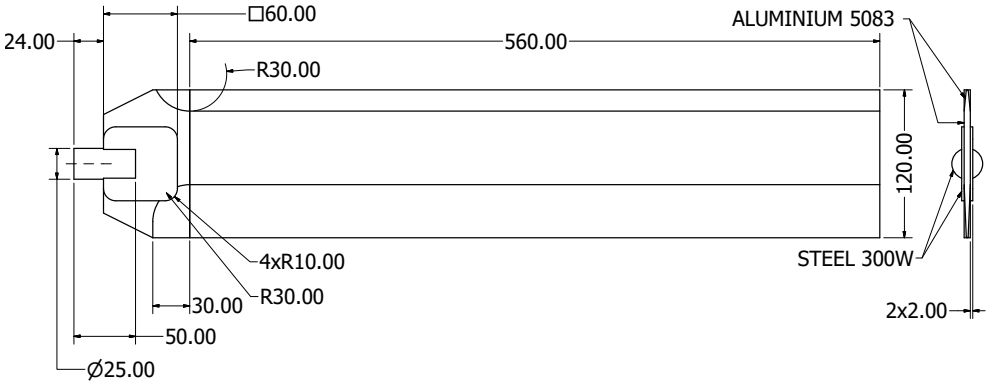


**Figure A.2:** Axial fan blade geometry

# Appendix B

# Additional information for the mathematical and numerical model

## B.1 Fluid flow assumptions

The physical phenomena have to be captured by a mathematical model. To do this certain fluid assumptions have to be made. These are listed below:

**Continuum principle:** Gases such as air have widely spread molecules that have weaker attraction forces than those in solids. This means that they can easily move irregularly and relative to each other. Using the continuum principle, the gaps between the molecules are disregarded and the fluid is considered continuous (Cengel and Cimbala, 2010). This allows for a mathematical approximation to describe the macroscopic fluid motion and assign attributes to it such as density, viscosity and pressure (Gatzhammer, 2008).

The fluid element consists of several fluid molecules and their properties are averaged to give the properties of the fluid element. This allows for the description of fluid state using its position and time (Gatzhammer, 2008).

**Newtonian and Isotropic:** Air can be modelled as a Newtonian fluid, because the shear stress ($\tau$) arising in the fluid element is linearly proportional to its strain rate ($\frac{du}{dy}$) as shown for one-dimensional flow in equation (B.1). The constant of proportionality is called the fluid viscosity ($\mu$) (Cengel and Cimbala, 2010).

$$\tau = \mu \frac{du}{dy} \tag{B.1}$$

The fluid is also isotropic. The fluid's properties are independent of the direction along which they are measured.

**Constant temperature:** Temperature changes are not considered in the simulation of the experiment. The temperature will be assumed constant throughout each simulation. This is a valid assumption, because the inlet air is not externally heated and temperature fluctuations are negligible. This means that the fluid properties such as viscosity $\mu$ and density $\rho$ are temperature independent. The benefit of this assumption is that no additional energy equation has to be solved.

**Incompressible:** Cengel and Ghajar (2011) state that if the Mach number of the fluid is below 0.3, then the fluid can be assumed to be incompressible. An incompressible fluid is assumed to have a constant density. The maximum Mach number is the ratio of the maximum air velocity in the domain divided by the speed of sound. Equation (B.2) is used to calculate the speed of sound using the fluid properties given in chapter 2 with the assumption that air is an ideal gas (Nave, 2015).

$$C_{Air} = \sqrt{\frac{c_P}{c_V} \times R_{Air} T} \tag{B.2}$$

The ratio of the specific heats of air $c_p/c_v$ is 1.4 at room temperature. The gas constant of air is 287 J/(kgK). The air temperature $T$ at the wind tunnel inlet was measured to be 298.15 K (Basson, 2015). This gives a speed of sound of 346.117 m/s. The air velocity may therefore not supersede 103.835 m/s in the simulation to be assumed incompressible. This gives a sufficient variance from the maximum inlet velocity of 20.335 m/s. The validity of this assumption will be verified during the simulations and reconsidered if the fluid velocity anywhere in the domain is greater than the specified value.

## B.2 Matrices for the structural model

### B.2.1 Mass matrix

The continuous mass distribution of the structure is discretized and represented by the mass matrix. In this subsection three different methods will be discussed to set up the mass matrix: the lumped, consistent and combined approach. The consistent method is used for the 1D model and leads to more accurate solutions if an implicit method is used (Cook *et al.*, 2002). Particle mass lumping is used in ANSYS for mesh-based methods (ANSYS Inc., 2013*d*, p. 1794).

**Particle mass lumping:** The element mass is lumped in equal parts onto each node. This gives a discontinuous displacement field where the nodes move separately to each other (Cook *et al.*, 2002). There is no mass linkage between the nodes, because the mass matrix is diagonal. Mass lumping is computationally efficient, but no rotational inertia is present and it has to be artificially added for rotational DOF. Furthermore, it can lead to ill-conditioned matrices for elements containing rotational DOF. This is of no concern for displacement based elements (Cook *et al.*, 2002).

For a two node displacement element in three-dimensional space, the mass matrix is given by:

$$\boldsymbol{M}_{Loc} = \frac{\rho V}{2} \boldsymbol{I} \tag{B.3}$$

where $\boldsymbol{I}$ is the $6 \times 6$ identity matrix. Newton's second law can be written as:

$$\boldsymbol{M}_{Loc} \left\{ \ddot{D}_{x,1}, \ddot{D}_{y,1}, \ddot{D}_{z,1}, \ddot{D}_{x,2}, \ddot{D}_{x,2}, \ddot{D}_{x,2} \right\}^T = \sum F \tag{B.4}$$

$D_x, D_y, D_z$ are the spatial displacements and subscripts 1 and 2 mark the two different nodes.

**Consistent mass matrix:** This method uses the same shape functions as those used for the stiffness matrix in FEM (Alavala, 2008). The local mass matrix of each element is determined by:

$$\boldsymbol{M}_{Loc} = \int_V \rho \left[\boldsymbol{N}^T\right] [\boldsymbol{N}] \, dV \tag{B.5}$$

where $\rho$ is the material density and $\boldsymbol{N}$ is the shape function matrix.

**Combined matrices:** This method combines the lumped and consistent method into one:

$$\boldsymbol{M}_{Loc} = \beta \boldsymbol{M}_{Loc,Cons} + (1 - \beta) \, \boldsymbol{M}_{Loc,Lum} \tag{B.6}$$

with $0 < \beta < 1$. Cook *et al.* (2002) shows that for several problems the lumped and consistent mass matrix underestimate and overestimate the natural frequencies respectively. Therefore, a combined mass matrix can lead to more accurate results.

### B.2.2 Damping matrix

Damping dissipates energy and reduces the amplitude of the vibration as shown by the SDOF system. The easiest way to set up the dynamic equation is by modelling all damping forces as viscous, as shown in equation (3.20). According to Cook *et al.* (2002) this is an accurate representation if the damping force $\boldsymbol{C}\dot{\boldsymbol{D}}$ does not exceed 10 % of the other forces in equation (3.20).

Rayleigh damping is an efficient way of representing the damping matrix. It allows for the coupled equation (3.20) to be uncoupled into $j$ independent equations using orthogonal transformation, where $j$ is the number of DOF (Chowdhury and Dasgupta, 2003). Here the damping matrix is a linear combination of the mass and stiffness matrix (Cook *et al.*, 2002):

$$\boldsymbol{C} = \beta_1 \boldsymbol{M} + \beta_2 \boldsymbol{K} \tag{B.7}$$

It is difficult to guess values for the constants $\beta_1$ and $\beta_2$. Chowdhury and Dasgupta (2003) give an equation that relates frequency and its corresponding damping coefficient to the constants:

$$\zeta = \frac{\beta_1}{2\,\omega} + \frac{\beta_2 \, \omega}{2} \tag{B.8}$$

The equation shows that $\beta_1 \boldsymbol{M}$ and $\beta_2 \boldsymbol{K}$ damp significantly for low and high frequencies respectively.

The blade's tip decay was recorded by Basson (2015) in a vacuum chamber to determine the blade's purely structural damping. The structural damping will be represented by the $\beta_1$ component and $\beta_2$ will be excluded under vacuum conditions. As mentioned in section 3.3.2.2, numerical damping is employed to prevent high frequency numerical noise. Therefore, $\beta_2$ is set to zero as the blade's higher frequency modes are already damped.

By substituting $\zeta_V$ and $\omega_V$ from table 2.1 into equation (B.8), $\beta_1$ is determined to be approximately 0.19. This damping factor will be included in all FSI simulations to model the structural damping.

### B.2.3 General stiffness matrix derivation

The stress-strain relationship in a material is given by Hooke's law as:

$$\boldsymbol{\sigma} = \boldsymbol{E}\boldsymbol{\epsilon} \tag{B.9}$$

There are a total of nine stress components acting on a point in a solid of which only six are independent to satisfy the force and moment equilibrium (Liu and Gu, 2005). The stress vector is given by:

$$\boldsymbol{\sigma}^T = \{\sigma_{XX}\, \sigma_{YY}\, \sigma_{ZZ}\, \sigma_{YZ}\, \sigma_{XZ}\, \sigma_{XY}\} \tag{B.10}$$

where the first three stresses are normal stresses and the other three are shear stresses. The constitutive matrix $\boldsymbol{E}$ relates the stress vector to the strain vector $\boldsymbol{\epsilon}$ and is given for an isotropic, three-dimensional solid as (Liu and Gu, 2005):

$$\boldsymbol{E} = \begin{bmatrix} D_{11} & D_{12} & D_{12} & 0 & 0 & 0 \\ & D_{11} & D_{12} & 0 & 0 & 0 \\ & & D_{11} & 0 & 0 & 0 \\ & & & G & 0 & 0 \\ & sy. & & & G & 0 \\ & & & & & G \end{bmatrix} \tag{B.11}$$

where

$$D_{11} = \frac{E(1-v)}{(1-2v)(1+v)} \quad D_{12} = \frac{Ev}{(1-2v)(1+v)} \tag{B.12}$$

and $G$ is the shear modulus. $G$ is dependent on the Young's modulus $E$ and Poisson's ratio $v$:

$$G = \frac{E}{2(1+v)} \tag{B.13}$$

The relationship between strain and nodal DOF is given by Cook *et al.* (2002):

$$\boldsymbol{\epsilon} = \boldsymbol{B}\boldsymbol{D}_{Loc} = \begin{bmatrix} \frac{\partial}{\partial x} & 0 & 0 \\ 0 & \frac{\partial}{\partial y} & 0 \\ 0 & 0 & \frac{\partial}{\partial z} \\ \frac{\partial}{\partial y} & \frac{\partial}{\partial x} & 0 \\ 0 & \frac{\partial}{\partial z} & \frac{\partial}{\partial y} \\ \frac{\partial}{\partial z} & 0 & \frac{\partial}{\partial x} \end{bmatrix} \boldsymbol{N}\boldsymbol{D}_{Loc} \tag{B.14}$$

where $\boldsymbol{B}$ is called the strain-displacement matrix. Shape functions $\boldsymbol{N}$ are discussed in greater detail in Cook *et al.* (2002). In general, field quantities are known at the nodal locations, but elsewhere they are usually approximated using an interpolating polynomial. These are then used to cast the shape functions, which are the individual $N_i$ in $\boldsymbol{N}$.

Using the principle of virtual work, the element stiffness matrix $\boldsymbol{K}_{Loc}$ can be found using equation (B.15) and cast into the global stiffness matrix $\boldsymbol{K}$ as done in Cook *et al.* (2002).

$$\boldsymbol{K}_{Loc} = \int \boldsymbol{B}^T \boldsymbol{E} \boldsymbol{B} dV \tag{B.15}$$

#### B.2.3.1 Stiffness matrix for 1D beam element

According to Harrevelt (2012) the Euler-Bernoulli beam theory is used for slender beams, such as the fan blade, which means that the transverse shear deformation is ignored (Cook *et al.*, 2002).

A 1D beam element is shown in figure 5.2. It has two nodes on either side. Each node has one rotational DOF about the x-axis and a displacement DOF in the y-direction. Axial displacements will be ignored as only the blade's flapwise motion has to be captured to accurately predict its first bending mode.

Equation (B.15) can be used to derive $\boldsymbol{K}_{Loc}$ and is given as:

$$\boldsymbol{K}_{Loc}\boldsymbol{D}_{Loc} = \frac{EI}{L^3} \begin{bmatrix} 12 & 6L & -12 & 6L \\ 6L & 4L^2 & -6L & 2L^2 \\ -12 & -6L & 12 & -6L \\ 6L & 2L^2 & -6L & 4L^2 \end{bmatrix} \begin{bmatrix} v_1 \\ \theta_1 \\ v_2 \\ \theta_2 \end{bmatrix} \tag{B.16}$$

where $I$ is the area moment of inertia.

# Appendix C

# Structural model set-up

This appendix covers additional information for section 4.1.

## C.1 Structural meshing procedure

Originally the blade was split into the steel base and aluminium blade, but due to geometrical complexities, an unstructured tetrahedral mesh had to be created. A structured hexahedral mesh was created by further splitting the blade model into smaller parts. This was done to reduce the total number of cells and to increase the cell quality. The separate meshing blocks are shown in figure C.1. Hexahedral meshing was enforced in the meshing blocks of the aluminium blade and in the steel plates. The created meshes from the different meshing blocks are not necessarily conforming at their interface. This is not a requirement, because the meshes were mathematically bonded together at their interfaces using a multi-point-constraint (MPC). A MPC does not allow for separation of the contact surfaces (ANSYS Inc., 2013*d*, p. 505). Table C.1 lists the meshing steps for the coarse, medium and fine mesh.

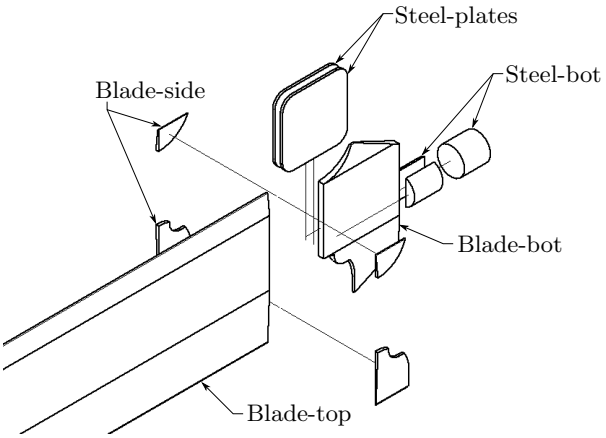


**Figure C.1:** Explosion view of the separate meshing blocks

Section 3.3.2.2 mentions that numerical damping is required for displacement boundary conditions and other phenomena such as numerical diffusion. In the validation cases, the base of the blade is fully constrained and no remeshing is required as the fluid domain is excluded. Therefore, no numerical damping is required for these instances.

**Table C.1:** Meshing procedure

| | Mesh block | Coarse | Medium | Fine |
|---|---|---|---|---|
| Body sizing $[mm]$ | Steel-plates | 3.5 | 3 | 2.5 |
| | Steel-bot | 6.5 | 6 | 5.5 |
| | Blade-top | 5.5 | 5 | 4.5 |
| | Blade-bot | 6.5 | 6 | 5.5 |
| | Blade-side | 3 | 2.5 | 2 |

The transient decay simulation was performed using $\beta_1 = 0.19$ as theoretically determined in appendix B.2.2. An exponential trend line was fitted through the peak values of the simulation results as shown in figure C.2 to determine $\zeta$ by comparing it to the exponential term of the SDOF homogeneous solution stated in equation (3.18):

$$e^{-\omega_d \zeta t} = e^{-0.09621t} \quad \text{thus} \quad \zeta = \frac{0.09621}{\omega_d} \tag{C.1}$$

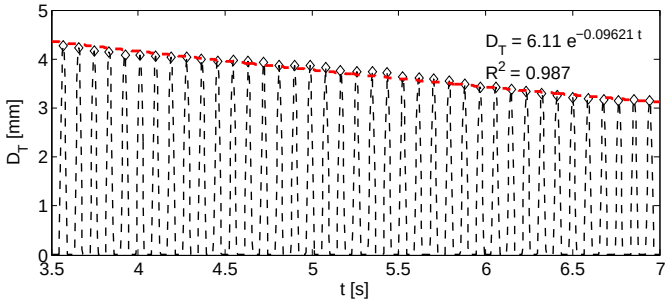


**Figure C.2:** Determining $\zeta$ from the transient decay simulation

## C.2 Mesh quality

The aspect ratio (AR), orthogonal quality (OQ) and element quality (EQ) will be used to compare the quality of the three different meshes. According to Brandsen (2013), a mesh growth rate of 20 % is acceptable and was set as the maximum growth rate for all meshes. Furthermore, he states that an AR below 10 000 is good, which is achieved by all three meshes.

EQ ranges between 0 and 1, where 0 indicates a negative cell volume, which can lead to a diverging simulation (ANSYS Inc., 2013*e*). Figure C.3 compares the EQ of the three different meshes and shows their bad to excellent cells as a percentage of the total number of cells. None of the three meshes contain bad or poor cells, which make them acceptable for the FSI simulation.

Skew cells are unacceptable and can lead to numerical errors. OQ is a measure of element quality ranging from 0 to 1, where 0 indicates very skew

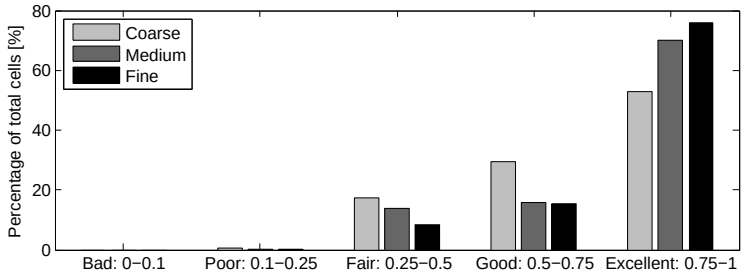


**Figure C.3:** EQ of the structural meshes

cells. Figure C.4 compares the OQ of the three different meshes and shows their bad to excellent cells as a percentage of the total number of cells. The figure shows that no bad or poor cells are contained in the three different meshes. Thus, the coarse mesh will be used for the FSI simulation as it is mesh independent, computationally inexpensive and has a good mesh quality.

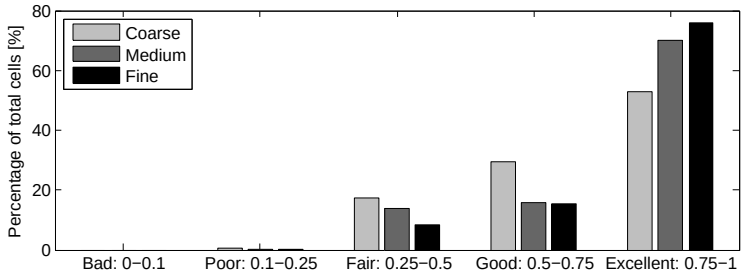


**Figure C.4:** OQ of the structural meshes

## C.3 Structural model adjustments for the FSI simulation

The adjustments made for the FSI simulation are as follows:

**Base excitation:** Section 2.4.1 states the required base constraints for the FSI simulation.

**FSI interface:** The blade surface submerged in the fluid requires an FSI interface so that data between the fluid and structural domain can be exchanged.

**Numerical damping:** The base of the blade is no longer fully constrained and thus numerical damping is required as mentioned in section 3.3.2.2.

# Appendix D

# Fluid model set-up

This appendix covers additional information for section 4.2.

## D.1 Fluid meshing procedure

Three different meshing approaches were attempted of which only the last prevailed:

**Polyhedra meshing:** A completely unstructured mesh was created around the blade with an inflation layer on the blade surface. The unstructured tetrahedral mesh was then converted to a polyhedra mesh in Fluent. A polyhedra mesh has the advantage that it reduces the total amount of cells and thus fastens the simulation process, although the computational cost per cell is increased, because each cell has more faces. This method does not work for FSI, because ANSYS does not allow for system coupling with a polyhedral mesh.

**Structured mesh around the blade:** The next meshing attempt was to create a structured mesh around the blade and an unstructured mesh in the rest of the domain. This ensured a high mesh quality around the blade. The problem was that no inflation layer could be created around the blade if the surrounding mesh was structured. This meant that there was no inflation layer that could deform with the blade and thus the blade adjacent cells changed in cell height. Therefore, the $y^+$ value constantly changed, which is not optimal.

**Unstructured mesh around the blade:** The final meshing attempt consisted of leaving the mesh around the blade unstructured and creating a structured mesh elsewhere in the computational domain. This allowed for the creation of a fine inflation layer around the blade, to capture boundary layer effects, that could deform with the blade. The structured meshing elsewhere in the domain reduced the total number of cells significantly. Figure D.1 shows the mesh around the blade for clarity.

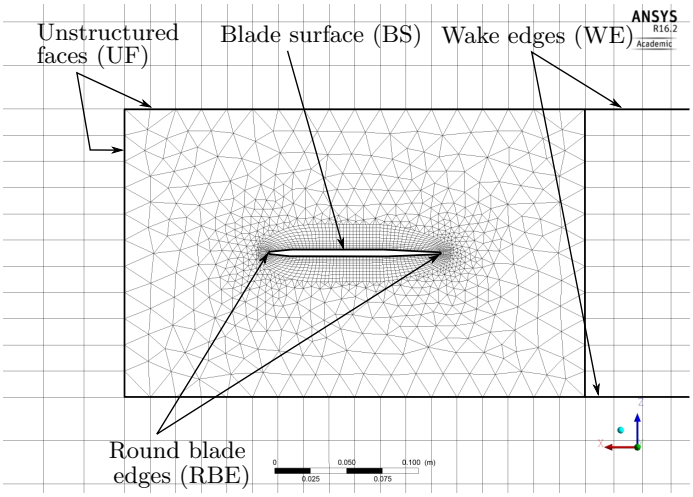


**Figure D.1:** Unstructured mesh around the blade for the SST $k-\omega$ model

### D.1.1 SST $k-\omega$ model

Four different meshes were compared to ensure mesh independence. Table D.1 states the different mesh refinements with the different meshing locations indicated in figure D.1. The growth rate was set to 20 % for the coarse to fine mesh and set to 15 % for the very fine mesh. A mapped face meshing was ensured on the blade surface so that the cells in the inflation layer were structured. A multizone method was used to create a structured hexahedral in the wake and surrounding fluid volume. The first layer thickness of the inflation layer was chosen so that the $y^+$ value was roughly 30 or smaller. As mentioned in section D.3, using enhanced wall treatment ensures $y^+$ insensitivity. The coarse to fine mesh have a first layer inflation layer thickness of 0.8 mm and the very fine mesh has a thickness of 0.7 mm. The growth rate of the inflation layer was set to 20 % and reduced to 15 % for the very fine mesh. Mesh smoothing was performed in Fluent to improve cell quality of the worst 1 % mesh cells.

**Table D.1:** Meshing procedure for the turbulent simulation

| | Mesh block | Coarse | Medium | Fine | Very fine |
|---|---|---|---|---|---|
| Cell count | | 616055 | 914871 | 1231066 | 1778581 |
| Face sizing [$mm$] | UF | 22 | 20 | 18 | 14 |
| | BS | 3.5 | 3 | 2.5 | 2.5 |
| Edge sizing [$mm$] | RBE | 1.1 | 1 | 0.9 | 0.9 |
| | WE | 25 | 22.5 | 20 | 20 |
| Inflation layers | BS | 10 | 10 | 10 | 15 |

Figure D.2 compares the predicted lift and drag coefficients for the different meshes. A second order polynomial was fitted to the data. The coefficients for the quadratic and linear terms were very small, indicating that a mesh refinement did not alter the solution.

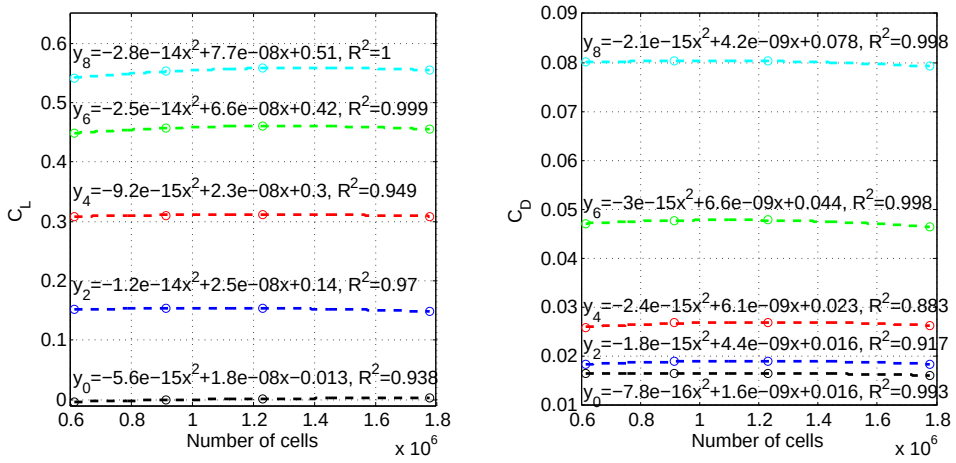


**(a)** $C_L$ vs. number of mesh cells **(b)** $C_D$ vs. number of mesh cells

**Figure D.2:** $k-\omega$ SST Turbulence Model

The domain size was increased, as stated in table 2.3, to ensure that the domain boundaries were placed far enough from the blade not to influence the accuracy of the solution. The maximum deviation between the predicted $C_L$ and $C_D$ values for the two domains are 2.4 % and 0.98 % respectively. The difference is negligible and thus the smaller domain will be used for the FSI simulation to reduce the computational cost.

### D.1.2 Transition model

Three different meshes were created according to table D.2. The growth rate was set to 20 % for all meshes. A mapped face meshing was ensured on the blade surface so that the cells in the inflation layer were structured. A multizone method was used to create a structured hexahedral mesh in the wake and surrounding fluid volume. The first layer thickness of the inflation layer was chosen so that the $y^+$ value was below 1 as required by the SST transition model. This corresponds to a first layer inflation layer thickness of 0.048 mm. The growth rate of the inflation layer was set to 10 %, which is another requirement of the SST transition model (ANSYS Inc., 2013*b*). Mesh smoothing was performed in Fluent to improve cell quality of the worst 1 % mesh cells.

**Table D.2:** Meshing procedure for the transient simulation

| | Mesh block | Coarse | Medium | Fine |
|---|---|---|---|---|
| Cell count | | 1175405 | 2130182 | 3042533 |
| Face sizing [$mm$] | UF | 22 | 20 | 18 |
| | BS | 3 | 2.5 | 2 |
| Edge sizing [$mm$] | RBS | 0.9 | 0.8 | 0.7 |
| | WE | 25 | 22.5 | 20 |
| Inflation layers | BS | 20 | 20 | 20 |

From figure D.3 it can be seen that the fitted trendline has small coefficients for the quadratic and linear term, which ensures mesh independence.

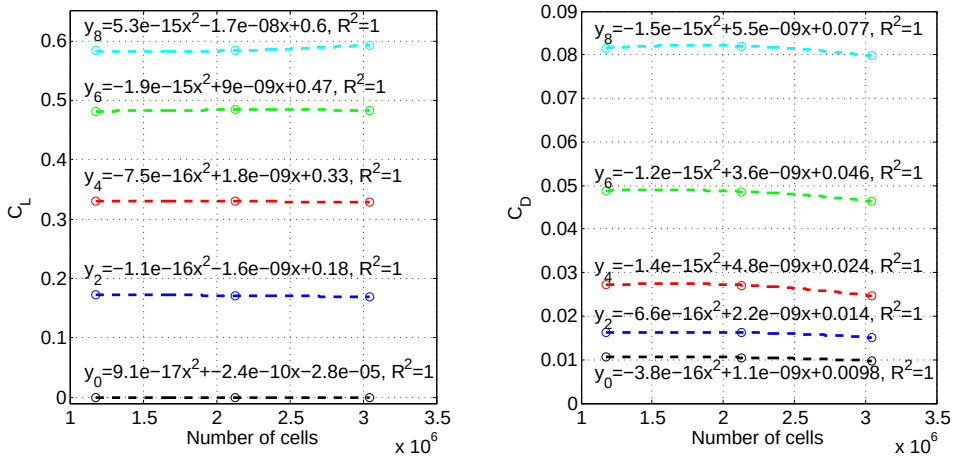


**(a)** $C_L$ vs. number of mesh cells **(b)** $C_D$ vs. number of mesh cells

**Figure D.3:** SST Transition Model

## D.2 Mesh quality

The mesh quality guidelines mentioned in section C.2 also apply to the fluid simulation mesh. The maximum AR of the transient and turbulent simulation mesh is 361.2, which is acceptable.
The fluid mesh contains more cells with a lower EQ than the structural mesh, because of the increased AR. Cells with a higher AR are more susceptible to form negative cell volumes during the mesh update process. Figure D.4 shows the EQ distribution for the turbulent and transition mesh respectively. The bad and poor EQ cells are located within the inflation layer, which is set to deform with the blade and thus little or no remeshing occurs in the inflation layer. This prohibits the generation of negative cell volumes. Therefore the simulation is not likely to diverge due to the bad EQ cells.

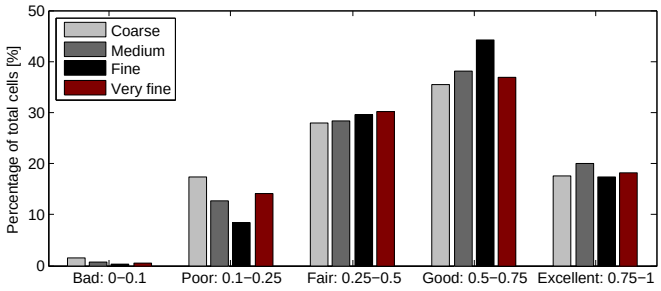


**(a)** EQ of the $k-\omega$ SST turbulent model mesh

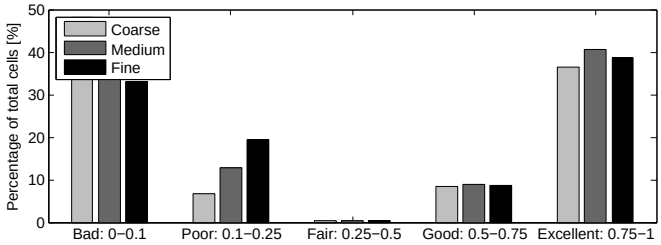


**(b)** EQ of the SST transition model mesh

**Figure D.4:** EQ of the fluid meshes

OQ of the mesh cells is given in figure D.5. The turbulence simulation mesh does not contain cells with a bad OQ, indicating that no skew cells reduce the accuracy of the simulation. The coarse transition simulation mesh contains 2 % cells with a poor OQ. These are located near the edges of the blade. Their influence on the simulation accuracy is negligible as the coarse mesh predicts the same lift and drag coefficients as the medium and fine meshes with no bad or poor OQ cells.

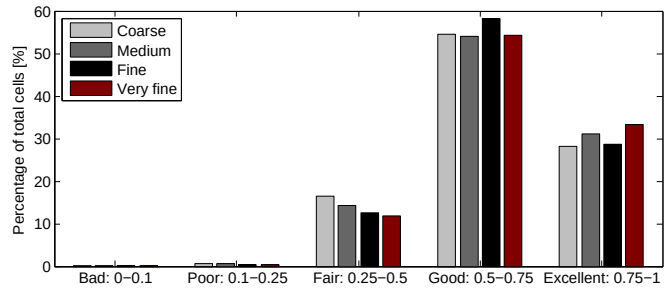


**(a)** OQ of the $k-\omega$ SST turbulent model mesh

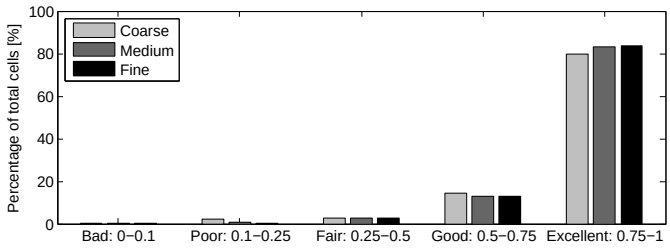


**(b)** OQ of the SST transition model mesh

**Figure D.5:** OQ of the fluid meshes

## D.3 Enhanced wall treatment

Turbulent flow can be characterised by four different regions (Cengel and Cimbala, 2010):

**Viscous sublayer:** A very thin layer next to the wall where viscous effects dominate turbulent effects and the flow is nearly laminar, because the wall minimises eddy motion.

**Buffer layer:** This is the next region where turbulent effects increase, but viscous effects are still dominant.

**Transition layer:** Above the buffer layer is the transition layer where turbulent effects are significant, but viscous effects are still dominant.

**Turbulent layer:** This region is furthest away from the wall and describes the remaining part of the flow. Here, turbulent effects dominate.

Due to the different flow characteristics in each layer, it is difficult to find an analytical velocity profile. The velocity profile in the viscous sublayer can be described using the normalised law of the wall (Cengel and Cimbala, 2010):

$$u^+ = y^+ \quad \text{if} \quad 0 < y^+ < 5 \tag{D.1}$$

where $y^+$ is similar to the Reynolds number, using half of the first cell height $y$ as characteristic length:

$$y^+ = \frac{yu^*\rho}{\mu} \tag{D.2}$$

$u^*$ is the frictional velocity $\sqrt{\tau_w/\rho}$ and is also used in $u^+$:

$$u^+ = \frac{u}{u^*} \tag{D.3}$$

where $u$ is the flow velocity close to the wall. In the transition layer the flow can be described using the logarithmic law:

$$u^+ = A_1\, ln\left(y^+\right) + A_2 \quad \text{if } y^+ > 30 \tag{D.4}$$

$A_1$ and $A_2$ are constants that can be determined experimentally. Equation (D.1) and equation (D.4) are not applicable in the buffer layer as shown in figure D.6. The use of standard wall functions in ANSYS requires that $y^+ > 30$ on the entire surface of the structure (ANSYS Inc., 2013*b*). The buffer and viscous layer are not resolved using the mesh, but are rather represented by an empirical expression. The Transition SST model requires that $y^+ \approx 1$, which means that all layers are resolved using the mesh.

Enhanced wall treatment ensures insensitivity to the $y^+$ value and allows for more freedom during mesh refinement. If $y^+ \approx 1$ the low Reynolds approach is used whereas if $y^+ > 30$ the wall functions are used. To ensure accuracy for meshes in the intermediate region between $5 < y^+ < 30$, the enhanced wall treatment smoothly blends the law of the wall and the logarithmic law using a smoothing function (ANSYS Inc., 2013*a*).

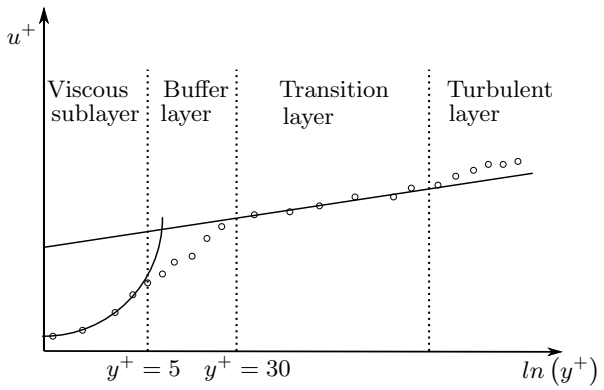


**Figure D.6:** Subdivisions of near-wall regions

## D.4 Fluent solver set-up

A steady flow analysis was conducted to validate the CFD simulation. The choices for the viscous model are mentioned in section 4.2.1.1. Table 2.2 states the fluid properties and the inlet velocity. The inlet and outlet turbulence intensity and viscosity ratio are not altered from the default values of 5 % and 10 respectively, as they were not measured by Basson (2015). This assumption was validated in appendix E.1. The other boundary conditions are shown in figure 2.5.

Shengyi *et al.* (2010) uses the SIMPLE algorithm for the velocity-pressure coupling whereas ANSYS Inc. (2013*b*) suggests the use of the PISO algorithm for transient simulations. It is mentioned that the algorithm converges rapidly and is stable even at large time steps, but has no noticeable advantage over the SIMPLE or SIMPLEC algorithm for steady state simulations. During the CFD validation process, the PISO algorithm sometimes caused the simulation to diverge and therefore the SIMPLEC scheme was employed. According to ANSYS Inc. (2013*b*), SIMPLEC converges faster than the SIMPLE algorithm. The spatial discretization of the convection terms for all transport equations was chosen as second order upwind as was done by Shengyi *et al.* (2010). A first order implicit time stepping scheme was employed.

## D.5 Fluid model adjustments for the FSI simulation

The adjustments made for a FSI simulation are as follows:

**Transient simulation:** The Fluent solver was set to transient with a time step size of 0.0044 sec. The solution is time step size independent as shown in section 3.3.2.

**Dynamic mesh:** The blade surface is set to be a FSI interface so that information can be transferred between the structural and fluid solver. The inflation layer is set to move with the FSI interface to ensure that the $y^+$ criterion is always met. The cells in the fluid domain and at the bottom symmetry face are set to deforming. This allows for cell smoothing and remeshing, which is covered in greater detail in the following section. Implicit mesh updating ensures that the mesh is updated during each time step. This is recommended for FSI simulations (ANSYS Inc., 2013*b*) and ensures a more robust solver run.

### D.5.1 Mesh update process

During blade motion, the fluid mesh has to adjust to the moving FSI interface. To prevent the deterioration of the mesh quality during the mesh update process, cell smoothing and remeshing are activated.

If the boundary is deformed and the interconnectivity of the nodes is not changed, then smoothing allows the absorption of the boundary motion by adjusting the cell size. Spring based smoothing is generally used for tetrahedral cells (ANSYS Inc., 2013*b*). It is cost efficient, but diffusion based smoothing is recommended for complex boundary motion if non-tetrahedral cells are used. Cell smoothing and remeshing will be mostly required in the unstructured mesh around the blade thus spring based smoothing is applicable here.

The edges between cell nodes are seen as ideal springs. The displacement of a boundary node induces a force along all the springs connected to it. The force is proportional to the node displacement according to Hook's Law. The interior nodes are iteratively shifted until a new equilibrium position of the nodes is achieved (ANSYS Inc., 2013*b*). Figure D.7 shows the smoothing of cells adjacent to the inflation layers an oscillating cylinder at different time steps.

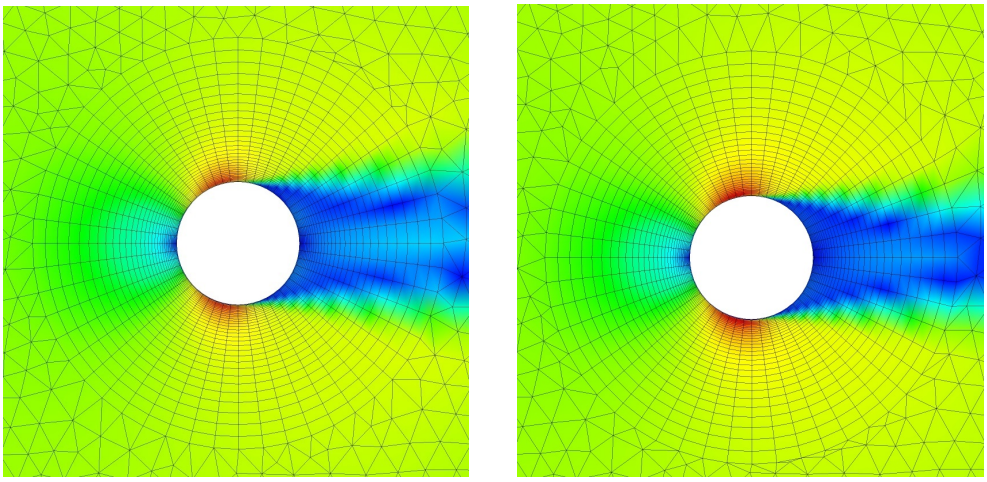

**(a)** Original mesh **(b)** Updated mesh at new time step

**Figure D.7:** Spring based smoothing

Cell smoothing is sufficient if the boundary displacement is comparable to the cell size. The blade displacement per time step is relatively large compared to its adjacent cell sizes. This means that the cell quality might deteriorate or it can lead to the formation of negative cell volumes. Fluent identifies cells that violate the skewness or size criterion and locally remeshes these cells and inerpolates the solution from the old cells (ANSYS Inc., 2013*b*).

Important to note is that the conservation equation in the dynamic mesh regions require an alteration to the convection term. For a general scalar $\phi$ on an arbitrary control volume $V$ with boundary $\partial V$, the integral form of the conservation equation is given as follows (ANSYS Inc., 2013*a*):

$$\frac{d}{dt}\int_V \rho\phi dV + \int_{\partial V} \rho\phi\left(\vec{U} - \vec{U}_g\right)\cdot d\vec{A} = \int_{\partial V} \Gamma\nabla\phi\cdot d\vec{A} + \int_V S_\phi dV \qquad \text{(D.5)}$$

where $\vec{A}$ is the face vector of the boundary faces of the cell, $\Gamma$ is the diffusion coefficient and $S_\phi$ is the source term of $\phi$.

The convection term contains the fluid velocity $\vec{U}$ and the mesh velocity of the moving mesh $\vec{U}_g$. If $\vec{U}_g$ equals $\vec{U}$ then the conservation equation is given in a Lagrangian framework where no convection term is required. If $\vec{U}_g$ is zero, then the equation is given in the Eulerian framework. This is the case in the rest of the domain where the mesh was not updated and is not displaced. $\vec{U}_g$ is not limited to those two cases but can also vary as done in Arbitrary Lagrangian Eulerian (ALE) methods (Codina *et al.*, 2009). In Fluent, $\vec{U}_g$ is prescribed by the FSI interface displacement.

# Appendix E

# Mesh-based FSI model set-up

This appendix covers additional information for section 4.3. The structural and fluid simulations are linked using an FSI interface. The additional FSI settings are as follows:

**Simulation time:** The simulation time has to be set so that the blade's transient response is negligible and the solution converges to the blade's steady oscillating motion. The solution converges rapidly due to the additional aerodynamic damping and thus the end time is set to 3.96 sec. Convergence was ensured by fitting linear trendlines through the maximum and minimum peak tip displacement values as shown in figure E.1. The trendlines are nearly horizontal and an increase in simulation time will not alter the solution.

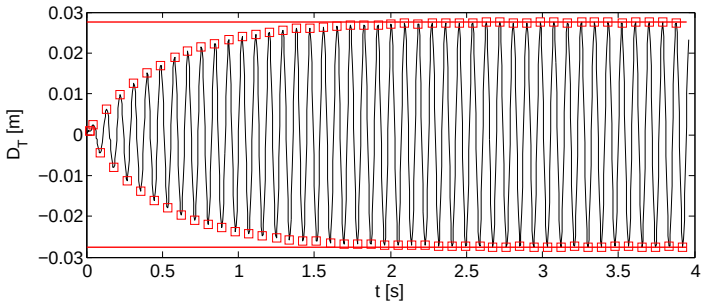


**Figure E.1:** Convergence of blade's tip displacement to steady peak limits (indicated by the fitted red lines)

**Stagger iterations:** As mentioned in section 3.1.2, a strong coupling is required for the aerodynamic damping simulation. For the 0AOA simulation only two stagger iterations were required per time step. The flow simulation requires 5 iterations per stagger iteration and converges rapidly, because of a rather simple flow field around the blade. The 9AOA simulation on the other hand, required 5 stagger iterations and 10 fluid iterations per stagger iteration. A strong coupling is required, because the flow simulation requires time to converge due to the complex flow field around the rotated blade.

## E.1 Sensitivity analysis

The number of stagger and fluid iterations were increased to ensure that the solution is independent of these values. The 0AOA simulation was run once with 3 stagger iterations and 10 fluid iterations. The results were identical to those of the simulation with 2 stagger and 5 fluid iterations. The same procedure was performed with the 9AOA simulation. The stagger iterations were increased to 6 and the fluid iterations were set to 15. Both resulted in the same tip displacement.

The 0AOA and 9AOA simulation were tested with the lowest inlet velocity. This ensured maximum mesh distortion and a complex flow field due to maximum tip displacement.

The simulation sensitivity to certain other parameters was also tested. Parameters that were slightly altered include the inlet velocity, material and air properties, turbulence intensity and viscosity ratio and numerical damping factor. Alterations of the material and air properties as well as inlet velocity by 5 % resulted in no noticeable change in predicted tip displacement. The numerical damping factor has a noticeable effect on the tip displacement, because it removes energy from the system. Thus, it was not altered from the suggested value of 0.1 (ANSYS Inc., 2013*d*). According to Shyy *et al.* (2013) the turbulence intensity (TI) can affect the lift prediction and effects the predicted reattachment point of the laminar separation bubble for example. The tip displacement was observed at an inlet TI of 10 % and at 1.1 % with minor differences.

## E.2 Non-occurring flow phenomena

### E.2.1 Laminar separation bubble (LSB)

This flow phenomena occurs at relatively low boundary Reynold's numbers where the flow is not yet fully turbulent (Jahanmiri, 2011). The range of Reynold numbers predict that the flow over the blade is not yet fully turbulent, as stated in section 2.3, and therefore the development of a LSB is possible.

Turbulent flow is less susceptible to adverse pressure gradients than laminar flow, because turbulent mixing introduces high momentum free stream fluid into the near wall region, which inhibits flow separation.

A LSB occurs if laminar flow separates from the blade's leading edge, which then reattaches further downstream as shown in figure E.2. The flow separation induces flow irregularities, which if sufficient, can cause flow transition. This in turn causes mixing that increases the fluid momentum near the wall. If the turbulent mixing is sufficient to overcome the adverse pressure gradient effects, then the flow reattaches (Shyy *et al.*, 2013).

A small recirculation zone or bubble is created between the separation and reattachment point. Downstream of the separation point, the recirculating flow velocity is significantly lower than the free stream velocity, which causes a pressure increase in this region. This means that a high pressure region is introduced on the suction side of the blade that significantly reduces the lift force acting on the blade. As mentioned in Shyy *et al.* (2013), a short LSB initiates the formation of a turbulent boundary layer and the long LSB directly influences the aerodynamic characteristics of the blade. A constant high pressure region/plateau is observed on the blade's suction side if a LSB is formed.

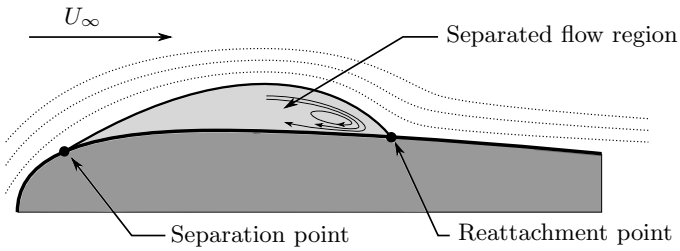


**Figure E.2:** Laminar separation bubble

The Reynolds number, pressure distribution, surface roughness and free stream turbulence affect the dynamics of a LSB. Flow reattachment is delayed or completely prevented if the Reynolds number decreases because the viscous damping effect increases and delays flow transition. A small increase in the adverse pressure gradient due to an increase in AOA causes intensified flow irregularities that accelerate flow transition. Therefore a shorter LSB is formed. Otherwise, if the adverse pressure gradient is significantly increased due to a large change in AOA, turbulent diffusion might not be sufficient for flow reattachment (Shyy *et al.*, 2013).

No pressure increase or pressure plateau was observed on the blade's suction side in the presence of the SFR. The flow within the separated flow region was not observed to be stagnant and therefore lowered the pressure due to the formation of leading edge vortices.

### E.2.2 Wake capture

Wake capture can influence the dynamic loading on the blade if the Strouhal number is sufficiently large. It is defined as a non-dimensional parameter given by the ratio between the translational wing velocity and the free stream velocity for plunging aerofoils (Shyy *et al.*, 2013).

Figure E.3 visualises wake capture for a plunging aerofoil. During the blade's upward motion, a clockwise rotating vortex is shed from the trailing edge. The vortex is convected downstream as the blade is further displaced. A counter-clockwise vortex is then shed from the blade during downward blade

motion. If the Strouhal number is sufficiently large, the blade interacts with its previously shed vortex. This increases the effective flow speed around the blade and induces an additional lifting force (Shyy *et al.*, 2013). This phenomenon is termed wake capture.

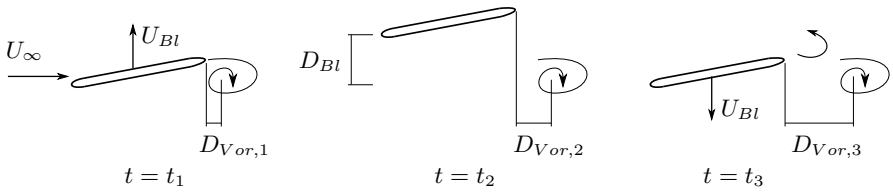


**Figure E.3:** Wake capture process

At instance $t_1$ the centre of the shed vortex is located a distance $D_{Vor,1}$ away from the trailing edge. The distance from the trailing edge to the centre of the vortex at $t_3$ increases to:

$$D_{Vor,3} = D_{Vor,1} + U_\infty \left(t_3 - t_1\right) \tag{E.1}$$

assuming that the vortex is convected downstream with a velocity equal to the free stream velocity $U_\infty$. The simple assumption is made that the vortex has to grow equal to $D_{Vor,3}$ for wake capture to occur. If the blade motion is given by:

$$D_{Bl} = D_0 \sin\left(2\pi f t\right) \tag{E.2}$$

then the blade requires $1/(2\,f)$ seconds from $t_1$ to $t_3$. Substituting this value into equation (E.1) gives:

$$D_{Vor,3} = D_{Vor,1} + \frac{U_\infty}{2f} \tag{E.3}$$

Substituting the lowest experimentally tested free stream velocity and the blade's natural frequency gives:

$$D_{Vor,3} = D_{Vor,1} + 0.4415\,m \approx D_{Vor,1} + 3.68\,c \tag{E.4}$$

This suggests that the wake vortex has to grow 3.68 times the blade's chord length in 0.044 15 sec for it to interact with the blade. Even if the vortex grows by such a substantial amount, the resulting vortex velocity will not be sufficient to increase the lift force acting on the blade. Thus, wake capture plays a negligible role in the investigation of the blade's aerodynamic damping.

# Appendix F

# Simplified 1D model set-up

This appendix covers additional information for chapter 5, such as the validation of the simplified 1D beam model and the theoretical flow models.

## F.1 Simplified blade geometry

The Euler-Bernoulli beam model requires the modulus of elasticity and the moment of inertia of the cross section in the transverse direction. The blade geometry was therefore simplified and is given by simple geometries as shown in figure F.1.

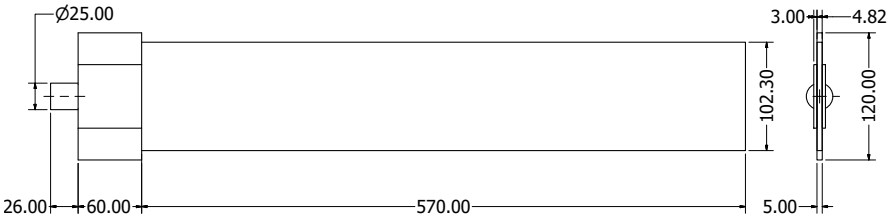


**Figure F.1:** Simplified blade geometry for the Euler-Bernoulli model

Due to the simplifications, the natural frequencies were not accurately predicted and the chord length of the upper aluminium blade was slightly reduced to better approximate the modal frequencies.

## F.2 Structural model validation

The structural model was first validated before it was coupled with the heuristic flow model. The same procedure was followed as for the mesh-based structural model validation.

Firstly, an undamped modal analysis was performed while varying the nodal count. The first, second and third bending frequency are displayed relative to the number of nodes in figure F.2. The solution is independent of the number of nodes if the model contains more than 25 nodes. The model's deviation from the first and second bending mode is $-0.203\,\%$ and $2.33\,\%$ respectively.

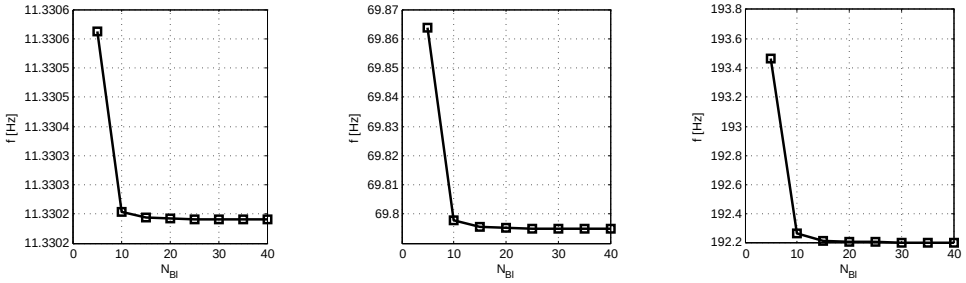


**(a)** 1st bending mode **(b)** 2nd bending mode **(c)** 3rd bending mode

**Figure F.2:** Node independence study using a modal analysis for the simplified model

The transient decay simulation, used for the mesh-based structural model validation, was also employed for the simplified two-dimensional model validation. The damping coefficient is 0.001 306 which is 2.06 % below the experimental value.

## F.3 Heuristic flow model validation

Basson (2015) measured the blade deflection for different air stream velocities and geometric AOAs without base excitation. These results were used to validate the heuristic flow model. Removing the blade's base excitation allows for steady deflection of the blade. Therefore, dynamic flow effects are not present. The added mass, Polhamus and the Theodorsen model were neglected. Figure F.3 compares the model's tip deflection at various inlet velocities with the experimentally determined tip deflections. The maximum relative deviation of the model's steady tip displacement is 11.1 % at an inlet velocity of 10.717 m/s.

## F.4 Derivation of the relative acceleration of the fluid for the added mass effect

In this section the added mass effect is derived for blade oscillation in a non-stationary fluid. A general correction factor is determined for the flapwise added mass of a transversely oscillating flat plate that is rotated relative to the free stream.

As mentioned in section 2.5.1, the relative velocity of the blade is given as:

$$U_{Rel} = \sqrt{\left(U_{In}\cos\left(\alpha_G\right)\right)^2 + \left(-U_{Bl} + U_{In}\sin\left(\alpha_G\right)\right)^2} \tag{F.1}$$

This equation can be simplified using trigonometric identities to give:

$$U_{Rel} = \sqrt{U_{In}^2 - 2U_{In}U_{Bl}\sin\left(\alpha_G\right) + U_{Bl}^2} \tag{F.2}$$

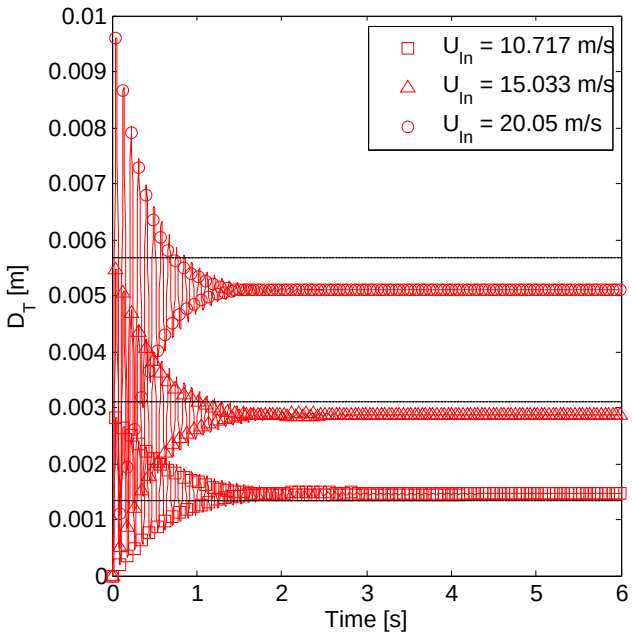


**Figure F.3:** Steady validation of the heuristic flow model at a 9° geometric AOA. The horizontal black lines mark the experimental results

Deriving this equation with respect to time gives the acceleration of the blade relative to the fluid. The geometric AOA and inlet velocities are constant for each simulation and are therefore time independent. This gives the relative acceleration:

$$\frac{\partial U}{\partial t} = \dot{U}_{Bl} G = \frac{\dot{U}_{Bl}\left(U_{Bl} - U_{In}\sin\left(\alpha_G\right)\right)}{\sqrt{U_{In}^2 - 2U_{In}U_{Bl}\sin\left(\alpha_G\right) + U_{Bl}^2}} \tag{F.3}$$

If the geometric AOA is zero then the relative acceleration can be simplified:

$$\frac{\partial U}{\partial t} = \frac{\dot{U}_{Bl}U_{Bl}}{\sqrt{U_{In}^2 + U_{Bl}^2}} \tag{F.4}$$

Assuming sinusoidal displacement of the blade, then:

$$U_{Bl} = U_0\cos\left(r\omega t\right) \tag{F.5}$$

The correction term can then be written as:

$$G(t, k_{AM}) = \frac{k_{AM}\cos(r\omega t)}{\sqrt{1 + k_{AM}^2\cos^2(r\omega t)}} \tag{F.6}$$

where $k_{AM}$ is the ratio of the blade's maximum velocity to the inlet velocity. Konstantinidis (2013) came to the same result using potential flow theory and investigating a transversely oscillating cylinder in a free stream.

## F.5 Particle swarm algorithm

$A_{Pol}$ is used to approximate $V_{Emp}$, a function that is known at discrete points in time and space. The variables upon which $A_{Pol}$ is based, are also known at the same locations. There are more discrete points at which $V_{Emp}$ has to be approximated by $A_{Pol}$ than there are unknown coefficients in $A_{Pol}$ to be determined. This results in an overdetermined system. The error function, given in equation (5.17), has to be minimised to determine the coefficients of $A_{Pol}$ that offer the best approximation of $V_{Emp}$. This was achieved by using the particle swarm optimisation algorithm (PSOA). The following steps are performed in the PSOA to determine the unknown coefficients (Schutte and Groenwold, 2003):

**Step 1:** The first step is to initialise a set of particles. Each particle has a position vector $\boldsymbol{x}_P$ that contains the unknown coefficients of $A_{Pol}$. These are chosen randomly within a given range to offer the first approximation of $V_{Emp}$.

**Step 2:** The guessed position vector of each particle is then used to evaluate equation (5.17). As mentioned, the error function has to be minimised to find the best approximation of $V_{Emp}$. Therefore, the global minimum error $E_{Glo}$ and the corresponding position vector $\boldsymbol{x}_{Glo}$ are stored as well as each particle's local minimum error $E_{Loc}$ and its position $\boldsymbol{x}_{Loc}$.

**Step 3:** Each particle is moved to its new position $\boldsymbol{x}_{P,n+1}$ by solving:

$$\boldsymbol{x}_{P,n+1} = \boldsymbol{x}_{P,n} + \dot{\boldsymbol{x}}_{P,n+1} \tag{F.7}$$

where $\boldsymbol{x}_{P,n}$ is the particle's old position and $\dot{\boldsymbol{x}}_{P,n+1}$ is determined from

$$\dot{\boldsymbol{x}}_{P,n+1} = \beta\dot{\boldsymbol{x}}_{P,n} + (1-\beta)\left(2r_{Glo}\left(\boldsymbol{x}_{Glo} - \boldsymbol{x}_{P,n}\right) + 2r_{Loc}\left(\boldsymbol{x}_{Loc} - \boldsymbol{x}_{P,n}\right)\right) \tag{F.8}$$

In the first iteration step, the particle's previous velocity vector $\dot{\boldsymbol{x}}_{P,n}$ is not known and is therefore set to zero. According to Schutte and Groenwold (2003), the inertia term $\beta$ should be selected so that $0.8 < \beta < 1.4$. In equation (F.8), $r_{Glo}$ and $r_{Loc}$ represent random numbers ranging from 0 to 1.

**Step 4:** The error is determined at each particle's new position by substituting it into equation (5.17). If a lower global or local minimum is found then these are stored.

**Step 5:** Step 3 and 4 are repeated until $E_{Glo}$ converges or the maximum number of iterations are reached. The final determined coefficients of $A_{Pol}$ are given in table F.1.

**Table F.1:** Coefficients for each term of $A_{Pol}$

| | $\alpha_E^2$ | $\alpha_E^2 z$ | $\lvert\alpha_E\rvert$ | $\lvert\alpha_E\rvert z$ | $z$ | 1 |
|---|---|---|---|---|---|---|
| V10 | 0.118 | -0.207 | -0.378 | 0.897 | 7.69 | -3.51 |
| V15 | 0.171 | -0.295 | -0.558 | 1.066 | 13.32 | -6.38 |
| V20 | 0.137 | -0.212 | -0.127 | 0.029 | 16.16 | -7.60 |

# Appendix G

# Additional information for the meshless FSI simulation

The main focus of this appendix is to offer additional information regarding the point cloud refinement and the point cloud independence study performed.

As mentioned in section 6.2, the smoothing length can be adjusted in time and space. Figure 6.2 shows the spatial variation of the smoothing length in the fluid domain. A fine point cloud surrounds the blade to capture the occurring flow phenomena. Further away from the blade, the point cloud is coarsened to reduce the computational cost of the simulation without affecting the accuracy of the blade's aerodynamic loading prediction.

Similarly, the point cloud is refined in time. At the beginning of the simulation, the blade has not yet reached its steady response as shown in figure E.1. Therefore, the aerodynamic load does not have to be modelled accurately as the interest of the investigation lies with the blade's steady response. For that reason, a coarser initial point cloud, with approximately half of its final number of points, is chosen to accelerate the simulation. The point cloud in the entire simulation domain is then linearly refined as the simulation progresses. At 2.5 sec, the final smoothing length is reached and kept constant with respect to time because the blade's oscillating motion starts to converge.

The initial discretization error, due to the coarse point cloud, is relatively large compared to the discretization error when the final smoothing length is reached. The discretization error after 2.5 seconds is assumed negligible because the simulation is point cloud independent when the final smoothing length is reached.

A steady CFD simulation was used to validate the FPM simulation by comparing its predicted lift coefficient to that determined by Riegels (1961) for a flat plate. Figure G.1 shows the predicted lift coefficient using four different point clouds. The FPM simulation is point cloud independent because the figure shows that all four different simulations predict a similar lift coefficient. The predicted lift coefficient is less than that determined experimentally by Riegels (1961) due to downwash. The lift coefficient from Riegels (1961) is for a two-dimensional flat plate and therefore the determined lift coefficient is unaffected by downwash as it does not occur.

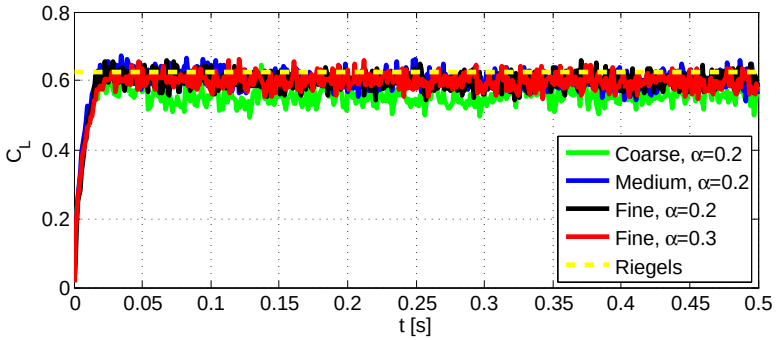


**Figure G.1:** The lift coefficient from Riegels (1961) for a flat plate is compared to that determined by FPM at a 9 degree geometric angle of attack

The constant $\alpha$ used in equation (6.4) was also altered to ensure that the simulation is independent of the time step size. As shown in the figure, increasing $\alpha$ to 0.3 results in no loss in accuracy. The fine point cloud with $\alpha = 0.3$ is used in the FSI simulation because a fine point cloud is required to resolve the separated flow region on the blade's surface.

The number of points and final smoothing length specifications are given for each point cloud in table G.1. A fine point cloud is contained within a cylinder of radius $R$ in which the blade is located. The smoothing length within the cylinder is specified by $h_{SL,Min}$. As shown in figure 6.2, the smoothing length outside of the cylinder increases radially until its maximum smoothing length is reached. The spatial smoothing length growth rate $h_{SL,Gr}$ and its maximum smoothing length $h_{SL,Max}$ are also stated in table G.1.

**Table G.1:** Final number of points and smoothing length for each of the three point clouds

| | Point count | $h_{SL,Min}$ | $R$ | $h_{SL,Gr}$ | $h_{SL,Max}$ |
|---|---|---|---|---|---|
| Coarse | 165136 | 0.03 | 0.06 m | $0.1\,\mathrm{m}^{-1}$ | 0.1 |
| Medium | 266167 | 0.025 | 0.07 m | $0.09\,\mathrm{m}^{-1}$ | 0.09 |
| Fine | 468842 | 0.02 | 0.08 m | $0.08\,\mathrm{m}^{-1}$ | 0.08 |

# List of References


Alavala, C. (2008). *Finite Element Methods: Basic Concepts and Applications*. PHI Learning. (Cited on page 86.)

Anderson, J. (1991). *Fundamentals of Aerodynamics*. Mc-Graw-Hill Series in Aeronautical and Aerospace Engineering. (Cited on pages 57, 58, and 60.)

ANSYS Inc. (2009 April). *ANSYS Theory Reference for the Mechanical APDL and Mechanical Applications*, 12th edn.
Available at: http://www.ansys.com (Cited on pages 31 and 32.)

ANSYS Inc. (2013 Novemebera). *ANSYS Fluent Theory Guide*, release 15.0 edn.
Available at: http://www.ansys.com (Cited on pages 98 and 101.)

ANSYS Inc. (2013 Novemberb). *ANSYS Fluent User's Guide*, 15th edn.
Available at: http://www.ansys.com (Cited on pages 36, 37, 95, 98, 99, and 100.)

ANSYS Inc. (2013 Novemeberc). *ANSYS Mechanical APDL Structural Analysis Guide*, 15th edn.
Available at: http://www.ansys.com (Cited on pages 30, 31, 32, and 33.)

ANSYS Inc. (2013 Novemberd). *ANSYS Mechanical User's Guide*, release 15.0 edn. (Cited on pages 85, 89, and 103.)

ANSYS Inc. (2013 Novembere). *ANSYS Meshing User's Guide*, release 15.0 edn.
Available at: http://www.ansys.com (Cited on page 90.)

Avinash (2016 May). Rankine cycle. Online.
Available at: https://tractionmech8.wordpress.com/2014/04/18/rankine-cycle/ (Cited on pages ix and 1.)

Basson, N. (2015). *Investigating The Effect of Aerodynamic Damping on an Axial Flow Fan Blade*. Master's thesis, University of Stellenbosch. (Cited on pages iii, iv, ix, 5, 6, 7, 8, 9, 10, 11, 13, 14, 15, 17, 26, 35, 39, 41, 85, 87, 99, and 107.)

Bathe, K. and Noh, G. (2012). Insight into an implicit time integration scheme for structural dynamics. *Elsevier: Computers and Structures*. (Cited on pages ix, 32, and 33.)

Bijl, H., van Zuijlen, H. and Bosscher, S. (2006). Two level algorithms for partitioned fluid-structure interaction computations. *European Conference on Computational Fluid Dynamics*. (Cited on pages 15, 20, 21, and 22.)

Bos, A. (1994). *A method to account for partial leading-edge suction and vortex flow for swept and deltawings at subsonic and supersonic speeds*. Ph.D. thesis, Delft University of Technology. (Cited on page 60.)

Brandsen, J. (2013). *Prediction of Axial Compressor Blade Vibration by Modelling Fluid-Structure Interaction*. Master's thesis, Stellenbosch University. (Cited on pages 12, 15, 30, 32, 34, and 90.)

Brennen, C. (1982). A review of added mass and fluid inertial forces. Tech. Rep., Naval Civil Engineering Laboratory Port Hueneme, Claifornia. (Cited on page 59.)

Brunton, S. (2012). *Unsteady Aerodynamic Models for Agile Flight at Low Reynolds Numbers*. Ph.D. thesis, Princeton University. (Cited on page 58.)

Bungartz, H. and Mehl, M. (2010). *Fluid Structure interaction II*. Springer. (Cited on page 32.)

Cengel, Y. and Boles, M. (2008). *Thermodynamics: An engineering approach*. Mc Graw Hill. (Cited on page 2.)

Cengel, Y. and Cimbala, J. (2010). *Fluid Mechanics: Fundamentals and Applications*. Mc Graw Hill. (Cited on pages 11, 16, 37, 44, 84, and 97.)

Cengel, Y. and Ghajar, A. (2011). *Heat and mass transfer: Fundamentals and applications*. Mc Graw Hill. (Cited on pages 2 and 85.)

Chang, P. (2014). *Separation of Flow*. Elsevier Science.
Available at: https://books.google.co.za/books?id=nthQAwAAQBAJ (Cited on page 43.)

Chattot, J. and Hafez, M. (2015). *Theoretical and Applied Aerodynamics and Related Numerical Methods*. Springer. (Cited on page 57.)

Chowdhury, I. and Dasgupta, S. (2003). Computation of rayleigh damping coefficients for large systems. *The Electronic Journal of Geotechnical Engineering, Volume 8*. (Cited on page 86.)

Codina, R., Houzeaux, G., Coppola-Owen, H. and Baiges, J. (2009). The fixed-mesh ale approach for the numerical approximation of flow in moving domains. *Journal of Computational Physics*. (Cited on page 101.)

Cook, R., Malkus, D., Plesha, M. and Witt, R. (2002). *Concepts and Applications of Finite Element Analysis*. Wiley. (Cited on pages 9, 26, 27, 29, 30, 31, 85, 86, and 88.)

Craig, R. and Kurdila, A. (2006). *Fundamentals of Structural Dynamics*. John Wiley & Sons. (Cited on page 33.)

Cumpsty, N. (1999). *Compressor Aerodynamics*. Longman Group UK Limited. (Cited on page 5.)

de Croon, G., Percin, M., Remes, B., Ruijsink, R. and De Wagter, C. (2015). *The DelFly: Design, Aerodynamics, and Artificial Intelligence of a Flapping Wing Robot*. Springer. (Cited on page 43.)

ENEXIO (2016 June). Energy engineering excellence. Online.
Available at: http://www.enexio.com/products/wet-cooling-towers/ (Cited on page 3.)

Eskom (2013 November). Medupi power station: Fact sheet. Online. Available at: http://www.eskom.co.za/Whatweredoing/NewBuild/MedupiPowerStation/Documents/medupifactsheetsept2013.pdf (Cited on page 2.)

Fries, T. and Matthies, H. (2004). Classification and overview of meshfree methods. *Scientific Computing: Informatikbericht N.: 2003-3*. (Cited on page 32.)

Gatzhammer, B. (2008). *A Partitioned Approach for Fluid-Structure Interaction on Cartesian Grids*. Master's thesis, Technische Universitaet Muenchen. (Cited on pages 20, 21, 22, 23, 24, 25, and 84.)

Green, S. (1995). *Fluid Mechanics and Its Applications: Fluid Vortices*. Springer. (Cited on page 44.)

Gulcat, U. (2016). *Fundamentals of Modern Unsteady Aerodynamics*. Springer. (Cited on pages 58 and 60.)

Harrevelt, S. (2012). *Eigenvalue analysis of the Timoshenko Beam theory with a damped boundary condition*. Master's thesis. (Cited on page 88.)

Harris, C. and Piersol, A. (2002). *Harris' Shock and Vibration Handbook*. McGraw-Hill. (Cited on pages 15 and 59.)

Heyns, J. (2008). *Performance characteristics of an air-cooled steam condenser incorporating a hybrid (dry/wet) dephlegmator*. Master's thesis, University of Stellenbosch. (Cited on page 2.)

Hodges, D. and Pierce, G. (2011). *Introduction to Structural Dynamics and Aeroelasticity, Second Edition*. Cambridge University Press. (Cited on page 4.)

Hou, G., Wang, J. and Layton, A. (2012). Numerical method for fluid-structure interaction- a review. *Global Science Press*. (Cited on pages 19, 20, and 31.)

Howard, C. and Cazzolato, B. (2015). *Acoustic Analyses Using MATLAB and ANSYS*. CRC Press. (Cited on pages 32 and 33.)

Hron, J. and Turek, S. (2006). A monolithic fem solver for an ale formulation of fluid-structure interaction with configuration for numerical benchmarking. *European Conference on Computational Fluid Dynamics*. (Cited on page 19.)

Hsu, M. and Bazilevs, Y. (2012). Fluid-structure interaction modeling of wind turbine: Simulating the full machine. *Springer: Computational Mechanics Volume 50*. (Cited on pages 42 and 82.)

Inman, D. (2014). *Engineering Vibration*. Pearson. (Cited on pages 27 and 28.)

Jahanmiri, M. (2011). Laminar separation bubble: Its structure, dynamics and control. Tech. Rep., Chalmers University of Technology: Department of Applied Mechanics. (Cited on page 103.)

Jefferies, A., Kuhnert, J., Aschenbrenner, L. and Giffhorn, U. (2014). Finite pointset method for the simulation of a vehicle travelling through a body of water. *Springer: Meshfree Methods for Partial Differential Equations VII*. (Cited on page 71.)

Kapooria, R., Kumar, S. and Kasana, K. (2008). An analysis of a thermal power plant working on a rankine cycle: A theoretical investigation. *Journal of Energy in Southern Africa*. (Cited on page 1.)

Katz, J. (1999 March). Wing/vortex interactions and wing rock. *Elsevier: Progress in Aerospace Sciences*, vol. 35, pp. 727–750. (Cited on page 64.)

Kim, J., Jung, W. and Kwon, M. (2013). Dissipation of higher mode using numerical integration algorithm in dynamic analysis. *International Journal of Civil, Environmental, Structural, Construction and Architectural Engineering*, vol. 7, no. 2, pp. 127–134. (Cited on page 31.)

Konstantinidis, E. (2013). Added mass of a circular cylinder oscillating transverse to a free stream. *Proceedings of the Royal Society Volume: 469 Issue: 2156*. (Cited on pages 59 and 109.)

Kröger, D. (2004). *Air-cooled Heat Exchangers and Cooling Towers: Thermal-flow Performance Evaluation and Design*. PennWell Corporation. (Cited on pages 2 and 3.)

Kuhnert, J. (1999). *General Smoothed Particle Hydrodynamics*. Ph.D. thesis, TU Kaiserslautern. (Cited on pages 69 and 72.)

Kuhnert, J. (2001). An upwind finite pointset method (fpm) for compressible euler and navier-stokes equations. *Springer: Meshfree Methods for Partial Differential Equations*, vol. 26, pp. 239–249. (Cited on page 79.)

Kuhnert, J. and Tiwari, S. (2001). Finite pointset method based on the projection method for simulations of the incompressible navier-stokes equations. *Berichte des Fraunhofer ITWM, Nr. 30*. (Cited on page 72.)

Leita Steel Construction (2016 May). Medupi power station. Online. Available at: https://www.aleita.co.za/projects/mining-heavy-industrial-structures/medupi-power-station/ (Cited on page 3.)

Liu, G. and Gu, Y. (2005). *An Introduction to Meshfree Methods and Their Programming*. Springer. (Cited on page 87.)

Liu, G. and Liu, M. (2003). *Smoothed Particle Hydrodynamics: A meshfree particle method*. World Scientific. (Cited on pages 19, 23, 41, 69, and 70.)

Liu, P., Duan, H. and Zhao, W. (2009). Numerical investigation of hot air recirculation of air-cooled condensers at a large power plant. *Elsevier: Applied thermal engineering*. (Cited on pages 3 and 4.)

Mashud, M., Sarwar, M., Mollah, A. and Hossain, F. (2009 December). Experimental study of separated flow control over a sharp-edged arc airfoil. *International Journal of Engineering and Technology IJET-IJENS*, vol. 09, no. 10, pp. 83–88. (Cited on page 44.)

Mostafa, M. (2009). *The Geometric Nonlinear Analysis of Iso-P Quadrilateral Element in 2D*. Ph.D. thesis, CVEN Dept. (Cited on page 9.)

Muiyser, J. (2016). *Investigation of Large-Scale Cooling System Fan Vibration*. Ph.D. thesis, Stellenbosch University. (Cited on page 82.)

Muiyser, J., Els, D., v.d.Spuy, S. and Zapke, A. (2014). Measurement of air flow and blade loading at a large-scale cooling system fan. *Journal of the South African Institution of Mechanical Engineering*. (Cited on pages 3, 4, 5, 6, and 82.)

Nave, R. (2015 August). Sound speed in gases. Online. Available at: http://hyperphysics.phy-astr.gsu.edu/hbase/sound/souspe3.html (Cited on page 85.)

Nisbett, J. (2011). *Shigley's Mechanical Engineering Design*. Mc. (Cited on page 12.)

Pierce, W. (2008). *Evaluation and Performance Prediction of a Wind Turbine Blade*. Master's thesis, Stellenbosch University. (Cited on pages 37, 38, and 39.)

Raja, R. (2012). *Coupled fluid structure interaction analysis on a cylinder exposed to ocean wave loading*. Master's thesis, Chalmers University of Technology. (Cited on page 20.)

Riegels, F. (1961). *Aerofoil Sections: Results from Wind-Tunnel Investigations: Theoretical Foundations*. Butterworths. (Cited on pages ix, xi, 9, 11, 12, 35, 38, 56, 83, 111, and 112.)

Schmucker, H., Flemming, F. and Coulson, S. (2010). Two-way coupled fluid structure interaction simulation of a propeller turbine. *IOP Conf. Series: Earth and Environmental Science 12*. (Cited on page 9.)

Schutte, J. and Groenwold, A. (2003). Sizing design of truss structures using particle swarms. *Structural and Multidisciplinary Optimization*, vol. 25, no. 4, pp. 261–269. Available at: http://dx.doi.org/10.1007/s00158-003-0316-5 (Cited on page 109.)

Seifarth, T. (2014). *Gitterfreie Lsungsschemen zur numerischen Lsung von Transportvorgngen*. Master's thesis, Universitt Kassel. (Cited on pages 70, 71, and 79.)

Shengyi, S., Ingham, D., Ma, L., Pourkashanian, M. and Tao, Z. (2010). Numerical investigations on dynamic stall of low reynolds number flow around oscillating airfoils. *Elsevier: Computers and Fluids*. (Cited on pages 36, 37, 44, and 99.)

Shyy, W., Aono, H., Kang, C. and Liu, H. (2013). *An Introduction to Flapping Wing Aerodynamics*. Cambridge University Press. (Cited on pages 36, 38, 43, 44, 51, 55, 59, 103, 104, and 105.)

Tiwari, S., Antonov, S., Hietel, D., Kuhnert, J., Olawsky, F. and Wegener, R. (2006*a*). A meshfree method for simulations of interactions between fluids and flexible structures. *Berichte des Fraunhofer ITWM, Nr. 88*. (Cited on page 32.)

Tiwari, S., Antonov, S., Hietel, D., Kuhnert, J., Olawsky, F. and Wegener, R. (2006*b*). A meshfree method for simulations of interactions between fluids and flexible structures. *Berichte des Fraunhofer ITWM, Nr. 88*. (Cited on page 71.)

Tooley, M. (2012 February). Fluid-structure interaction using system coupling. Online.
Available at: http://www.ansys-blog.com/fluid-structure-interaction-using-system-coupling/ (Cited on page 22.)

Tramecon, A., de Luca, P., Binetruy, C. and Kuhnert, J. (2006). Finite pointset method (fpm): A meshfree approach for incompressible flow simulations applied to composite materials. *The 8th International Conference on Flow Processes in Composite Materials*. (Cited on pages 71 and 72.)

Versteeg, H. and Malalasekera, W. (2007). *An Introduction to Computational Fluid Dynamics: The Finite Volume Method*. Pearson: Prentice Hall. (Cited on pages 12, 24, 25, and 70.)

Weber, W. and Seidel, U. (2015). Analysis of nattural frequencies of disc-like structures in water environment by coupled fluid-structure-interaction simulation. *6th IAHR International Meeting of the Workgroup on Cavitation and Dynamic Problems in Hydraulic Machinery and Systems*. (Cited on page 41.)

Wick, T. (2011). Fluid-structure interaction using different mesh motion techniques. *Elsevier: Computers and Structures*. (Cited on pages 19 and 23.)

Widmann, A. (2015). *Formation and Detachment of Leading Edge Vortices on Unsteady Airfoils*. Ph.D. thesis, Technical University Darmstadt. (Cited on pages 44 and 45.)

Wright, J. and Cooper, J. (2015). *Introduction to Aircraft Aeroelasticity and Loads*. Wiley. (Cited on pages ix, 42, 43, and 56.)